OBSERVATION AND CHARACTERIZATION OF EXTRA-SOLAR PLANETS USING INDIAN FACILITIES

A Thesis

Submitted for the Degree of

Doctor of Philosophy (Technology)

Submitted by

Aritra Chakrabarty

Department of Applied Optics & Photonics

University College of Technology

University of Calcutta

September 2020

To my Family,

Friends, Teachers and

Supervisor...

Acknowledgements

First and foremost, I would like to express my sincerest gratitude to Prof. Sujan Sengupta, under whose supervision I have carried out my research at the Indian Institute of Astrophysics (IIA), Bangalore. I will forever be indebted to him for his constant support and motivation. His timely actions and feedbacks have helped me in the successful completion of my thesis work on time. I would also like to take this opportunity to thank my associate supervisor, Dr. K. Sankarasubramanian for his insightful inputs in the field of photometric observation which was an integral part of my work. My gratitude goes out to the supporting staff at the Indian Astronomical Observatory (IAO), Hanle; the Centre for Research and Education in Science and Technology (CREST), Hosakote and the Vainu Bappu Observatory (VBO), Kavalur, without whom my research would have been impossible to carry out. Indispensable tools like PyRAF which I have extensively used for most of the tasks of reduction and photometry, has definitely made my work a lot easier. PyRAF is a product of the Space Telescope Science Institute, which is operated by AURA for NASA. I acknowledge Dr. Parijat Thakur and Vineet Mannaday for providing me with the raw data acquired on two nights in 2018. I heartily thank Dr. Michael Gillon for his prompt response and help at the initial stage of my project. I am grateful to Prof. Giovanna Tinetti, Prof. Jonathon Tennyson, Dr. Marcell Tessenyi, Angelos, Gordon, Billy and Ingo for warmly welcoming me at the University College London, UK. My heartfelt thanks to Prof. Tinetti for all the valuable discussions we had at our meetings and for providing us the various data relevant to the modeling of transmission spectra of exoplanets. I am also grateful to Dr. Sukrit Ranjan for sharing his insights and also for giving me the opportunity to present my work at the Massachusetts Institute of Technology, USA. I would like to extend my thanks to Prof. Gopinathan Maheswar, Dr. Girish V., Prof. Rajib Chakraborty and Prof. Kallol Bhattacharya along with my supervisor for assessing my pre-PhD seminar with their critical and valuable insights. I would like to thank Prof. Kallol Bhattacharya, Prof. Rajib Chakraborty, Prof. A. K. Dutta, Prof. Ajay Ghosh, Prof. Mina Ray, Prof. L.N. Hazra, Prof. Amitabha Basuray, Prof. A. K. Chakraborty and Prof. S.

K. Sarkar for their valuable lessons imparted during the coursework at the Calcutta University. I am thankful to Prof. C. S. Stalin, Prof. Gajendra Pandey, Prof. Sivarani Thirupathi, Dr. Brajesh Kumar and Dr. Suvendu Rakshit for their valuable suggestions to my observation-related work. Also, I sincerely thank the former director of IIA, Prof. P. Sreekumar and the present dean of IIA, Prof. G. C. Anupama along with my supervisor for their assistance during the visit to the University College London, UK and present my work there along with them. They have also given me advice useful to my research at various points of time. Above all, IIA has been a home away from home. I will forever be grateful that I could be a part of this institute, experience the amazing culture carried forward by the faculty, seniors and juniors, utilize the innumerable resources, namely the observing facilities, to hone my skills and aid my research and most importantly receive any sort of help whenever I found myself stuck. I would like to thank my juniors from the same research group, namely Soumya, Suman and Manika for their support and all the discussions we had at the group meet- ings. I would like to thank my seniors, namely Subhamoy, Panini, Phanindra, Hemanth, Prasanna Deshmukh, Ramya, Mugundhan, Sreekanth and Shubham for their help and valuable suggestions. I thank Anirban, Sireesha and Avrajit for their immense help with spectroscopy. I would particularly like to thank my present batchmates, namely Pavan and Tanya as well as my ex-batchmate and friend Souvik, as they have been giving me company as well as helpful insights since the day I joined IIA. I would like to thank my juniors, namely Subhankar, Pallavi, Athira and especially, my roommate Swastik for their company and support. I would like to thank all the other friends of mine from IIA, namely Avinash, Samrat, Snehalata, Tridib, Amit, Megha, Raghubar and Pavana for the memory I will carry of their wonderful company and the intense informative discussions we had on various topics. Besides, I thank all the other friends and teachers from my alma maters. I thank my friend Debdutta for informing me of the possible ways of pursuing a Ph.D. in Astronomy and Astrophysics after the completion of my Bachelor's degree in Engineering. Most importantly, I am forever indebted to my parents, my grandparents, my sister and her extended family, my maternal uncle and aunt for their indomitable support throughout my life

for all the decisions I have made and especially, to my parents for encouraging me to follow the path that lead me to my dreams. I cannot conclude without expressing my eternal gratitude to Shreshtha and her family for constantly supporting and inspiring me to pursue my ambition. Last but not the least, I am grateful to the Department of Science and Technology of India for providing financial support, allowing me to pursue my research seamlessly.

List of Publications and Presentations

1. Peer Reviewed Journals (Published/Accepted)

(a) **Aritra Chakrabarty** and Sujan Sengupta, *Precise Photometric Transit Follow-up Observations of Five Close-in Exoplanets : Update on Their Physical Properties*, The Astronomical Journal, Vol. 158:39, 2019. [1]

(b) Sujan Sengupta, **Aritra Chakrabarty** and Giovanna Tinetti, *Optical Transmission Spectra of Hot Jupiters: Effects of Scattering*, The Astrophysical Journal, Vol. 889:181, 2020. [2]

(c) **Aritra Chakrabarty** and Sujan Sengupta, *Effects of Thermal Emission on the Transmission Spectra of Hot Jupiters*, The Astrophysical Journal, Vol. 898:89, 2020. [3]

2. Selected Conference Abstracts (talk/poster)

(a) **Aritra Chakrabarty** and Sujan Sengupta, *Limb Darkening of T-Brown Dwarfs*, XXXVI Annual Meeting of Astronomical Society of India, Osmania University, Hyderabad, India, February 5-9, 2018.

(b) **Aritra Chakrabarty** and Sujan Sengupta, *Detection and Characterization of Exoplanets using BINA*, Accepted in 2nd BINA Workshop, Royal Observatory of Belgium, Brussels, Belgium, October 9-12, 2018.

(c) **Aritra Chakrabarty** and Sujan Sengupta, *Precise Transit Photometric Observation of the Extra-solar Planets Using Indian Astronomical Facilities*, XXXVII Annual Meeting of Astronomical Society of India, Bengaluru, Christ University, India, February 18-22, 2019.

[1] Presented in Chapter 2 and Chapter 3
[2] Presented in Chapter 4 and Chapter 5
[3] Presented in Chapter 6

(d) **Aritra Chakrabarty** and Sujan Sengupta, *Precise Transit Photometric Observation of Close-in Exoplanets Using Indian Astronomical Facilities*, SEEC Symposium 2019, NASA GSFC, Greenbelt, USA, November 4-8, 2019.

(e) **Aritra Chakrabarty** and Sujan Sengupta, *Transmission Spectra: Towards the Understanding of the Atmospheres of the Exoplanets*, Accepted in XXXVIII Annual Meeting of Astronomical Society of India, IISER Tirupati, Tirupati, India, February 13-17, 2020.

3. Invited Talks

(a) **Aritra Chakrabarty** and Sujan Sengupta, *Detection and Characterization of Exo-planets Using Indian Astronomical Facilities*, University College London, London, UK, April 2, 2018.

(b) **Aritra Chakrabarty** and Sujan Sengupta, *Extra-Solar Planets: Observation From VBO*, Commemoration of 50 Years of Vainu Bappu Observatory, IIA, Bengaluru, India, August 9, 2018.

(c) **Aritra Chakrabarty** and Sujan Sengupta, *Precise Transit Observation and Characterization of Exoplanets*, Massachusetts Institute of Technology, Cambridge, USA, October 31, 2019.

Abstract

Detection and characterization of extra-solar planets (also known as exoplanets) is an emerging field that has been constantly evolving with the advent of new cutting-edge observational techniques and the development of state-of-the-art models to interpret the observational results. Since the discovery of the first confirmed planet orbiting around a Solar type star, 51 Pegasi, in 1995, the astronomers have engaged in a global and systematic quest for understanding the origin and evolution of the exoplanets. Till date over 4200 exoplanetary detections have been confirmed and a few of those planets have been studied extensively using different photometric and spectroscopic techniques. Transit photometry and transit spectroscopy are the two essential tools, in this regard, for the detection and characterization of the exoplanets. We have used the 2m Himalayan Chandra Telescope (HCT) and the 1.3m Jagadish Chandra Bhattacharyya Telescope (JCBT) for the photometric follow-up observations of the transit events of some confirmed Jupiter-sized close-in planets (hot Jupiters) such as WASP-33b, WASP-50b, WASP-12b, HATS-18b, HAT-P-36b, etc. This exercise is a part of the capability testing of the two telescopes and their back-end instruments in the field of transit photometry. Leveraging the large aperture of both the telescopes used, the images acquired during several nights were used to produce the transit light curves with high photometric signal-to-noise ratio (SNR $>$ 200) by performing differential photometry. In order to reduce the fluctuations in the transit light curves due to various sources such as stellar activity, varying sky transparency etc. we preprocessed them using wavelet denoising and applied the Gaussian process correlated noise modeling technique while modeling the transit light curves. A state-of-the-art algorithm used for modeling the transit light curves provided the physical parameters of the planets with more precise values than reported earlier.

Also, we present the results obtained from the high-resolution transit spectroscopic observations of some bright stars ($V_{mag} < 12$) from the 2.34 m Vainu Bappu Telescope (VBT) which are aimed at the characterization of the atmospheres of the exoplanets. The results show that the spectral SNR achieved with these observations are not enough to draw any inference on the atmo-

spheric contents of the exoplanets and instead, we need repeated observations to improve the SNR, preferably a telescope with an even larger aperture ($> 4m$).

Besides, another important aspect of the project is the theoretical modeling of the atmospheres of the hot Jupiters to predict the nature of their transmission, reflection and emission spectra for different values of the physical parameters such as size, surface gravity, irradiation temperature, internal temperature, etc. We have used external databases for the abundance and opacity of the atoms and molecules in the planetary atmospheres, considering solar metallicity and solar Carbon-to-Oxygen (C/O) ratio. We have developed a complete pipeline that calculates all the physical and chemical properties of the atmospheres of the hot Jupiters and computes the effect of the interaction between the light and the atmospheric contents by either using the Beer-Bouguer-Lambert law or solving the 1-D multiple scattering radiative transfer equations using discrete space theory. We have extensively studied the effect of scattering albedo and the planetary emission on the transmission spectra of the hot Jupiters. These studies are aimed at a more accurate and consistent representation of all the physical and chemical processes occurring in the atmospheres of the exoplanets to precisely model the bulk amount of observational data to be obtained from the upcoming missions such as James Webb Space Telescope (JWST), Atmospheric Remote-sensing Exoplanet Large-survey (ARIEL) and so forth.

Contents

List of Figures

List of Tables

Chapter 1

Introduction

1.1 Introduction

A systematic scientific and global quest in understanding the planets and the planetary systems outside the solar system was boosted in 1995 with the discovery of the first confirmed planet orbiting around a solar-type star, 51 Pegasi. Since then, astronomers have discovered a large variety of planets with sizes ranging from sub-Earth to giant jovian planets. These discoveries along with the characterization of quite a few planets have revolutionized our concept of planetary science. Although more than 4200 extra-solar (also known as exoplanets) planets have been confirmed by the ground- and the space-based telescopes, this is just a small fraction of exoplanets in the solar neighborhood and a large number of planets with different physical properties are yet to be discovered. At the same time, understanding the properties and dynamics of various planets already discovered is another important aspect of exoplanet research. These pieces of information help us reshape and develop our understanding of planet formation, evolution, physical and chemical structure, and interaction with their host stars. These can in turn give us a better understanding of the formation and evolution of the solar system. On the other hand, these studies

can be extended to a thorough understanding of habitability in the quest for extra-terrestrial life.

An exoplanet is named according to the convention for naming multiple-star systems as adopted by the International Astronomical Union (IAU). The name of an exoplanet orbiting a single star is formed by adding a lower case letter after the name of the parent star. The letter 'a' denotes the parent star itself and hence, the planets are designated with the letters from 'b' onward according to the chronological order of discovery (i.e., the first planet discovered around a star is designated with the letter, 'b'). e.g., HD 209458 b. If multiple planets are discovered around a host star at the same time, then the letters are assigned to those planets in the increasing order of distance from the parent star (i.e., the planet nearest to the parent star is identified with the letter, 'b').

With the current technology, most of the planets orbiting at a distance of a few Astronomical Units from their parent stars cannot be spatially resolved from their hosts and hence, indirect methods are used to detect and study them. However, the distant young self-luminous planets can be directly imaged in the mid and far-infrared wavelength region using masking techniques such as coronagraphs. In the following section, we discuss the techniques used for detection and detailed study of exoplanets in different regimes of wavelengths and physical properties.

1.2 Detection Techniques of Exoplanets in a Nutshell

There are various direct and indirect techniques for the detection of exoplanets that involve extreme precision in observation, critical analysis of observed data and extensive models of planetary motion and structure. To date, all the methods other than the direct imaging method rely on some kind of perturbation on the light coming from the host stars created by the orbiting planets. Some of

the most important and widely used detection techniques are described briefly below.

1.2.1 Transit Method

Most of the planets so far (over 3000, see Figure 1.2) have been discovered using the transit method. When an exoplanet transits across its host star it blocks some light, analyzing which, we get information about the planets such as the size, the orbital inclination, the semi-major axis of the orbit, etc. In order for transit to happen, the orbital planes of the planets need to be edge-on i.e. aligned to our line-of-sight (LOS). Transit events can be observed in both visible and near-infrared (NIR) region. This method alone, however, does not give any information about the mass of the planet. With current technology, this method requires the planets to be extremely close to their host stars (see Figure 1.1), leading to short orbital periods (hence, multiple transits can be observed) and high transit probability. The larger the planet, the higher is the transit detectability (greater transit depth to noise ratio). Within the permissible range of the inclination angle (i) of the orbital plane for transit detection, the transit depth remains almost unchanged with the change in inclination angle. The first exoplanet detected using the transit technique is HD 209458 b that orbits around a solar analog (Charbonneau et al., 2000; Henry et al., 2000).

1.2.2 Radial Velocity (RV) Method

In terms of the number of detections of exoplanets, this method comes right after the transit method (over 800, see Figure 1.2). When a heavy planet orbits around its host star, the center of mass is slightly away from the center of the star depending on the mass of the planet. This causes the star wobble slightly as both of them orbit around their common center of mass. The radial component of this wobble can be perceived through the well known

Doppler spectroscopy. The oscillation in the radial velocity component of the star causes the atomic lines on the spectra to shift on either side of the reference wavelength periodically due to the Doppler effect. Evidently, in order to calculate the line-shifts on the spectra with high precision, this method calls for spectroscopic observation with extremely high resolution as well as high stability of the optical setup. As a result, most of the RV observations are performed in the visible wavelength region around F-K type host stars. Although recently some RV studies have also been performed in the NIR region around the M-type stars and extensive research is ongoing to study RV in the infrared region to detect planets around the late M-type stars and brown dwarfs using the RV technique. This method also requires the planets to be close to their host stars (see Figure 1.1) and the orbital planes to be edge-on. Unlike the transit method this method directly depends on the inclination angle of the orbital plane ($\propto \sin i$). RV method does not calculate the exact mass but gives a lower estimate of the mass. For an orbital inclination equal to i, the RV study provides an estimate of the parameter, $M_P \sin i$ (M_P = actual mass of the planet). The first-ever exoplanet around a star was detected using the RV technique which orbits around a solar-type star named 51 Pegasi in 1995 (Mayor & Queloz, 1995).

1.2.3 Direct Imaging Technique

As the name suggests, using this method the distant and young planets around the host stars can be directly imaged in the mid- and far-infrared. The young planets with age less than 100 Myr emit thermal radiation in the mid- and far-infrared where the emissions from the host stars are not that intense. Even if the stellar emission is comparable to the planets‘ emission, e.g. when the host star is a late M type star or a brown dwarf or when the planet is relatively less heavy, techniques such as coronagraphs are used to block the host stars leaving out the planets. This requires the planets to be at a large distance

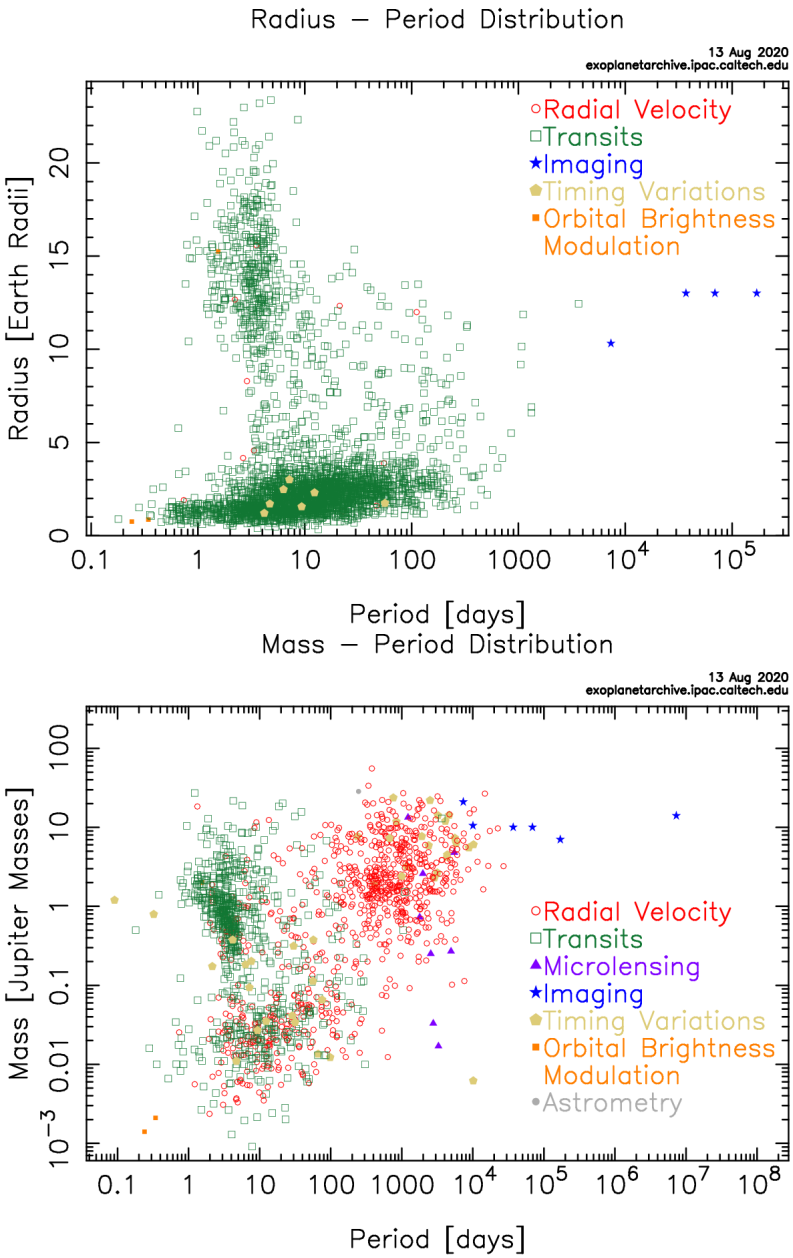

Figure 1.1: The radius-period (left) and mass-period (right) distributions of the confirmed exoplanets detected using different techniques. These show that there are planets whose masses are not known and again, there are planets whose sizes are not known. Source: https://exoplanetarchive.ipac.caltech.edu/exoplanetplots

(current lower limit is ∼2 AU) from the host stars. Also, evolution models suggest that the planets need to be heavy (>4 M_J) and young (<100 Myr) to be self-luminous enough (Burrows et al., 1997). The first exoplanet discovered using this technique is 2M1207 b which is a hot and young planet orbiting around a brown dwarf. To date, 50 planets have been discovered using this

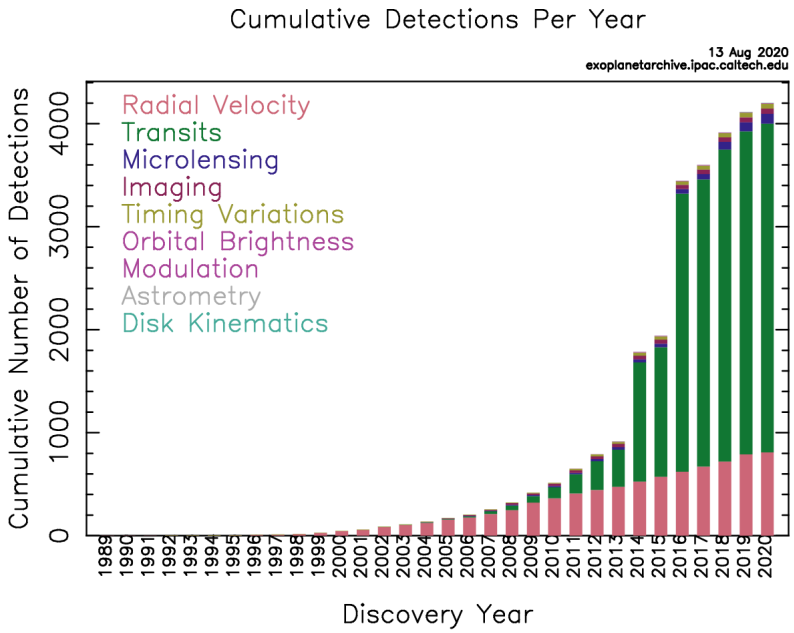

Figure 1.2: Cumulative discovery of the confirmed exoplanets per year using different techniques. Source: https://exoplanetarchive.ipac.caltech.edu/exoplanetplots

method (Figure 1.2).

1.2.4 Timing Variation Method

The timing variation method broadly refers to all the techniques that are used to detect planets by studying the shift in the periodicity of some periodic event pertaining to the host stars or the other planets in the same star-system due to the perturbation created by that planet under study. For example, transit timing variation (TTV) is the variation in the epoch of transit (a slight deviation from strict periodicity) of an already detected planet due to the other planet(s) in the same system. TTV is useful when one or more planets are already detected in a star-system and it is difficult to detect the other further planets using methods like transit or RV due to low signal-to-noise ratio (SNR). However, this method requires the already detected planets (whose transit times are being studied) to be relatively more massive than the planets to be detected and the latter planets to have relatively close orbits for better detection. The first significant detection of a non-transiting planet using this method was of

the planet Kepler-19 c by studying the TTV of the other planet in the same system Kepler-19 b. Another way to study exoplanets is by investigating the transit duration variation (TDV) of an already detected planet caused by an exomoon, apsidal precession for eccentric planets due to another planet in the same system, or general relativity.

Another important technique for the detection of a planet is the pulsar timing variation. The radio wave emission from a pulsar is so regular that slight anomalies can be reflected in the irregularity of its radio emission. Using this principle, the presence of a planet around a pulsar can be studied. The first confirmed discovery using this method was of the planet PSR B1257+12 b in 1992 (Wolszczan & Frail, 1992). This technique provides information about the planets such as mass and semi-major axis of the orbit. However, as these so-called planets around the pulsars form differently from the planets around the regular stars or the brown dwarfs, there is a controversy regarding whether to call these objects orbiting around pulsars as planets.

1.2.5 Gravitational Microlensing Method

Gravitational microlensing is another popular method of detection. More than 80 exoplanets have been discovered using this method. This method is based on the lensing effect of a distant background star by another foreground star when they are almost in the same line with respect to the Earth. If the foreground star harbors a planet, the planet's own gravitational field adds to the lensing effect. Unlike the other methods, this method can detect stellar companions of a wide range of mass (0.005-18 M_J) and in orbits of a wide range of semi-major axis (0.2-18 AU). With current technology, this method is actually capable of detecting an Earth-like planet in an Earth-like orbit around a solar-type star. This method has produced a list of candidates of extragalactic planets, e.g. planet in Andromeda galaxy (An et al., 2004), rogue planets (Dai & Guerras, 2018), etc. However, the main drawback is the requirement for alignment of

two stars and hence, to enhance the detection probability, simultaneous surveys of fields with a large number of stars are conducted like the transit method.

1.2.6 Other Methods

Other existing methods of detection of exoplanets include astrometry (e.g., DENIS-P J082303.1-491201 b), orbital brightness modulation (e.g., Kepler-76 b, Kepler-429 b, etc.), disk kinematics (e.g., HD 97048 b), etc.

There are several methods that can be used for detection and a more detailed study of exoplanets in the near future. These methods include detection of magnetospheric and auroral radio emission; transit imaging using interferometry; direct imaging using interferometry; detection of exoplanets, exomoons, etc. using polarization technique; and so on.

1.3 Study of the Planets with Edge-on Orbits at Different Phases

Detection and characterization of the close-in exoplanets with edge-on orbital orientation can be conducted by studying the periodic variations and modulations in the observed flux from the host stars. These variations are due to either the geometric obscuring effects or the contribution from the planetary flux to the total observed flux. We see the former effect in case of primary transit, secondary eclipse, transit timing variation, transit duration variation, etc. On the other hand, we see the latter effects when we study transmission, reflection, and emission spectra from the planets or the phase curves of the planets. These techniques are elaborated in the following subsections.

1.3.1 Transit, Occultation and Eclipse

Transit, eclipse and occultation are common astronomical events that involve partial or full obscuration of view of a celestial body by another body with

respect to the observer. During a transit event, a celestial body passes directly between another large body and the observer. The foreground object appears to move across the face of the background body as viewed from a vantage point. Examples include the well-known Venus transit and Mercury transit that have been observed and studied for centuries, solar system satellites transiting their parent planets, etc. Eclipse, on the other hand, is a special kind of transit in which, the apparent size of the smaller body transiting the larger body appears to move across by casting the larger body into shadow, as we see in the case of a solar eclipse caused by the passage of the Moon. Again, an occultation is an event in which a foreground object completely blocks the view of a background object from the observer. Studies of occultations of the bright stars by the Moon, the asteroids and the solar-system planets have revealed much information regarding them and also, have led to the discovery of new asteroids.

In the context of exoplanets (also, hereafter in this thesis) a transit event is referred to as the phenomenon of a planet moving across its host star blocking some portion of the starlight when the orbital plane is aligned to our LOS. Half an orbit later, the planet moves behind the host star with respect to the observer, blocking the light only coming from the planet (reflected and/or emitted). This event is known as the secondary eclipse (see Figure 1.3).

1.3.2 Transit Photometry

During a transit event, the passage of the exoplanet in front of the host star can only be perceived as periodic slight dimming of the starlight when captured with an electronic detector and post-processed. Observers take time-series images of a target star over a long span of time (several months to several years) and calculate the flux as a function of time, known as light curves. Periodic short-amplitude fluctuations that follow the transit function formalism are identified as exoplanetary transit events after rigorous modeling and calcu-

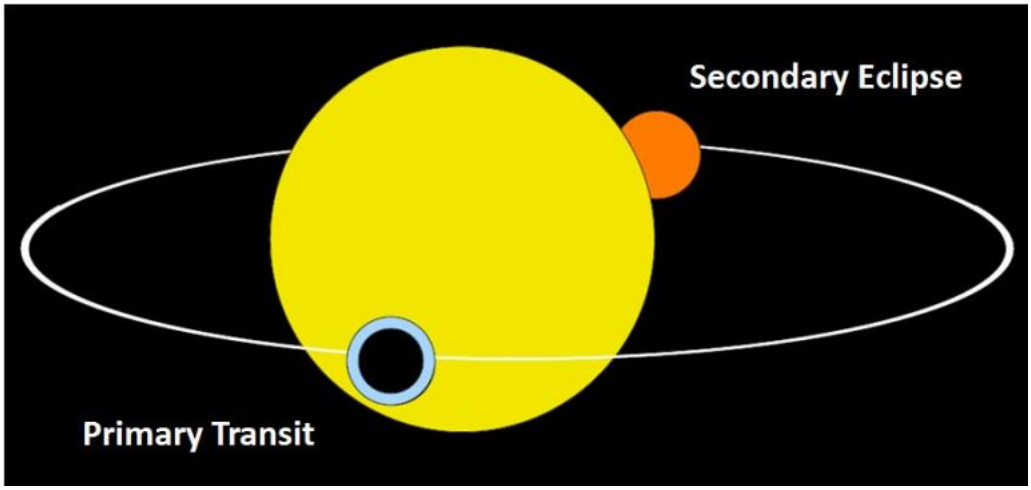

Figure 1.3: Transit and secondary eclipse of a exoplanet. Image Credit: Sara Seager (MIT) and Alexis Smith (Keele University).

lation of transit probability. The maximum depth is directly proportional to the square of the radius ratio, R_P^2/R_*^2, where, R_P and R_* are radii of the planet and the host star respectively. This is the fundamental concept of transit photometry. By modeling the transit light curves, the different parameters and planetary properties can be estimated such as the transit epoch (ingress, mid or egress), the size, the impact parameter, the inclination of the orbital plane with respect to our LOS, the semi-major axis of the orbit, etc. The main challenge lies in achieving the precision both in the calculation of the light curves and the estimation of the planet properties therefrom, since, a giant planet around a solar-type star does not cause a transit depth more than 3% and an Earth-sized or smaller planet around such a star can cause a transit depth as low as several parts per million (PPM). Contaminations such as the systematics (both astrophysical and detector-level), the stellar variability or pulsation (long and short term), the Earth's atmospheric effect in case of ground-based observation, the motion of the space vehicle in case of space-based observation, etc. distort the transit light curves and increase the chances of missing out a detection or of false detection.

Transit photometry can be also be used to conduct TTV and TDV studies.

By regularly recording the transit epochs and transit durations for multiple transit events over a long span of time (e.g., several years), the presence of other bodies in the system can be studied by analyzing the temporal variations in the transit timing and duration of the planet under study.

1.3.3 Photometry at Secondary Eclipse and Phase Curves

During a secondary eclipse, a planet is blocked by its host star. This causes a much smaller dip in the light curves than the transit dip. This happens due to the fact that the planet's reflection and emission are obstructed by the star. This is the basis of the study of phase-dependent modulation of reflection and emission from the exoplanets. As we observe a planet over its full orbit, the planet goes through different phases from fully illuminated (right before or after the secondary eclipse) to fully dark (right before or after transit) and back again. As a result, we detect modulations in the reflection and emission spectra from the planets at different phases which are known as phase curves (Figure 1.4). These phase curves carry information about the albedo and other thermal properties of the atmosphere and/or surface of a planet.

Presently mostly the hot Jupiters are selected for studying the phase curves in the infrared. These studies reveal the thermal re-emission from the atmospheres of the hot giants. As these planets orbit their host stars from close proximity these planets are tidally locked. As a result, the daysides of these planets get heated up by strong irradiation from the host stars. The nightsides also may receive heat due to the advection process depending on how well the heat redistributions are. Planets with high day to night temperature contrast show strong and easily detectable phase modulations. Whereas, planets with low day to night temperature contrast show little to no modulation over phase (almost flat except transit and eclipse dips). Moreover, these phase curves allow probing into the planets‘ longitudinal structures (e.g., Parmentier & Crossfield, 2018). The substellar point on a planet (point exactly opposite

to the star) receives maximum irradiation and is supposed to be the hottest point on the planet. However, the advection process in the atmosphere and the inhomogeneities in the atmospheres cause some shift in the position of the hottest point. In the case of planets where these shifts are negligible, the phase curves peak just before (or after) secondary eclipse and dip just before (or after) transit. However, for planets with significant shifts, the peaks and the troughs of the phase curves exhibit, what is called, phase curve offsets.

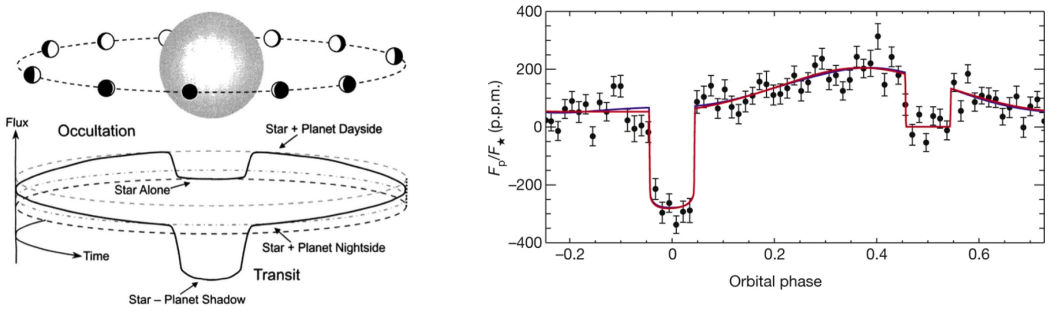

Figure 1.4: Left: Different orbital phases of a close-in tidally locked exoplanet. Image credit: Josh Winn (Princeton University).
Right: Phase curve of 55 Cnc e observed using 75 hours of the Spitzer Space Telescope Infrared Array Camera (Demory et al., 2016).

1.3.4 Transit Spectroscopy

Transit spectroscopy is the study of the transit depth of the exoplanets as a function of wavelength. Spectra of a host star are acquired during and outside the transit events by its planet. The normalized difference between the two types of spectra shows a pattern over wavelength especially at certain absorption lines, which are found to be slightly deeper during transit. This happens due to the preferential absorption of the starlight in the upper layers of the semi-transparent atmosphere by different atoms and molecules present in the atmosphere. Evidently, this method requires the planets to be transiting their host stars and thus to be extremely close to their host stars and have edge-on orbital planes. The main drawback of this method is the constraint on the SNR, which can be enhanced by combining the transit spectra acquired on

multiple transit events. To date, both high-resolution and low-resolution transit spectroscopic data have been acquired for some exoplanets, mostly the hot Jupiters and a few sub-Neptunes and super-Earths. These spectra convey different information about the atmospheres of the planets such as their physical structures, bulk chemical composition, the minor composition of atoms and molecules that actively partake in the absorption and emission of light, cloud or haze structures, etc. However, inferring the properties of the atmospheres of the planets from the observed spectra calls for consistent and detailed theoretical models of planetary atmospheres and their interaction with incident starlight and re-emitted radiation.

1.3.5 Spectroscopy at Secondary Eclipse

Spectroscopy during secondary eclipse allows us to study the albedo and the thermal properties of the exoplanets as a function of wavelength. Just as transit spectroscopy, spectra of the host stars are recorded before (or after) and during the secondary eclipse events and the normalized difference is calculated. In the optical wavelength region, it gives information about the wavelength-dependent reflectivity of the atmospheres (also, the reflectivity of the planetary surfaces, for terrestrial planets). On the other hand, eclipse spectra acquired in the infrared region give information regarding the wavelength-dependent thermal emission from the planets. Both can tell us about the atmospheric compositions of the planets.

1.4 Overview of Global Missions for Exoplanets

Since the discovery of the first transiting planet using a ground-based telescope dedicated to the discovery of exoplanets, there have been many ground-based and space-based missions proposed and commissioned aimed at the detection

and characterization of exoplanets.

1.4.1 Dedicated Missions for Detection of Exoplanets Using Transit Method

In 1992 NASA proposed the first global dedicated mission to search for exoplanets, namely FRESIP (FRequency of Earth-Size Inner Planets). However, this mission faced several setbacks and delays until it was finally launched in 2009 while the name was changed to Kepler Space Telescope. Meanwhile, several ground-based dedicated telescopes were already commissioned and operational for exoplanet surveys such as HATNet, WASP, TrES, XO, etc.

1.4.1.1 Space-Based Missions

- **Kepler:** Kepler space telescope had an effective aperture of 0.95 m and a fixed field of view (FOV) of 115 deg^2 on-sky. It stared at the same field on-sky until 2013 before it lost its ability of continuous monitoring with the loss of two reaction wheels. In this span, Kepler discovered 2342 confirmed planets with sizes ranging from as small as Earth to about twice the size of the Jupiter and produced a list of 2418 planetary candidates that are yet to be confirmed[1]. Kepler has discovered many Earth-sized planets which are now prime candidates for being habitable. The targets that were in the field of its spacecraft can be publicly accessed from the Kepler Input Catalog (KIC) and they can be identified as KIC followed by a unique number (e.g., KIC 8462852, also known as Tabby's star). If one or more transit events were detected around one of the targets, then that star has been enlisted in the Kepler Object of Interest (KOI) catalog designated as KOI followed by a unique number (e.g., KOI-377, also known as Kepler-9) and to identify the suspected planets from the detected transit events, the KOI name of the star is added with 2 digit

[1] *Taken from* https://exoplanetarchive.ipac.caltech.edu

decimal at the end in the chronological order of discovery starting from 01 (e.g. KOI-377.01, KOI-377.02, etc). When a planet is confirmed then its host star is identified as Kepler followed by a unique number and the planets are 'identified using the usual lower case letters starting from 'b' (e.g., Kepler-9b, Kepler-9c, Kepler-9d in the chronological order of discovery).

- **K2:** After the loss of two reaction wheels, Kepler's regular operation was discontinued in 2013 and a new mission leveraging Kepler's remaining capabilities was started named K2 with less photometric SNR. The K2 mission involved a series of sequential observing "Campaigns" of fields distributed around the ecliptic plane and each campaign was limited by Sun angle constraints to a duration of approximately 80 days. Followed by the test campaign (Campaign 0) 19 campaigns were conducted before the service was discontinued forever in 2018. Over these campaigns, K2 has discovered 410 planets which are confirmed and 889 planetary candidates have been detected which are yet to be confirmed[2]. Just as Kepler, the targets in the field of view are included in the Ecliptic Plane Input Catalog (EPIC) and a target can be identified as EPIC followed by a unique number (e.g., EPIC 211945201). A planet discovered by K2 is designated as K2 followed by a unique number followed by a lower case letter (e.g., K2-3b).

- **CoRoT:** CoRoT stands for Convection, Rotation et Transits planétaires in French or Convection, Rotation and planetary Transits in English. This mission was led by the French Space Agency (CNES) in conjunction with the European Space Agency (ESA) and other international partners. This was operational between 2006 and 2013. The telescope on board had a diameter of 27 cm and a field of view of 2.7° by 3.05° on-sky. It has discovered more than 100 planets of size ranging from super-Earths to

[2] *Taken from* https://exoplanetarchive.ipac.caltech.edu

about twice the size of the Jupiter.

- **TESS:** The Transiting Exoplanet Survey Satellite or TESS is a part of NASA's Explorers program and is jointly operated by NASA and Massachusetts Institute of Technology, USA. TESS was launched in 2018. TESS surveys the entire sky by breaking it up into 26 different sectors, each 24° by 96° across. Four cameras on the spacecraft, each of 100 mm effective pupil diameter and 24° by 24° field of view on-sky, stare at each sector for at least 27 days. The planned life span is 2 years. To date, TESS has discovered about 70 confirmed planets and more than 1300 planetary candidates which are yet to be confirmed. Each of the TESS targets has a TESS Input Catalog (TIC) ID and the detected planets (both confirmed and candidates) have TESS Objects of Interest (TOI) IDs (e.g., TOI-700b, TOI-700c, TOI-700d).

1.4.1.2 Ground-Based Missions

- **HATNet and HATSouth:** The Hungarian-made Automated Telescope Network (HATNet) Exoplanet Survey is a geographically distributed network of 7 small telescopes optimized for detecting transiting exoplanets. HATNet telescopes are located at the Fred Lawrence Whipple Observatory (FLWO) at Mount Hopkins in Arizona, USA (5 telescopes), and the Mauna Kea Observatory in Hawaii, USA (2 telescopes). The network uses 200 mm lenses and CCDs to seamlessly monitor the sky over the better part of 24 hours leveraging the large separation in longitude. It has been operational since 2003 and till date, it has discovered more than 60 exoplanets. The planets discovered by the HATNet project are designated as HAT-P- followed by a unique number and a lower case letter (e.g., HAT-P-36b).

  The Hungarian-made Automated Telescope Network-South (HATSouth) Exoplanet Survey is a network of 6 astrograph telescope systems designed

to detect transiting exoplanets in orbit around relatively bright stars visible from the southern hemisphere. The telescopes are situated in Chile, Namibia and Australia, each of 180 mm in diameter. This network also can seamlessly monitor the sky over the better part of 24 hours. This network has been operational since 2009 and till date, it has discovered more than 70 planets. The planets discovered by HATSouth are designated as HATS- followed by a unique number and a lower case letter (e.g., HATS-18b).

- **WASP:** Wide Angle Search for Planets or WASP is an exoplanet detection program composed of the Isaac Newton Group, IAC and six universities from the United Kingdom. WASP consists of two robotic observatories: SuperWASP-North at Roque de los Muchachos Observatory on the island of La Palma in the Canaries, Spain and WASP-South at the South African Astronomical Observatory, South Africa. Each observatory consists of an array of eight Canon 200 mm lenses and CCDs. The project began in 1999 and till date, over 150 planets have been discovered by WASP. The planets discovered by WASP are designated as WASP- followed by a unique number and a lower case letter (e.g., WASP-12b).

- **TrES and KELT:** The Trans-atlantic Exoplanet Survey, or TrES, used three 4-inch (10 cm) telescopes located at Lowell Observatory, Palomar Observatory, and Teide Observatory to locate exoplanets. It started its operation in 2003 and has discovered 5 exoplanets. It is no longer operational. The planets discovered by TrES are identified as TrES- followed by a unique number and a lower case letter (e.g., TrES-1b).

  The Kilodegree Extremely Little Telescope (or KELT) consists of two telescopes: one is KELT-North, located at Winer Observatory in Arizona, USA and the other is KELT-South, located at the Sutherland observing station of the South African Astronomical Observatory (SAAO). Each has a 42 mm lens and a CCD covering 26° by 26° on-sky. In March 2020,

the KELT transit search was concluded and till then KELT discovered 26 planets which are identified as KELT- followed by a unique number and a lower case letter (e.g., KELT-1b).

- **TRAPPIST and SPECULOOS:** The Transiting Planets and Planetesimals Small Telescope (TRAPPIST) is a group of two Belgian Telescopes, viz., TRAPPIST–North situated at the Oukaïmeden Observatory, Morocco, operating from 2016 and TRAPPIST–South at ESO's La Silla Observatory, Chile, operating from 2010. Till date, seven Earth-sized planets have been discovered around the host star TRAPPIST-1 (Gillon et al., 2016, 2017). SPECULOOS (Search for Planets EClipsing ULtracOOl Stars) project aims to detect terrestrial planets eclipsing some of the smallest and coolest stars of the solar neighborhood. It is based on a network of robotic telescopes whose main cores are the observatories, viz. SPECULOOS South in Chile (4 telescopes) and SPECULOOS North in Tenerife (1 telescope), complemented by the SAINT-EX (1 telescope in Mexico) and TRAPPIST.

- **Others:** Other ground-based facilities include XO, MASCARA, KPS, etc. So far, the XO project has discovered 6 confirmed planets. MASCARA (Multi-site All-Sky CAmeRA), a project maintained by the Leiden University, has till now discovered 2 confirmed planets. The Kourovka Planet Search (KPS) project has discovered 1 confirmed planet till date along with several candidates.

1.4.2 Existing Facilities Used for Characterization of Exoplanets

Characterization of exoplanets requires telescopes of large aperture. So far the pre-existing large-aperture telescopes have been used for this purpose.

1.4.2.1 Space-Based Telescopes

- **Hubble Space Telescope:** Hubble Space Telescope or HST is a space telescope that was launched in 1990 and has been one of the largest and most versatile telescopes ever since. It is jointly operated by NASA, ESA and Space Telescope Science Institute (STScI). It has a 2.4 m mirror and it can be used to observe in the ultraviolet, visible, and near-infrared regions. Transit photometric observations are been carried out in the optical wavelengths using the Space Telescope Imaging Spectrograph (STIS) instrument and in the infrared region using the Wide Field Camera (WFC3) instrument. STIS and WFC3 instruments are also used to carry out NUV and Infrared spectroscopy respectively. The other instrument namely Near Infrared Camera and Multi-Object Spectrometer (NICMOS) has also been used to observe exoplanets until it was put on hibernation in 2009.

- **Spitzer Space Telescope:** The Spitzer Space Telescope was an infrared space telescope operational between 2003 and 2020. It had a primary of 0.85 m diameter. It was jointly operated by NASA and the California Institute of Technology (Caltech). The Infrared Array Camera (IRAC) on board has been used to perform photometric observation of exoplanets in the mid-infrared regions (3.6 μm , 4.5 μm , 5.8 μm and 8 μm).

1.4.2.2 Ground-Based Telescopes

There are several large aperture (diameter $>$ 1 m) telescopes around the globe that have been used in the characterization of exoplanets. These telescopes were already used in other fields of astronomy. After the discovery of the first transiting planet (Charbonneau et al., 2000; Henry et al., 2000) these telescopes are being used to study the exoplanets using techniques such as transit spectroscopy, eclipse spectroscopy, infrared phase curves etc. These include the 8.2 m Very Large Telescope (VLT) in Chile with the instruments

at the backend such as the Focal Reducer and Low Dispersion Spectrograph (FORS1/FORS2), the Cryogenic Infrared Echelle Spectrograph (CRIRES), the Echelle Spectrograph for Rocky Exoplanet- and Stable Spectroscopic Observations (ESPRESSO), etc.; the 10 m Hobby–Eberly Telescope (HET) at the McDonald Observatory in USA with the instruments at the backend such as the High-Resolution Spectrograph (HRS), etc.; the 3.5 m telescope at the Calar Alto Observatory in Spain used as a part of the CARMENES (Calar Alto high-Resolution search for M dwarfs with Exoearths with Near-infrared and optical Echelle Spectrograph) survey, etc.

1.4.3 Upcoming Missions

There are a number of space-based missions and ground-based telescopes under development or planned for operation dedicated to the study of exoplanets or exoplanetary research being one of the major science goals.

1.4.3.1 JWST

The James Webb Space Telescope (also known as JWST or Webb) is an upcoming infrared observatory that will complement and extend the discoveries of the Hubble Space Telescope. Presently it has been decided to be launched on 31 October 2021. It has a primary of 6.5 m diameter and it will cover the wavelength range from 0.6-28 μm . The primary instruments on board that will be engaged in the study of exoplanets are the Near-Infrared Camera (NIRCam) for both imaging and low-resolution spectroscopy over the wavelength range 0.6-5 μm , the Near-Infrared Spectrograph (NIRSpec) that will allow multi-object spectroscopy in the wavelength range 0.6-5.3 μm , Near-Infrared Imager and Slitless Spectrograph (NIRISS) that will allow low-resolution wide-field grism spectroscopy; medium-resolution grism spectroscopy; aperture masking interferometry; and parallel imaging through filters matched to those available with NIRCam over the wavelength range 0.6-5 μm , and the Mid-Infrared In-

strument (MIRI) for both imaging and low-resolution spectroscopy over the wavelength range 4.9-28.8 μm .

1.4.3.2 ARIEL

The Atmospheric Remote-sensing Infrared Exoplanet Large-survey (ARIEL) is a space telescope that is going to be a part of the European Space Agency's Cosmic Vision programme. It will be a dedicated mission for the study of exoplanets. It will be observing at least 1000 known exoplanets using the transit method and characterizing the planets' chemical composition and thermal structures through transit and eclipse spectroscopy. The telescope will use an oval 1.1 $\times$ 0.7 m primary mirror and operate in the visible and near-infrared spectrum. It is planned to be launched in 2028.

1.4.3.3 PLATO

The PLAnetary Transits and Oscillations of stars (PLATO) is a space telescope under development by the European Space Agency dedicated to the discovery of planets especially the earth-like planets in the habitable zone (where water can exist in a liquid state) around sun-like stars. The goals are to search for planetary transits across up to one million stars and to discover and characterize rocky extrasolar planets around yellow dwarf stars (like our sun), subgiant stars, and red dwarf stars. It is planned to be launched in 2026. There will be 26 telescopes on board, each having a diameter of 120 mm and operate in the optical wavelengths (0.5-1 μm).

1.4.3.4 TMT and ELT

The Thirty Meter Telescope (TMT) and the Extremely Large Telescope (ELT) are the two upcoming ground-based largest telescopes with aperture diameters of 30 m and 39.3 m respectively. The ELT is being organized and will be operated by the ESO. The TMT International Observatory LLC (TIO), a non-profit organization, was established in May 2014 to carry out the construction and

operation phases of the TMT Project. The Members of TIO are Caltech, the University of California, the National Institutes of Natural Sciences of Japan, the National Astronomical Observatories of the Chinese Academy of Sciences, the Department of Science and Technology and the Department of Atomic Energy of India, and the National Research Council (Canada). The Association of Universities for Research in Astronomy (AURA) is a TIO Associate. Major funding has been provided by the Gordon & Betty Moore Foundation. The Aryabhatta Research Institute for Observational Sciences (ARIES), Nainital, the Indian Institute of Astrophysics (IIA), Bangalore and the Inter-University Center for Astronomy and Astrophysics (IUCAA), Pune are the three main institutes constituting TMT-India. Both of these telescopes can be engaged in the photon-starved studies of exoplanets such as direct imaging, radial velocity, gravitational microlensing and high-resolution transmission and reflection and emission spectroscopy (Frazin, 2019; Tanner & Crossfield, 2014). Owing to the extremely large apertures of the telescopes, the high-resolution absorption and emission features of the planetary atmospheres on those spectra can convey precise information about the atomic and molecular abundances of the planetary atmospheres, physical effects that impact the intrinsic shape of atmospheric lines such as wind patterns, atmospheric circulation, planetary rotation, pressure broadening, etc., and also about the high-altitude atmospheric layers, which may be undetectable at low spectral resolution because of clouds or hazes that partly suppress the spectral features (Martins et al., 2018; Skemer, 2019). Also, both have capabilities of detection of polarization of light with ELT having much better sensitivity than TMT and hence, they can be used for the polarization-based detection and characterization of exoplanets (Anche et al., 2015; Atwood et al., 2014; Keller et al., 2010) as lights from both the directly imaged planets and the close-in giants are likely to be polarized due to various physical effects (Marley & Sengupta, 2011; Sengupta, 2008, 2013, 2018; Sengupta & Marley, 2016; Stam et al., 2006, etc.).

1.5 Outline of Thesis

Chapter Two: Transit Photometric Observations

This chapter describes the motivation behind the inception of regular transit photometric observation using the Indian Astronomical facilities. The details of the telescopes and their back-end instruments and the observing strategies for precise photometry are discussed here. The details of the two types of observations, viz., survey and follow-up observations, are explained in this chapter along with results. We have also briefly described here the properties of the host stars that we followed up such as TRAPPIST-1, WASP-33, WASP-50, HATS-18, etc. Finally, the caveats in this technique, which we focused on and worked on, are summarized at the end of the chapter.

Chapter Three: Analysis and Modeling of Transit Photometric Data

This chapter focuses on state-of-the-art techniques of analysis, processing and modeling of transit photometric data applied by us to obtain precise results. This chapter briefly discusses the details of the pipelines we developed for different stages of photometry such as for reduction and processing, namely `pyapphot` (available on Github) and for modeling of transit light curves (not made open-source yet). The different sources of noise are discussed here along with the details of how we segregated the noise and treated them with techniques such as wavelet denoising, baseline detrending and Gaussian process regression. The modeled transit light curves and the tables containing the transit parameters calculated from the entire process are presented here.

Chapter Four: Transit Spectroscopy

This chapter explains the different methods of observation and modeling of low-resolution and high-resolution transit (or, transmission) spectroscopic data. The details of our high-resolution transit spectroscopic observation are presented here along with the results. The underlying principles and calculations associated with the theoretical modeling of transmission spectra are elaborated here step by step. Finally, some basic models of transmission spectra are pre-

sented in this chapter.

Chapter Five: Detailed Modeling of Transmission Spectra in the Optical

This chapter discusses the methods associated with our detailed modeling of the optical transmission spectra. In contrast to the existing models which only consider the effect of extinction of the light coming from the host stars in the planetary atmospheres, we present here more accurate models of transmission spectra by incorporating the effect of diffused transmission due to scattering in the atmospheres. The basic formalisms involving the solution of radiative transfer equations and numerical techniques adopted are explained here. We also present here the results obtained from benchmarking and comparing our models with the archival observed transit spectroscopic data of some close-in giant exoplanets.

Chapter Six: Detailed Modeling of Transmission Spectra in the Infrared

This chapter focuses on the effects of the emission from the night sides of the close-in Jupiter-sized planets on their transmission spectra. The basic formalisms of calculating the thermal emission and incorporating it in the expression for transmission spectra are explained here. Also, we present here the different case studies to assess the significance of the effect of the thermal emission for different properties of the planets and the host stars and for different observing modes. For the calculation of the significance, we have calculated the noise levels and simulated observational data in the infrared to be obtained from the upcoming James Webb Space Telescope. Details of these simulations are explained in this chapter.

Summary

Here we summarize the entire work explained in this thesis, demonstrating our significant contribution towards the scientific community.

Chapter 2

Transit Photometric Observations[1]

2.1 Introduction

Transit photometry is based on the most familiar physics of eclipse. In the context of exoplanets, when an extra-solar planet passes directly between its host star and an observer, it is called a transit event. The planet appears to move across the face of the larger body as viewed from a vantage point and blocks some portion of the light coming from the host star. When the event is recorded with a sensitive camera and the images are post-processed, the periodic dimming of the starlight can be detected, which can be attributed to the presence of a companion. Observers take time-series images of a target star over a long span of time (several months to several years) and calculate the flux (or magnitude) as a function of time. Periodic short-amplitude fluctuations are detected using techniques such as the Lomb-Scargle periodogram (Lomb, 1976; Scargle, 1982), box least squares (BLS) periodogram (Kovács, Zucker, & Mazeh, 2002) etc. The presence of a planet is only confirmed after rigorous modeling of the transit light curves with the transit formalism of Mandel & Agol (2002) and calculation of the transit probability. Besides detection, long-

[1] *Part of this chapter is published in The Astronomical Journal, Chakrabarty and Sengupta, vol. 158:39, 2019.*

term transit photometric observations help us estimate the different properties of the transiting planets precisely along with the understanding of the orbital dynamics.

2.2 Overview of Previous Works

Mercury transit and Venus transit are the most common examples of transit events that have been studied by the astronomers for centuries to excavate much key information about the solar system. Rosenblatt (1971) first proposed the idea of detecting the extra-solar planets using the transit method. However, the lack of a suitable low-noise detector rendered the idea unimplementable until 1999. In 1999 research teams led by David Charbonneau and Greg Henry independently detected planetary transit events across a solar-type bright star (V-band magnitude$\sim$8) HD 209458 for the first time (Charbonneau et al., 2000; Henry et al., 2000). After that many ground-based facilities such as WASP, HATNet and HATSouth, TrES, etc. and a space-based mission namely CoRoT were commissioned aimed at the search for exoplanets. Initially mostly close-in Jupiter-sized or larger planets were being discovered such as OGLE-TR-56 b (Konacki et al., 2003), TrES-1 b (Alonso et al., 2004), XO-1 b (Wilson et al., 2006), HAT-P-1 b (Bakos et al., 2007), WASP-1 b (Collier Cameron et al., 2007), CoRoT-1 b (Barge et al., 2008), etc. which are somewhat similar to HD 209458 b and all of these planets belong to the class of hot Jupiters. Later a few mini-Neptunes and super-Earths were discovered using the transit method such as GJ 436 b (Pont et al., 2009), ,CoRoT-7 b (Queloz et al., 2009) GJ 1214 b (Charbonneau et al., 2009), HAT-P-11 b (Bakos et al., 2010), etc. Once Kepler was launched in 2009, Kepler and K2 discovered planets of different sizes ranging from smaller than Earth to about twice the size of the Jupiter including several multi-planetary systems. Kepler-10 b was the first rocky exoplanet (radius$\sim$1.4 $R_{\oplus}$) discovered (Batalha et al., 2011). The first ground-based discovery of rocky planets was the multi-planetary system around

TRAPPIST-1, where 7 Earth-sized (b-h) planets were discovered around the M8 type host star (Gillon et al., 2016, 2017). Till date, over 4200 planets have been discovered, but it is just a tiny fraction of the stars in our galaxy. Also, it has been realized that the follow-up of the already detected planets is extremely called-for to precisely determine the properties of the planets from the transit observations. However, a significant number of confirmed planets either are followed up zero to few times or show poor precision or conflicting results on their repeated follow-ups. This calls for the large aperture telescopes (aperture $>$ 1 m) around the globe to be engaged in follow up observation of the confirmed planets.

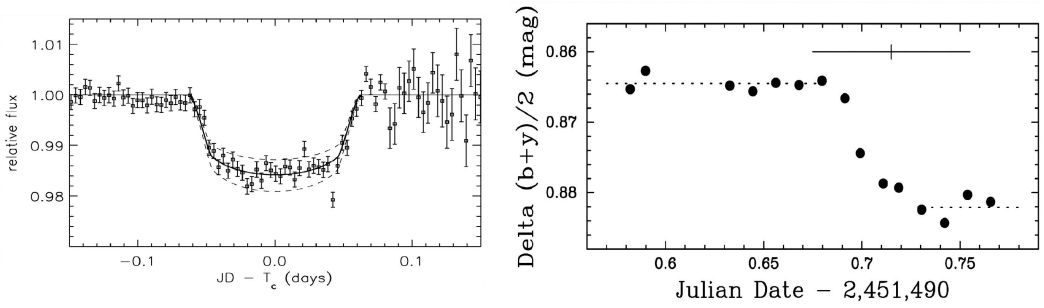

Figure 2.1: The first-ever detection of a transiting exoplanet. The transit detection and the corresponding light curves for the planet HD 209458 b were reported by two groups almost at the same time: Charbonneau et al. (2000) (left) and Henry et al. (2000) (right).

2.3 Engaging Indian Astronomical Facilities in Regular Transit Observations

India with nationwide observatories consisting of modern big-budget large-aperture telescopes and low-noise detectors is well-suited for studying exoplanets. The main requirement for transit photometry is the low-noise precise detectors such as the charge-coupled devices (CCDs). The aperture requirement depends on whether it is a survey aiming for the detection of planets or a follow-up observation aimed at the characterization of planets. The former

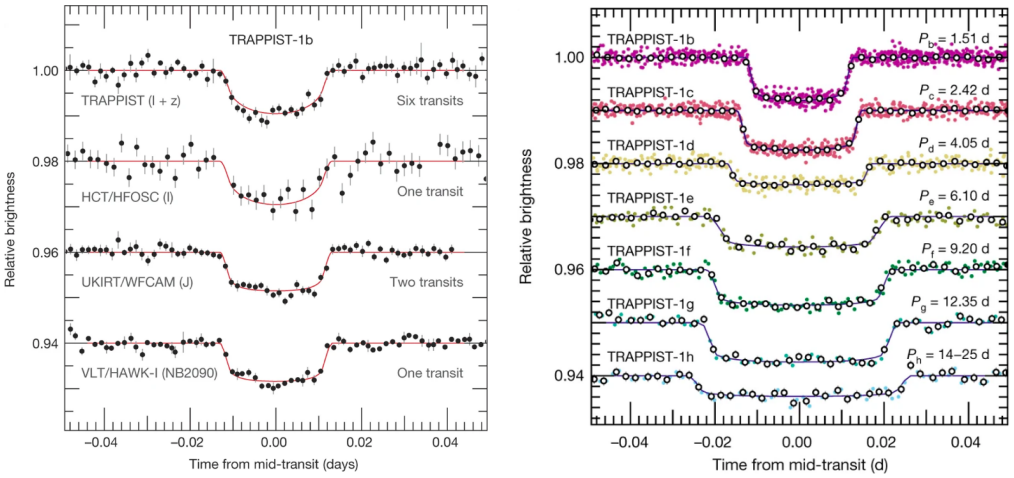

Figure 2.2: Left - Transit light curves corresponding to the detection of the Earth-sized planet TRAPPIST-1 b around an M dwarf by Gillon et al. (2016). The second light curve from the top corresponds to the observation made from HCT, IAO, India on 18 Nov 2015. Right - Transit light curves of seven Earth-sized planets (including the 'b' planet) around the same star detected and reported by Gillon et al. (2017).

would require a large field of view (FOV) on-sky and continuous monitoring, for which a small or medium aperture ($\lesssim$1 m) telescope is more favorable. On the other hand, characterization of exoplanets requires high-precision observation for high SNR, and for this purpose large-aperture telescopes are favored. The aperture requirement also depends on how readily available the facilities are for transit observation, as repeatability (for both high SNR and better estimation of the period) is one of the key requirements of transit observation. In this regard, the telescope facilities controlled and maintained by the Indian Institute of Astrophysics (IIA) of 1-2 m class are well-suited.

Moreover, in order to observe a transient event like a transit, coordinated observations around the globe have already been proven to be highly effective by ensuring the coverage of a transit event regardless of its ephemeris of occurrence. In this regard, the astronomical facilities of IIA such as the Indian Astronomical Observatory (IAO, 78° 57′ E, 32° 46′ N) and the Vainu Bappu Observatory (VBO, 78° 50′ E, 12° 34′ N) can fill in the missing longitudinal coverage. For this reason, the group involved in the TRAPPIST mission conducted a one-night observation from the 2 m Himalayan Chandra Telescope

(HCT) situated at IAO as a part of the detection and confirmation of the Earth-sized planet TRAPPIST-1 b. This was the first time an Indian facility was involved in a global transit photometric observation. We acquired the raw data from the principal investigator (PI) of the group and reduced and analyzed the data to produce the transit light curve of TRAPPIST-1 b. After modeling the light curve (see Section 3.3), we estimated the transit parameters which were within 1 σ error-bar of the parameters determined by Gillon et al. (2016). This motivated us to continue the search and follow-up observations using HCT and other facilities of India. The facilities are described in the next section.

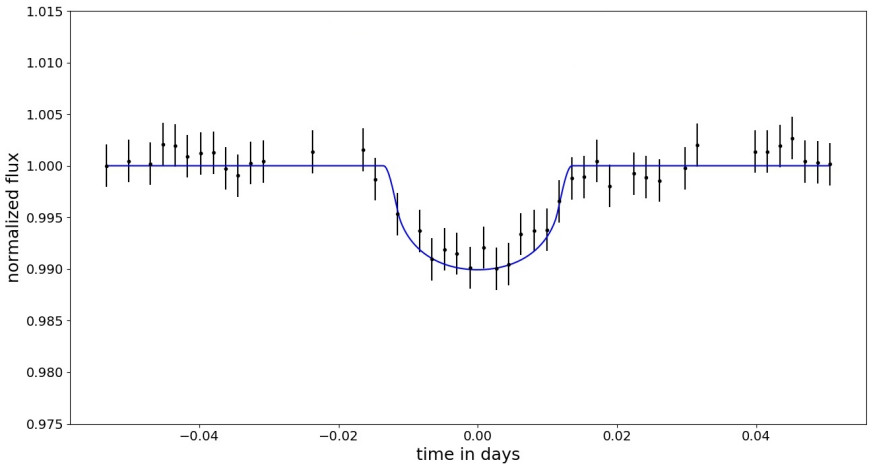

Figure 2.3: Transit light curve of TRAPPIST-1 b. Observation was made from HCT, IAO, India by Gillon et al. (2016) on 18 Nov 2015. We independently reduced the data and performed differential photometry to produce the light curve data shown with errorbar in black. We modeled the data with the transit function of Mandel & Agol (2002) using MCMC to get the distributions of the transit parameters. Model corresponding to the median of the parameter distributions is shown in blue.

2.4 Details of Observing Facilities Used

We observed the transit events by using the 2-meter Himalayan Chandra Telescope (HCT) at Indian Astronomical Observatory (IAO), Hanle and the 1.3-meter Jagadish Chandra Bhattacharyya Telescope (JCBT) at Vainu Bappu Observatory (VBO), Kavalur. Being a doctoral student affiliated with IIA, I

have regular access to the telescopes of IIA by submitting proposals every cycle (a year consists of 3 cycles). These proposals are examined and accordingly observation times are granted by time allocation committees (TAC) assigned for each telescope, viz. HTAC and VTAC for facilities in IAO and VBO respectively.

For HCT we used the back-end instrument Hanle Faint Object Spectroscopic Camera (HFOSC) which has a $2K \times 2k$ optical CCD as the imager with a field of view of $10' \times 10'$ on-sky. In the case of JCBT, we used the $2k \times 4k$ UKATC optical CCD as the imager with a field of view of $10' \times 20'$ on-sky. Bessel V, R, and I filters were used for the observations. Both the imagers have a plate-scale of $3''$/pixel and both are liquid Nitrogen cooled to make the dark noise negligible. In order to obtain multiple transit light curves, each target has been observed repeatedly. Some of the observed frames had to be discarded as they were affected by either passing cloud or due to the condensation of water on the CCD.

Figure 2.4: The 1.3 m Jagadish Chandra Bhattacharyya Telescope (JCBT) at the Vainu Bappu Observatory (VBO), Kavalur, India. Left - the dome. Right - the telescope. Image Credit: Prasanna Deshmukh (IIA).

Figure 2.5: The 2 m Himalayan Chandra Telescope (HCT) at the Indian Astronomical Observatory (IAO), Hanle, India. Left - the dome. Right - the telescope. Image Credit: Prasanna Deshmukh (IIA).

2.5 Survey Operation

We first engaged the HCT and the JCBT in survey operation aiming to detect planets around stars with no reported confirmed or candidate planet. This was difficult as we do not have continuous access to the telescopes unlike the groups involved in dedicated planet-hunting missions have. Also, we can only observe during nights in India for not being part of a coordinated search. Above all, many nights get wasted because of the presence of clouds. Hence, we have adopted a strategy to monitor the different parts of the sky as explained in Section 2.5.2.

2.5.1 Goals

The main goal of our survey operation is to regularly monitor different parts of the sky to detect new planets around stars with no reported planet. This survey operation also helps us assess the capability of these telescopes in tran-

sit observation. The first steps include getting familiar with the site condition (seeing, transparency, cloud coverage etc.); optimizing observational parameters for transit observation; etc. Experience from regular survey operations helps us prepare our targets and observation strategy for follow-up of transit events of already discovered planets. Moreover, these observations also help us assess the stability of the systems that get reflected in the light curves. We study the light curves with no traits of planetary transits to assess whether the fluctuations in the light curves are significantly less than the transit depth (<1%) we attempt to detect. This is used to characterize the baselines of the transit light curves.

2.5.2 Procedure

We observe different parts of the sky with crowded fields or fields containing star clusters over 3-4 consecutive nights. If we do not get a transit signal we move to another field. This way we increase our survey space so as to maximize the probability of detection. We choose bright stars as targets. We avoid the fields on-sky where the telescopes such as Kepler, K2, WASP, HATNet, CoRoT, etc. have once stared, as the possibility of the presence of a planet around a bright star in those fields have already been ruled out. Moreover, we avoid the stars with reported variability and binary companion to minimize the chance of false positive. We ensure that our target fields contain stars with a V-band magnitude of 8-18 when observing from HCT and 6-14 when observing from JCBT. The lower limit (brighter side) is set by shutter speed and the upper limit (fainter side) is set by the transit duration and number of data points required within that time. Targets are slightly defocused to reduce the jitter effect, especially for bright stars to avoid saturation. Autoguider is always kept on during observation which would reduce the pixel drift minimizing the flat-field noise.

Details of the point spread function (PSF): The full-width half maxi-

mum (FWHM) of the PSF is maintained between 6 and 10 pixels corresponding to 2″-2.6″on-sky. The ellipticity is maintained below 0.15 so that the extraction of aperture produces the least error. By using the autoguider the ratio of the drift in PSF position on CCD (in pixel) to the FWHM (in pixel) is less than 1. The average jitter ratio is about 0.6.

Table 2.1: Parameters quantifying the fluctuations in the light curves with no transit signal

Date	Parameters	TYC 3337-1778-1	TYC 3337-1676-1	TYC 3337-83-1
04 Jan 2019	fluctuation (%)	0.12 ± 0.007	0.16 ± 0.01	0.16 ± 0.01
	PSNR	865 ± 55	639 ± 43	714 ± 61
05 Jan 2019	fluctuation (%)	0.14 ± 0.01	0.12 ± 0.009	0.16 ± 0.01
	PSNR	713 ± 63	872 ± 71	605 ± 40
06 Jan 2019	fluctuation (%)	0.15 ± 0.01	0.13 ± 0.01	0.18 ± 0.02
	PSNR	655 ± 70	765 ± 74	563 ± 52
08 Jan 2019	fluctuation (%)	0.16 ± 0.009	0.18 ± 0.007	0.26 ± 0.01
	PSNR	642 ± 41	552 ± 21	394 ± 22

Note. The value of each parameter is shown along with 1-σ error margin. Also, some of the values are shown as −, which implies that no observation of that star has been made on that day.

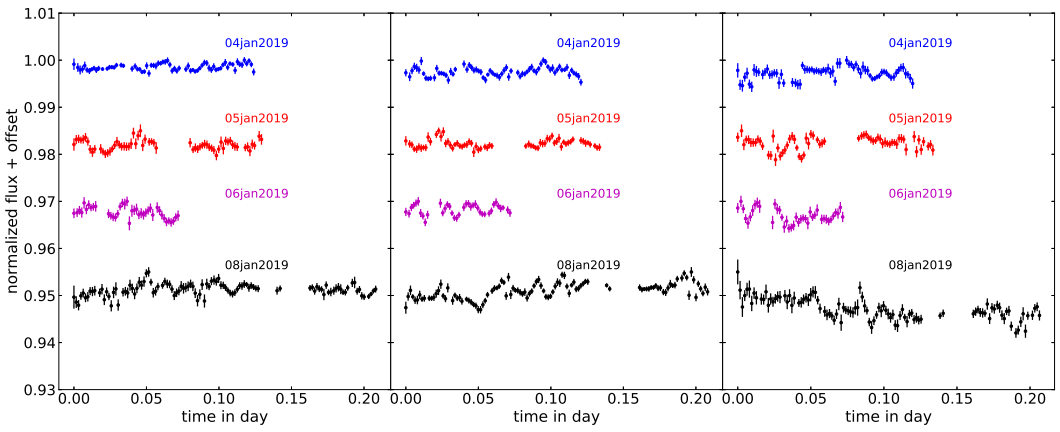

Figure 2.6: Light curves of the stars TYC 3337-1778-1, TYC 3337-1676-1, and TYC 3337-83-1 (from left to right), respectively, observed from JCBT. The zero points on the time axes for the dates 2019 January 4, 5, 6, and 8 are set at BJD-TDB 2458488.096490033, 2458489.094740324, 2458490.231318539, and 2458492.054523, respectively.

2.5.3 Results and Discussion

The results of some of the survey operations are shown in Figure 2.6. Clearly, the light curves show very little fluctuation with no trace of any detectable transit event. With the current noise levels, we can at most rule out the

possibility of any transit by a close-in Jupiter-sized planet within the duration of observation and cannot comment on the presence of any sub-Neptunian planet. The fluctuations (in %) and the peak signal-to-noise ratio (PSNR) values for the light curves are tabulated in Table 2.1.

2.6 Follow-up Observation

We conduct follow up observation of the already detected planets. We engaged the Indian telescopes in active follow-up transit observation to demonstrate the capability of Indian telescopes to be a part of the global hunt. We presently focus only on the close-in giant planets. Owing to the large aperture and our state-of-the-art processing and modeling algorithms we update the properties of the planets with precise values. We have published the first set of results for five hot Jupiters, viz., WASP-33 b, WASP-50 b, WASP-12 b, HATS-18 b and HAT-P-36 b in the peer-reviewed journal, The Astrophysical Journal (Chakrabarty & Sengupta, 2019). The results for these planets are available on the publicly-accessible websites for exoplanets such as NASA Exoplanet Archive[2], The Extrasolar Planets Encyclopaedia[3], etc. Currently, the Planetary Systems databse[4] (also, the retiring Confirmed Planets database) and the Overview page on NASA Exoplanet Archive shows our publication as the default reference i.e. the reference for default parameters of those five hot Jupiters as it qualified the criteria for inclusion in the archive as default reference based on number and precision of the parameters.

2.6.1 Goals

The primary goal of the follow-up observation is to update the parameters such as the mid-transit epoch (T_{cen}), the planet radius (R_P), the orbital separation

[2] https://exoplanetarchive.ipac.caltech.edu

[3] http://exoplanet.eu

[4] https://exoplanetarchive.ipac.caltech.edu/cgi-bin/TblView/nph-tblView?app=ExoTbls&config=PS

(a), the inclination angle (i), the impact parameter ($b = a\cos i/R_*$, R_* being the host star radius), etc. with precise values (small 1-σ error-bars). Precise update of the transit epochs also helps us accurately predict the future transit events. The space-based and the ground-based telescopes dedicated to new detection of exoplanets cannot be used for long term follow-up of those discovered planets. In this regard, the large aperture telescopes used in versatile astronomical applications are appropriate. Regular update and long term study of the transit light curves help us excavate information regarding the dynamics of the planets with transit photometry alone.

- **Transit timing variation (TTV) study:** Long term study (5-10 years) of transit light curves gives us information about the TTV of the planets. If over the years we find systematic drifts of the transit epochs from the predicted time, based on the planets' periods, then by analyzing those timing variations we can infer whether those drifts are due to the presence of other planets or other objects. Also, from the study, we can estimate the mass of the other objects causing the TTV. Gillon et al. (2016) and Gillon et al. (2017) have confirmed the presence of 7 planets around an M-dwarf TRAPPIST-1, of which, masses of 6 planets were estimated using this TTV method.

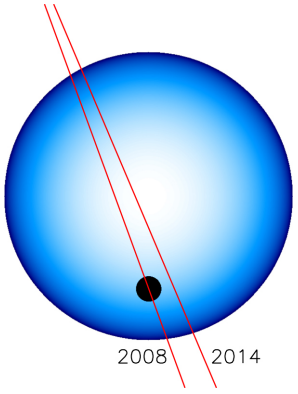

Figure 2.7: Schematic showing the transit chord crossing the star at the 2008 and 2014 epochs as shwon in Johnson et al. (2015). The stellar rotation axis is vertical, and the north pole is at the top, such that star rotates from left to right. The planet moves along the red lines from bottom to top (Johnson et al., 2015).

- **Nodal precession:** Study of the variations in the duration of the transit events of the planets over a long time (5-10 years) can reveal information about the dynamics of the orbits of the planets. For example, combining the transit photometric and radial velocity (RV) results of the planet WASP-33 b, Johnson et al. (2015) report the values of the impact parameter (b, from transit) and the spin-orbit misalignment (λ, from RV) from the observational data of 2014. Johnson et al. (2015) also compare the values of b and λ with that reported by Collier Cameron et al. (2010) (observed in 2008) and infer that the values of b and λ have changed in sync over 6 years at a rate of $db/dt = 0.0228^{+0.005}_{-0.0018}\mathrm{yr}^{-1}$ and $d\lambda/dt = 0.^{\circ}373\ \mathrm{yr}^{-1}$. This corresponds to a nodal precession of $1.^{\circ}5\ \mathrm{yr}^{-1}$ (See Figure 2.7). These changes reflect in the value of the transit duration. So, transit duration measured on two epochs ∼10 years apart using transit photometry can directly infer about the nodal precession of WASP-33 b.

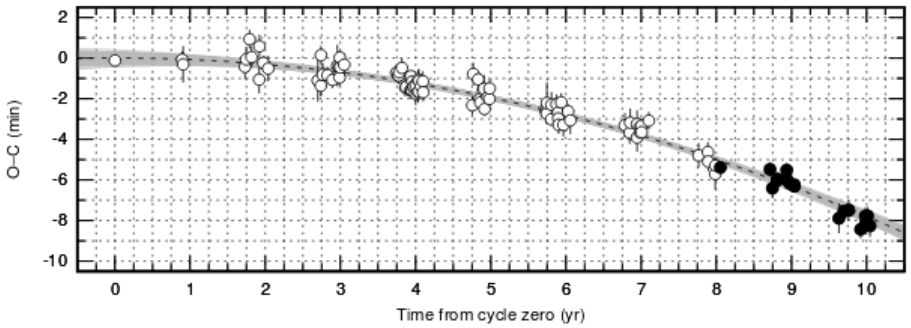

Figure 2.8: Timing residuals against the linear ephemerides for WASP-12 b as presented in Maciejewski et al. (2018). The back dashed and gray lines represnt the best-fit quadratic trend in the transit times and associated errorbar respectively. This indicates a decreasing trend in the orbital period of the planet at every epoch.

- **Orbital decay:** Study of the timing residuals can also tell us about the apsidal precession of the orbits or the orbital decay. For example, Maciejewski et al. (2016, 2018); Patra et al. (2017), etc. present that the timing residuals i.e. the deviation of the observed ephemerides from the predicted epochs of transit and the secondary eclipse of WASP-12 b show a pattern (see Figure 2.8) which can be fitted with either a quadratic

ephemeris model, assuming a circular orbit and a constant period derivative or an apsidal precession model, considering slightly eccentric orbit (Maciejewski et al., 2016, 2018; Patra et al., 2017). The former model shows a better chi-square value, when fitted with, indicating an orbital decay of WASP-12 b. The decay model implies that WASP-12 was discovered within the final ∼0.2% of its existence, which is an unlikely coincidence but harmonizes with independent evidence that the planet is nearing disruption (Patra et al., 2017). By fitting this model, the decay rate of the orbital period has been estimated to be $(-8.9 \pm 1.4) \times 10^{-10}$, $(-10.2 \pm 1.1) \times 10^{-10}$ and $(-9.67 \pm 0.73) \times 10^{-10}$ days per epoch by Maciejewski et al. (2016); Patra et al. (2017) and Maciejewski et al. (2018) respectively.

2.6.2 Procedure

We first started with the reduction of the raw transit data of TRAPPIST-1 b, which were not observed by us but by Gillon et al. (2016). The successful reduction and analysis of the data and the transit light curve (of depth ∼0.75%) obtained therefrom motivated us to follow up transit events of more planets. As hot Jupiters cause transits of relatively larger depth (1-3%), we started with the transit follow-ups of hot Jupiters. The observational techniques for follow-up observation are the same as that for the survey operations. We choose the targets according to their availability within the time-slots we are given at each telescope on each cycle by the TAC committees mentioned in Section 2.4. We observe the target host stars as long as they are available from HCT and JCBT and also, according to the transit epochs predicted in various public-accessible websites [5,6]. For our first publication we chose five hot gas giants, viz., WASP-33 b, WASP-50 b, WASP-12 b, HATS-18 b and HAT-P-36 b. The reduction,

[5] http://var2.astro.cz/ETD/predictions.php

[6] https://exoplanetarchive.ipac.caltech.edu/cgi-bin/TransitView/nph-visibletbls?dataset=transits

processing, and modeling techniques are described in the next chapter.

We have adopted the stellar parameters such as mass, radius and effective temperature of the host stars and the semi-amplitude of the oscillation of the radial velocity of the host stars due to the planets (K_{RV}) from existing data available in the literature (Bakos et al., 2012; Collier Cameron et al., 2010; Collins, Kielkopf, & Stassun, 2017; Gillon et al., 2011; Lehmann et al., 2015; Penev et al., 2016). These data combined with the transit photometric results have been used to calculate the physical properties of the planets such as mass (M_P), surface gravity (g), and equilibrium temperature for zero Bond albedo (T_{eq}).

- **TRAPPIST-1 b:** TRAPPIST-1 b is an Earth-sized planet around the host star 2MASS J23062928-0502285, an M8 type red dwarf star 12 parsecs away from the Earth (Liebert et al., 2006). The host star has a luminosity, mass and radius of 0.05%, 8% and 11.5% those of the Sun, respectively (Filippazzo et al., 2015). The host star has a magnitude of 18.8 and 14.0 in V and I filter respectively. One of the transit events of TRAPPIST-1 b was observed from HCT in I filter on 15 Nov 2015 by Gillon et al. (2016).

- **WASP-33 b:** WASP 33 b is a hot Jupiter that orbits around the host star HD 15082. We observed this object for 5 transit events - one from HCT in V filter on 09 Dec 2017, two from JCBT in I filter on 05 Jan 2018, 27 Jan 2018 and the other two from JCBT in V filter on 26 Dec 2018 and 06 Jan 2019. The host star is an A5 type star (Grenier et al., 1999). It has a mass of 1.495 ± 0.031 $M_\odot$ and a radius of 1.444 ± 0.034 $R_\odot$ (Collier Cameron et al., 2010). It is a δ Sct variable star with a V mag of 8.3 (Herrero et al., 2011). So, the transit light curves of WASP-33b are contaminated with the pulsations as reported by Johnson et al. (2015); von Essen et al. (2014). The effect of these pulsations on the estimation of the transit parameters is subtracted by adopting a denoising technique

as explained in Section 3.4.2. The orbital period of the planet is taken as 1.21987 ± 0.000001 days (Collier Cameron et al., 2010; Johnson et al., 2015; von Essen et al., 2014).

In order to determine the mass and hence the mean density of the planet, we have considered the semi-amplitude of the radial velocity of the star due to the planet as $K_{RV} = 304.0 \pm 20.0 \mathrm{ms}^{-1}$ (Lehmann et al., 2015). The effective temperature of the host star is taken to be $T_{eff} = 7308 \pm 71$ K (Collier Cameron et al., 2010). From this the equilibrium temperature of the planet is determined (see section 3.10).

- **WASP-50 b:** We observed a total of 5 transit events of this hot Jupiter by using JCBT in I filter on 26 Jan 2018, 28 Jan 2018 and 30 Jan 2018 and in R filter on 07 Jan 2019 and 11 Jan 2019. The host star has a V mag of 11.44, a mass of $0.892^{+0.080}_{-0.074}$ $M_{\odot}$ and a radius of 0.843 ± 0.031 $R_{\odot}$ (Gillon et al., 2011). The T_{eff} and the semi-amplitude of the radial velocity of the star due to the planet (K_{RV}) are respectively 5400±100 K and 256.6±4.4 m/s (Gillon et al., 2011). The orbital period of the planet is taken as1.955100 ± 0.000005 days (Gillon et al., 2011).

Table 2.2: Stellar and orbital parameters adopted from literature

Parameters	WASP-33 b	WASP-50 b	WASP-12 b	HATS-18 b	HAT-P-36 b
Host star mass, M_* ($M_{\odot}$)	1.495 ± 0.031	$0.892^{+0.08}_{-0.074}$	1.434 ± 0.11	1.037 ± 0.047	1.03 ± 0.03
Host star radius, R_* ($R_{\odot}$)	1.444 ± 0.034	0.843 ± 0.031	1.657 ± 0.046	$1.02^{+0.057}_{-0.031}$	1.041 ± 0.013
Host star T_{eff} (K)	7430 ± 100 (a)	5400 ± 100	6360 ± 140	5600 ± 120	5620 ± 40
Orbital Period, P (days)	1.21987 ±0.000001	1.955100 ±0.000005	1.09142 $\pm 1.4432 \times 10^{-7}$	0.83784 $\pm 4.7 \times 10^{-7}$	1.32734683 ±0.00000048
RV amplitude, K_{RV} (m/s)	304 ± 20	256.6 ± 4.4	226.4 ± 4.1	415.210.0	334.7 ± 14.5

Note. The value of each parameter is shown along with 1σ error margin. The parameters are taken from Collier Cameron et al. (2010) and Lehmann et al. (2015) for WASP-33 b; from Gillon et al. (2011) for WASP-50 b; from Collins, Kielkopf, & Stassun (2017) for WASP-12 b; from Penev et al. (2016) for HATS-18 b; from Bakos et al. (2012) and Mancini et al. (2015) for HAT-P-36 b.

- **WASP-12 b:** Using JCBT, we observed the transit events for this hot Jupiter on 14 Feb 2018 in R-band, on 15 Feb 2018 in I-band and on 04 Jan

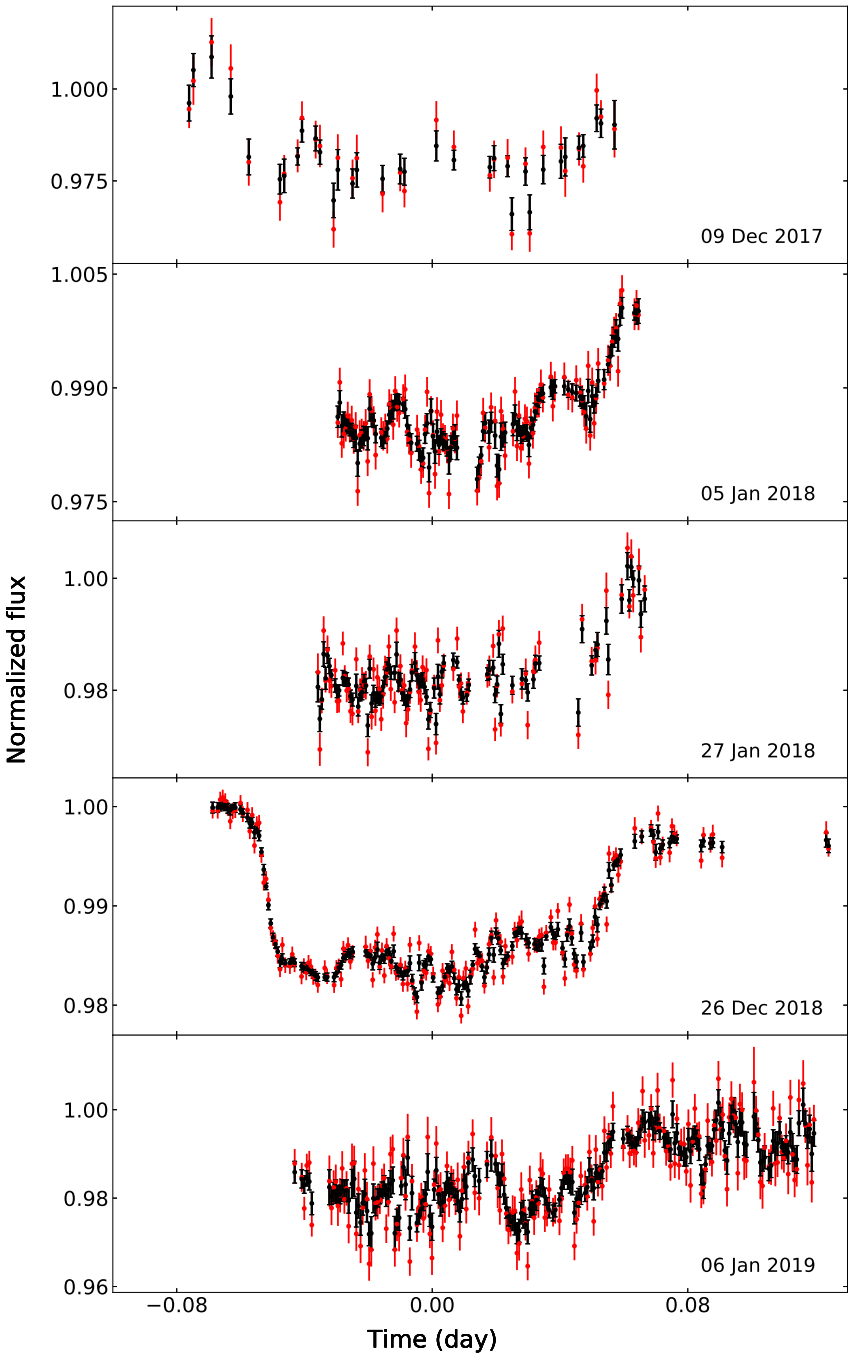

Figure 2.9: The transit light curves of WASP-33b. The original light curves (right after differential photometry) are shown with red errorbars and wavelet denoised light curves are over-plotted with black errorbars. The zero points on the time axes are set at the the mid-transit ephemerides as shown in Table 3.1.

2019 in V-band. The host star has a mass, radius and T_{eff} of 1.434 ±0.11 $M_{\odot}$, 1.657 ±0.046 $R_{\odot}$ and 6300 ±150 K respectively (Collins, Kielkopf,

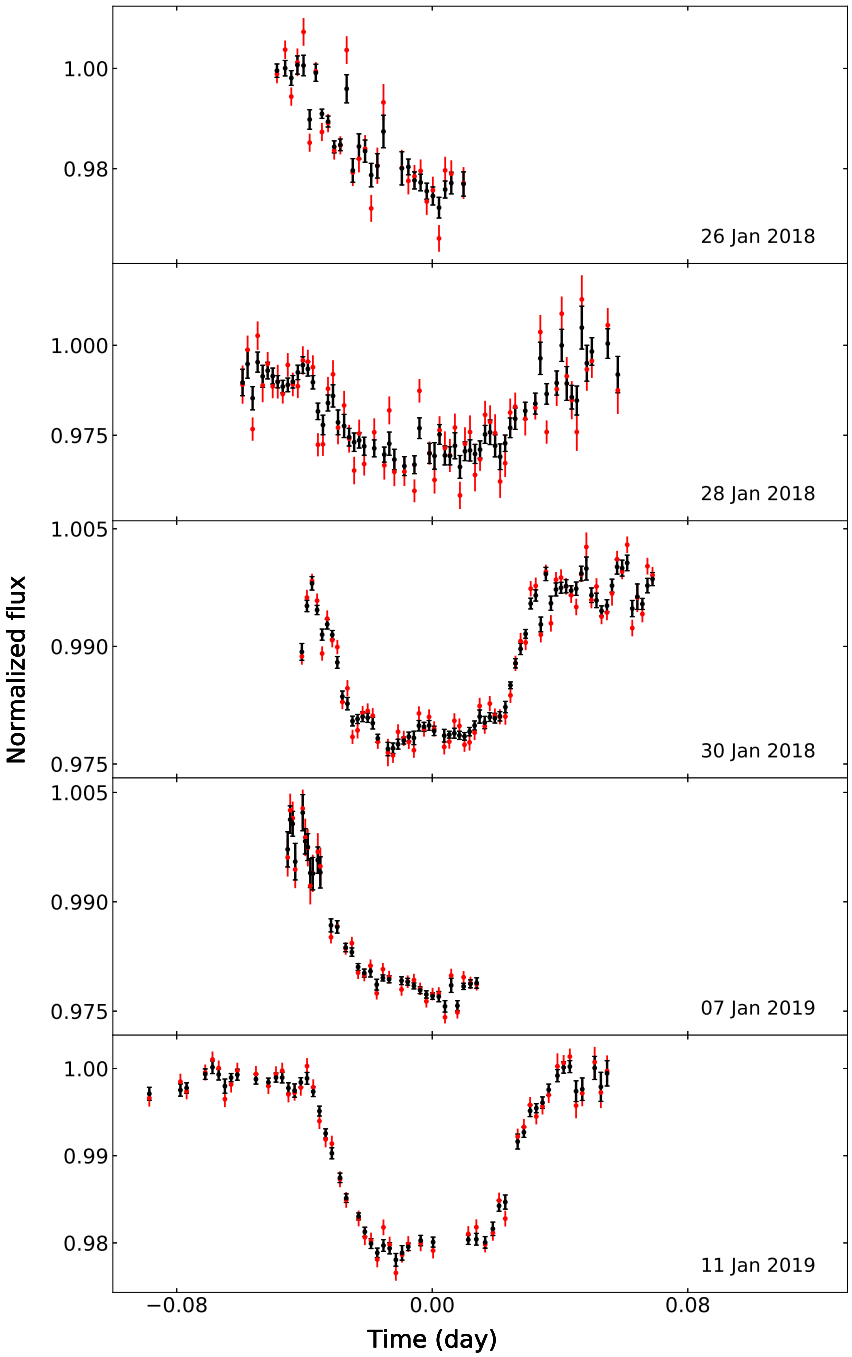

Figure 2.10: The transit light curves of WASP-50b. The original light curves (right after differential photometry) are shown with red errorbars and wavelet denoised light curves are over-plotted with black errorbars. The zero points on the time axes are set at the the mid-transit ephemerides as shown in Table 3.1.

& Stassun, 2017). The semi-amplitude of the radial velocity of the star due to the planet is $K_{RV} = 226 \pm 4.0 \mathrm{ms}^{-1}$ (Collins, Kielkopf, & Stassun,

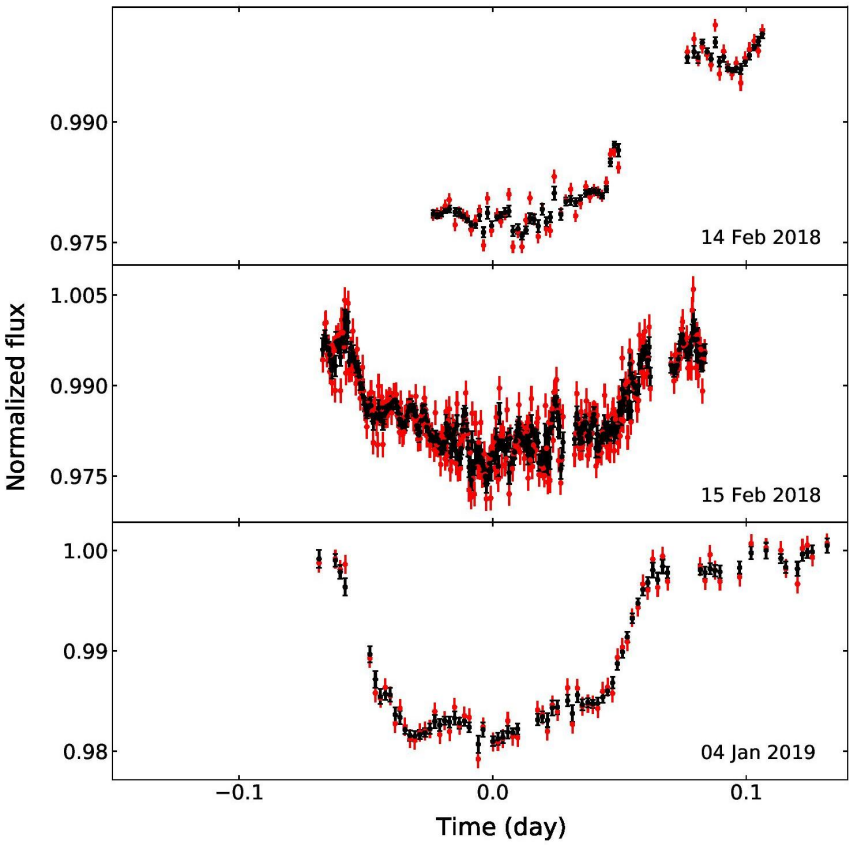

Figure 2.11: The transit light curves of WASP-12b. The original light curves (right after differential photometry) are shown with red errorbars and wavelet denoised light curves are over-plotted with black errorbars. The zero points on the time axes are set at the the mid-transit ephemerides as shown in Table 3.1.

2017). The orbital period of the planet is 1.09142 ± 0.00000014 days (Collins, Kielkopf, & Stassun, 2017).

- **HATS-18 b:** HATS-18 b is a hot Jupiter that orbits around a G type star which is very similar to the Sun in terms of mass, radius and T_{eff}. We report the observations of four transit events of HATS-18 b, all by using JCBT. The observations were taken in I-band on 27 Jan 2018, 18 Feb 2018 and 06 Apr 2018 and in R-band on 08 Jan 2019. The host star has a mass, radius and T_{eff} of 1.037 ±0.047 $M_{\odot}$, $1.020^{+0.057}_{-0.031} R_{\odot}$ and 5600 ±120 K respectively (Penev et al., 2016). The semi-amplitude of radial velocity of the star is $K_{RV} = 415.2 \pm 10.0 \mathrm{ms}^{-1}$ (Penev et al., 2016). The orbital period of the planet is 0.8378 ± 0.00000047 days (Penev et al.,

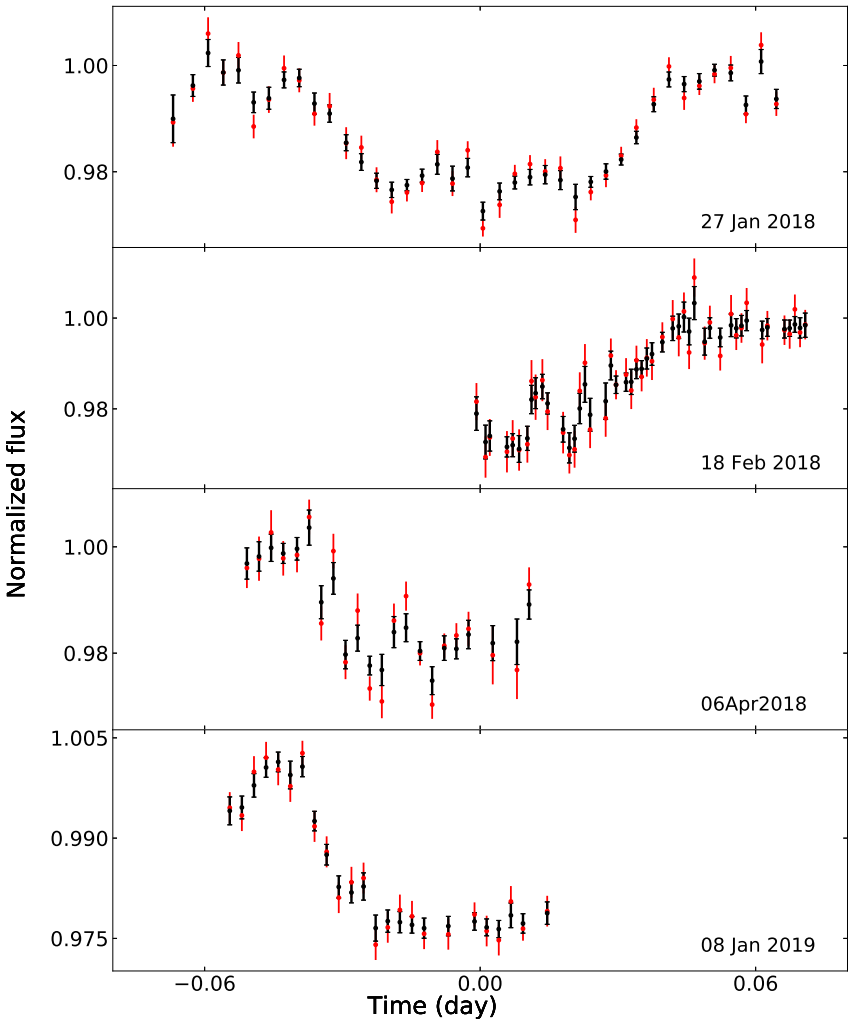

Figure 2.12: The transit light curves of HATS-18b. The original light curves (right after differential photometry) are shown with red errorbars and wavelet denoised light curves are over-plotted with black errorbars. The zero points on the time axes are set at the the mid-transit ephemerides as shown in Table 3.1.

2016).

- **HAT-P-36 b:** We observed HAT-P-36b during 4 transit events: On 15 Feb 2018 by using I filter, on 08 Apr 2018 and 06 May 2018 by using V filter in JCBT and on 20 Jun 2018 by using V filter in HCT. The host star is a G5V star with mass, radius and T_{eff} of 1.03 ± 0.03 $M_{\odot}$, 1.041 ± 0.013 $R_{\odot}$ and 5620 ± 40 K respectively (Bakos et al., 2012). This star is also very similar to the Sun in terms of mass, radius and T_{eff}. The semi-amplitude of radial velocity of the star due to the planet is $K_{RV} =$

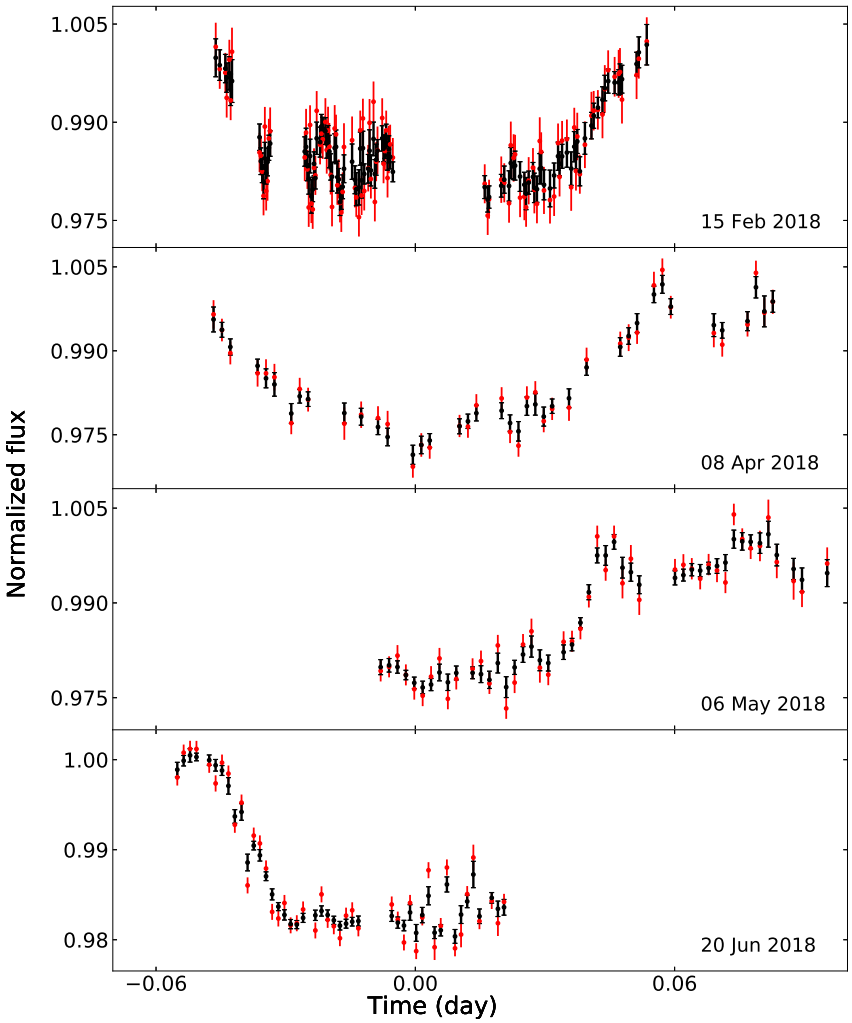

Figure 2.13: The transit light curves of HAT-P-36b. The original light curves (right after differential photometry) are shown with red errorbars and wavelet denoised light curves are over-plotted with black errorbars. The zero points on the time axes are set at the the mid-transit ephemerides as shown in Table 3.1.

$334.7 \pm 14.5 \mathrm{ms}^{-1}$ (Bakos et al., 2012; Mancini et al., 2015). The orbital period of the planet is taken as 1.9551 ± 0.00005 days (Bakos et al., 2012; Mancini et al., 2015).

2.6.3 Results and Discussion

The transit light curve of TRAPPIST-1 b is found to be stable and the transit depth of 0.75% is detected at $\sim 4\ \sigma$ significance as evident from Figure 2.3. The light curves of the hot Jupiters often contain white noise fluctuations added

Table 2.3: Deatils of observation

Planet	Date of Observation	Telescope	Filter (Bessel)	Photometric SNR (median)	Cycle no.[a]
WASP-33 b	09 Dec 2017	HCT	V	191.90	4191
	05 Jan 2018	JCBT	I	1253.47	4213
	27 Jan 2018	JCBT	I	300.29	4231
	26 Dec 2019	JCBT	V	505.03	4504
	06 Jan 2019	JCBT	V	466.48	4513
WASP-50 b	26 Jan 2018	JCBT	I	361.93	1323
	28 Jan 2018	JCBT	I	252.39	1324
	30 Jan 2018	JCBT	I	1012.89	1325
	07 Jan 2019	JCBT	R	1139.06	1500
	11 Jan 2019	JCBT	R	1086.67	1502
WASP-12 b	14 Feb 2018	JCBT	R	1261.32	2764
	15 Feb 2018	JCBT	I	500.50	2765
	04 Jan 2019	JCBT	V	1085.84	3646
HATS-18 b	27 Jan 2018	JCBT	I	443.07	1261
	18 Feb 2018	JCBT	I	239.80	1287
	06 Apr 2018	JCBT	I	307.09	1343
	08 Jan 2019	JCBT	R	425.84	1674
HAT-P-36 b	15 Feb 2017	JCBT	I	329.09	1959
	08 Apr 2018	JCBT	V	461.99	1998
	06 May 2018	JCBT	V	589.10	2019
	20 Jun 2018	HCT	V	1106.84	2053

[a]The mid-transit ephemerides (BJD-TDB) at cycle 0 for WASP-33 b, WASP-50 b, WASP-12 b, HATS-18 b, HAT-P-36 b are considered to be at 2452984.82964 (Turner et al., 2016), 2455558.61197 (Gillon et al., 2011), 2455147.4582 (Turner et al., 2016), 2457089.90598 (Penev et al., 2016) and 2455565.18167 (Mancini et al., 2015) respectively.
[†]The raw frames observed on these dates were kindly given to us by Vineet Mannaday and Dr. Parijat Thakur and we reduced and analyzed the data to get the light curves.

with the red noise. The different noise with different origins are treated differently as elaborated in Section 3.5-3.8. The light curves were pre-processed with wavelet denoising technique (elaborated in Section 3.6 and 3.8) before modeling in order to reduce the white noise and improve the precision in the deduced results. Figure 2.9-2.13 show the transit light curves of those planets observed on different nights. The errorbars in red denote the light curves obtained directly after the differential photometry and the black errorbars denote the wavelet denoised light curves. The detailed results after modeling are described in the next chapter.

2.7 Caveats and Circumventions

In general, the transit photometric method has many caveats that render this method difficult to be used for the detection of the planets without proper preparation and arrangements. Post-processing tools are crucial for the precise study of the planetary properties associated with transit events. These caveats and the possible ways of circumventing them are explained below.

- **Low transit probability:** A transit event cannot be observed unless aligned from the observer's vantage point. The probability for a randomly-oriented planet on a circular orbit to be favorably aligned for transit, or secondary eclipse, is $p = R_*/a$, where, R_* and a are the stellar radii and orbital separation respectively. So, for a large orbital separation, the probability of detection is extremely low.

  To circumvent that, the target population is generally kept extremely high. A large field of view on-sky with a crowded field of stars are monitored continuously either from a space-based telescope or from a co-ordinated group of ground-based telescopes to increase the chance of detection.

- **High rate of false detection:** Low depths of transit light curves make the method susceptible to a high number of false detections. Stellar activity (passage of a star-spot rather than a planet), flares etc. get identified as transit signal by mistake frequently.

  Stellar activities can be ruled out from transit detection by observing a target star for a long time and looking for the strictly periodic events, as activities are not as periodic as planetary transits (mostly spots die after some interval). However, to rule out all other possibilities the host stars are thoroughly studied using photometry and spectroscopy and the probability of the detected signal being a false alarm is calculated. If the probability of the true positive crosses the threshold (usually 99%) then

the detection is accepted. Also, rigorous modeling with detrending and denoising techniques is extremely important to rule out stellar variability and pulsation. Nonetheless, the estimates of the radii of the planets and the other transit parameters obtained from modeling the transit light curves can be used to assess the plausibility of the transit events. Moreover, masses of the planets estimated using the other techniques, such as RV, TTV, etc., complement the information about the planets obtained from the transit photometric observations and confirm their presence.

- **Susceptable to systematics and noise:** As the transit depths are extremely small, e.g. 1-3% for hot Jupiters and several ppm for Earth-sized or Mercury-sized planets around solar-type stars, the transit signals are easily contaminated with external systematics and noise. In the case of space-based observation, the transit light curves are susceptible to systematics from various sources such as attitude fluctuation of the space vehicles, Exposure of detectors to cosmic rays, charged particles or solar flare etc. On the other hand, in the case of ground-based observation, fluctuations in the atmospheric transparency, drifts in telescope tracking, fluctuations in ambient temperature and humidity of the detectors etc. can add significant systematics and white noise to the transit signals. In addition to that, long term stellar variabilities and short term stellar pulsations can add red noise to the transit signals.

  The noises from different sources are treated differently using techniques like baseline detrending, differential photometry, wavelet denoising, Gaussian process regression etc. which are explained elaborately in Chapter 3.

Chapter 3

Analysis and Modeling of Transit Photometric Data[1]

3.1 Introduction

The observed raw data contain frames of images of the fields on-sky under study. The first step of the analysis involves the reduction of these frames followed by some processing. To handle the bulk amount of data efficiently we have developed an automated pipeline that performs the necessary tasks on the raw frames and produces the light curves. The second step involves the processing of the light curves containing the transit signals to address the different sources of noise that pollute and distort the transit light curves. The last step involves modeling of the transit light curves efficiently to estimate the planet properties with high precision.

In the following subsections, we briefly describe the pipelines we have developed for reduction and analysis and also the modeling pipeline. We analyze the different sources of noise contaminating the transit light curves and address them with different denoising techniques.

[1] *Part of this chapter is published in The Astronomical Journal, Chakrabarty and Sengupta, vol. 158:39, 2019.*

3.2 Reduction and Analysis of Raw Data Using Pipeline Developed by Us - 'Pyapphot'

The reduction of raw data involves processes like bias subtraction, flat fielding, alignment of the frames, discarding of bad frames, selection of objects on the frames, aperture selection and performing differential photometry. Performing these tasks on the huge amount of data manually is extremely cumbersome and prone to manual error. To avoid this, we have developed a Python-based pipeline, namely `pyapphot`, that can be publicly found on Github [2]. The key features of this package are as follows.

- This package allows interactive selection and deselection of objects on the frames.
- This package also performs auto-detection of objects on multiple frames based on one reference frame, auto-alignment of the frames, etc.
- Using this package one can extract all the information about the point spread functions (PSFs) on the frames and store them for future use.
- This package also allows users to set their criteria to filter out the frames or objects with poor PSF and helps make a decision regarding the trade-off between the frames to be discarded and the objects to be discarded.
- It allows users to perform differential photometry and calculate the differential flux (or mag) as a function of time with a proper estimation of the propagated error and save the results in datacubes.

After reducing with `pyapphot` we get the light curves for different targets and choose them where we can find a transit dip of depth >0.5%.

[2] https://github.com/arcunique/pyapphot

3.3 Modeling of Transit Light Curves Using Pipeline Developed by Us - 'MATTrEx'

We model the transit light curves by using the formalisms described in Mandel & Agol (2002). Using this formalism the flux from the host star during a transit event can be expressed as a function of the projected distance between the centers of the stellar disc and the planetary disc and hence, as a function of time normalized to the orbital period (P). This formalism also allows us to include the effect of stellar limb darkening. We have used the Markov Chain Monte Carlo (MCMC) technique employing the Metropolis-Hastings algorithm (Collier Cameron et al., 2010) to fit the models with the observed light curves and thus determined the various physical parameters from the best fit. An essential parameter of the model is the orbital period which we have kept fixed at the values given in previously published results (Bakos et al., 2012; Collier Cameron et al., 2010; Collins, Kielkopf, & Stassun, 2017; Gillon et al., 2011; Penev et al., 2016). For all the transit events we have assumed circular orbits of the planets. The free parameters for each transit model are the mid-transit ephemeris (t_{cen}), the impact parameter (b), the scaled radius of the star (R_*/a), the ratio between the planetary and the stellar radius (R_p/R_*), the pre-ingress or post-egress baseline level of the observed flux (f_{star}) and the limb darkening coefficients (Ci). The principle of MCMC is explained below.

The main target of MCMC is to find the parameters corresponding to the maximum likelihood of the parameters given the observed data i.e. the conditional probability $p(\Theta|t, f, \sigma)$, where t, f and σ denote time, flux and the error in flux respectively. Θ denote the set of parameters. By Bayes' theorem,

$$\begin{aligned} p(\Theta|t, f, \sigma) &\propto p(\Theta)p(f|\Theta, t, \sigma) \\ Or,\ \ \ln p(\Theta|t, f, \sigma) &= \ln p(\Theta) + \ln p(f|\Theta, t, \sigma) + constant \end{aligned} \tag{3.1}$$

The probability $p(\Theta)$ is called the prior function which is assumed to be a

Gaussian or a uniform function. The natural logarithm (ln) of $p(f|\Theta, t, \sigma)$ can be expressed as,

$$\ln p(f|\Theta, t, \sigma) = -0.5 \sum_i \left[\frac{(f_i - m_i)^2}{\sigma_i^2} + \ln(2\pi\sigma_i^2) \right], \tag{3.2}$$

where m_i denotes the transit model as a function of the parameters Θ and t. Clearly, by maximizing Equation 3.2 we determine the sample space of the best-fit parameters.

We have modeled all the observed transit light curves of a particular planet simultaneously. By modeling the light curves simultaneously we have deduced a single set of values for b, R_*/a and R_p/R_* for each planet. These parameters are the properties of the planet-star systems and hence independent of the observing conditions. We deduced different sets of values for the limb darkening coefficients C_i for each host star for different filters. Also, for different transit events, we deduced different sets of values for t_{cen} and f_{star} from our model fit (Table-3.1) as these parameters depend on the nights of observations. For all the free parameters we have set uniform prior function (Gillon et al., 2011). We adopted quadratic limb darkening law which can be expressed as:

$$I/I(\mu = 1) = 1 - C_1(1 - \mu) - C_2(1 - \mu^2), \tag{3.3}$$

where $I/I(\mu = 1)$ denotes the intensity at any point on the disc normalized to that at the center. The initial values required to derive the limb darkening coefficients from the MCMC fit are taken from Claret & Bloemen (2011) and Gaussian priors were set on them (Johnson et al., 2015).

The MCMC generates a sample space of the best-fit values for the model parameters depending upon the number of walkers and iterations by maximizing the likelihood space of model fits to the light curve data. A Gaussian fit to the sample space then gives the required value of the parameters at 1σ error margins. We have developed a modeling pipeline (not made public yet) that

handles multiple transit light curves, segregates the free and fixed parameters and generates the distributions of best-fitted parameters employing MCMC.

3.4 Different Sources of Noise

The images captured from ground-based telescopes are susceptible to noises generated from various sources. These noises are either common to all the objects in a frame and uncorrelated in time such as the noises caused by the fluctuations in the transparency, seeing, airmass etc. or unique to each object and correlated in time such as the noises caused by the activity or pulsations of the host stars. In order to reduce the former kind of noises from the light curves, a preprocessing on the light curves is essential before modeling to achieve high precision in the transit parameters estimated from modeling. Whereas, the correlated noises can only be modeled and then subtracted from the original light curves.

3.4.1 Noise on Each Frame

These sources of noise contaminate each frame of observation. These include photon noise from the source itself, sky and background noise, dark and read-out noise, etc. Photon noise majorly contributes to the errorbars in the light curves constricting the precision in the parameters obtained by modeling these light curves. Owing to the large apertures of the telescopes we use (JCBT and HCT), we can observe transit events of faint host stars (V-band mag $\sim$15) and detect a transit event with a high confidence level with respect to the photon noise, even from a single set of observation. The photon signal-to-noise ratio (SNR) can be increased by increasing the exposure time within the saturation limit and also by acquiring multiple transit observations of the same planet-star pair. Sky noise does not dominate over the source photon noise unless the observations are taken on bright illuminated nights, e.g., a full moon night. Dark noise and read-out noise can be ignored as we capture the images with

the high-end CCDs housed at the back-end of the telescopes which are cooled with liquid nitrogen.

3.4.2 Noise Accumulated over Time: Fluctuations in Light Curves

A major source of noise is the varying atmospheric extinction which changes with the change in elevation of the source on-sky throughout the observation. To reduce this kind of large-scale noise, we perform differential photometry of the host stars. In this method, we perform aperture photometry of several other stars in the field of view, known as the field stars, along with the target stars. Then the differential flux (or magnitude) is calculated for every pair of field stars. One of the stars showing the least fluctuation in the differential flux over time is selected as a reference star for the target star. Finally, the differential flux (or magnitude) is calculated between the target and the reference stars.

Another source of noise is the scintillation or the change in transparency in the Earth's atmosphere. This causes medium- to small-scale fluctuations in the light curves. Usually, this kind of noise is uncorrelated in time. Also, irregular cosmic rays can hit and contaminate some of the pixels on the frame. These cause some outliers in the light curves.

In addition to these patterns, confusing signals caused by stellar activity or pulsation are unique to each star. They are temporally correlated and can not be suppressed or removed by de-noising. They can, however, be modeled alongside the signal of interest. The effect of the high-frequency variation or pulsation of stellar flux can be traceable within a transit event. This kind of noise requires special decorrelation techniques for reduction. Besides, low-frequency variations can also be present on the light curves affecting the baselines (causing, for example, tilt in the baselines) of the light curves when observed for a long time covering multiple transit events. These gradual trends originate from various sources such as low-frequency variations in host star flux, the

effect from other astrophysical sources, the drift of the telescope, or attitude problem in space vehicles in case of space-based observation, etc. These trends can be detrended in various techniques one of which is discussed in the next section.

3.5 Segregation and Treatment of Noise

Overall, the different noises can be broadly categorized into three kinds in terms of treatment (Chakrabarty & Sengupta, 2019). The first kind is the noise due to large-scale transparency fluctuations (due to scintillation or varying airmass etc.) that change the apparent brightness of all the stars in the frame almost equally. This kind of noise can be taken care of by using techniques like differential photometry. The second kind is the patterns caused by the medium- to small-scale transparency fluctuations or seeing fluctuations that affect the stars on a frame slightly unequally but temporally uncorrelated. In order to reduce the effect of such kind of noise, a preprocessing on the light curves is essential before modeling to achieve high precision in the transit parameters estimated from modeling. However, the smoothing techniques such as Moving Average or Gaussian smoothing can not be used to suppress these noises as the smoothing process can distort the original light curves by removing the high-frequency components of the transit signal itself and question the reliability of the properties derived therefrom.

On the other hand, for a non-stationary non-sinusoidal signal like a noisy transit signal, the wavelet denoising is much more efficient than a frequency-based filtering technique in terms of signal reconstruction and denoised SNR (Barsanti & Gilmore, 2011; Lagha et al., 2013). Wavelets have already been used extensively in the light curve noise analysis and filtering (Cubillos et al., 2017; Waldmann, 2014). Also, this method removes the outliers caused by the cosmic-ray hits etc. The concept of wavelets and wavelet denoising is explained in Section 3.6.

In addition to these white sources of noise, the light curves are also affected by red noise, which is the third kind of noise. These appear either due to small scale fluctuations that affect the different stars on the frames differently or because of some events unique to the host star itself. In either case, the noise is correlated in time which calls for modeling of the noise for reduction. The long term systematics can be reduced by detrending the light curves. Detrending is performed by, first, modeling the baseline assuming a polynomial relationship between the baseline flux and the independent variables such as time, position on CCD, focus, etc.; followed by which, the light curve is divided by that baseline model to make the baseline flat (Gillon et al., 2016). However, the choices of the independent variables and the degree of the polynomial are determined by minimizing the Bayesian Inference Criteria (BIC) (Gillon et al., 2016). In our case by minimizing the BIC, we have chosen a one order baseline function of time. On the other hand, the high-frequency fluctuations caused by the host star activity or pulsation can be addressed by applying Gaussian process regression (see Section 3.7).

3.6 Wavelets, Wavelet Transform and Wavelet Denoising

A wavelet is a wave-like but finite oscillation with a varying amplitude that increases from zero and then goes back to zero. These highly localized impulse-like functions can be used to extract information in both the domains of time and frequency for non-stationary signals. For practical purposes, a wavelet function is preferred to be continuously differentiable, but a prototype wavelet function has to be square-integrable in the time domain i.e.

$$\int_{-\infty}^{\infty} |\psi(t)|dt < \infty \; and \; \int_{-\infty}^{\infty} |\psi(t)|^2 dt < \infty, \tag{3.4}$$

The prototype function $\psi(t)$ is also known as the mother wavelet. A mother

wavelet is scaled and shifted and then projected on to the signal under study to excavate the time-frequency information. This altered child wavelet can be expressed as,

$$\psi_{a,b}(t) = \frac{1}{\sqrt{a}}\psi\left(\frac{t-b}{a}\right), \tag{3.5}$$

where a is a positive number denoting the scale and b is a real number denoting the delay. In discrete space the real space of parameters (a, b) is mapped into positive integer space of parameters (m, n) and the child wavelet is expressed as,

$$\psi_{m,n}(t) = \frac{1}{\sqrt{a^m}}\psi\left(\frac{t-nb}{a^m}\right), \tag{3.6}$$

where $a > 1$ and $b > 0$ are fixed at some values. The discrete wavelet transform is obtained by projecting the child wavelet on to the signal under study, say x(t), and as a result we get discrete coeffcients.

$$c_{m,n} =< x, psi_{m,n} >= \int x(t)\psi_{m,n}(t)dt \tag{3.7}$$

The signal x(t) can be reconstructed as ,

$$x(t) = \sum_{m\in\mathbb{Z}}\sum_{n\in\mathbb{Z}} < x, \psi_{m,n} > .\psi_{m,n}(t) \tag{3.8}$$

However, in discrete wavelet transform (DWT) that admits to a multiresolution anaysis (Mallat, 1989), to avoid the numerical complexity in calculating the coefficients, the wavelet consists of a mother wavelet function $\psi_{m,n}$ and an auxiliary function $\phi_{m,n}$, also known as a father wavelet or scaling function. In such a case the reconstructed signal X is expressed as,

$$X = \sum_n c_{m0,n}\phi_{m0,n} + \sum_{m<m0}\sum_n d_{m,n}\psi_{m,n}, \tag{3.9}$$

where the coefficents are given by,

$$c_{m0,n} = \ < X, \phi_{m0,n} > \ \text{and} \ \ d_{m,n} = \ < X, \psi_{m,n} > \tag{3.10}$$

Some of the wavelet and scaling functions for different wavelet families are shown in Figure 3.1.

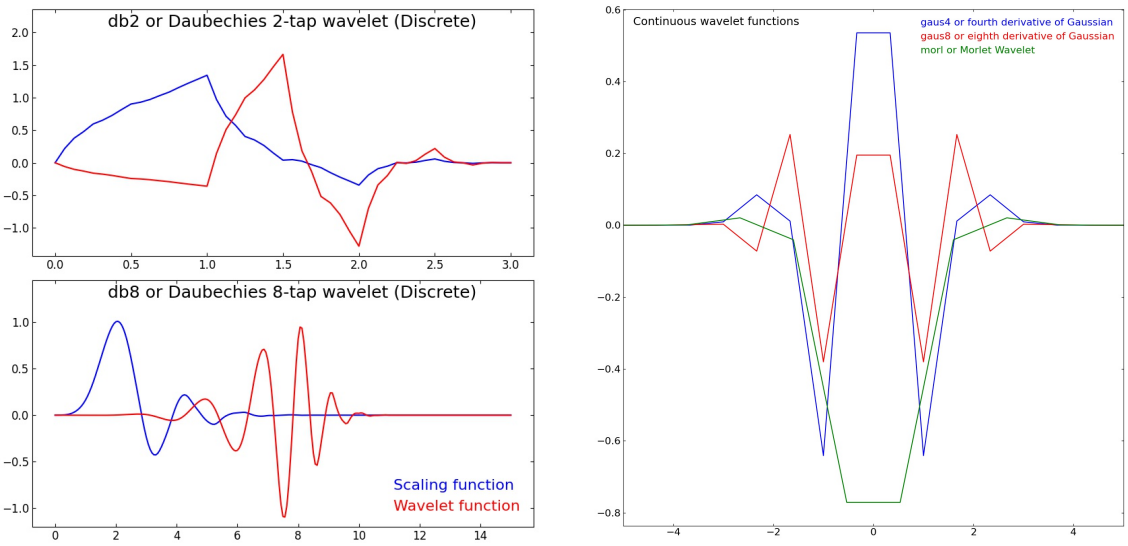

Figure 3.1: Left: The scaling and wavelet functions of the two discrete wavelets from Daubechies family, viz., db2 (2-tap) and db8 (8-tap). Right: The wavelet functions of the continuous wavelets, viz., gaus4 (fourth derivative of Gaussian), gaus8 (eighth derivative of Gaussian) and morl (morlet wavelet).

In wavelet denoising, a signal is first decomposed into approximate and detail coefficients as explained in del Ser, Fors, & Núñez (2018). The number of decomposition levels is equal to the length of the $\log_2$ of the signal length. The decomposition is done using stationary wavelet transform (SWT) instead of DWT which is similar to DWT except SWT overcomes the lack of translation-invariance of the DWT. One way of denoising is thresholding the last level detail coefficients at a cut-off level while reconstructing the signal. Another way is to first calculate the inverse SWT (ISWT) at each level by setting all the coefficients other than those of that level to zero and then the last level ISWTs are thresholded to reconstruct the signal by filtering the low amplitude noise out. The coefficients after SWT of a simulated transit light curve and the decomposed signal obtained from ISWT of those coefficients at each level

are shown in Figure 3.2.

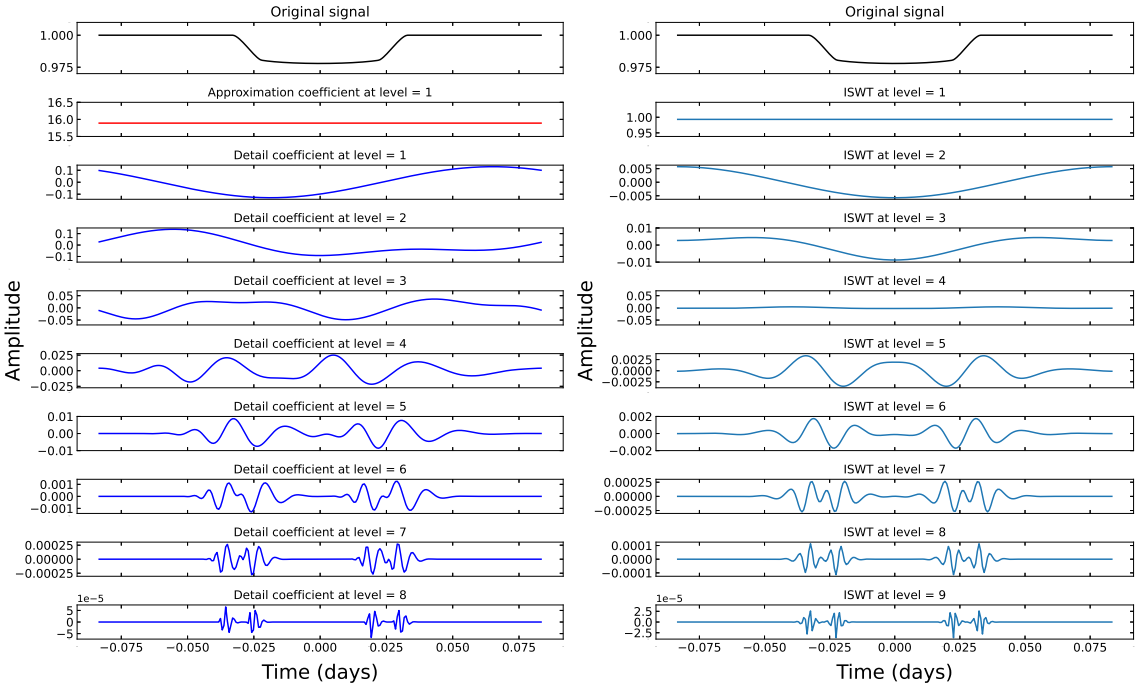

Figure 3.2: Left: The approximation and detail coefficients obtained from the stationary wavelet transform (SWT) of a simulated transit light curve. Right: The inverse SWT performed on the SWT coefficients of the light curve at each level as explained in Section 3.6 (also, see del Ser, Fors, & Núñez (2018)).

3.7 Gaussian Process (GP) Regression

Gaussian process (GP) regression, also known as correlation noise modeling, is applied to model the correlated noise added with the signal that can not be reduced by denoising techniques. A full description of GP regerssion can be found in Rasmussen & Williams (2006). Contrary to white noise, in case of red noise, we use the covariance matrix rather than just the noise vector. The covariance matrix (K) can be expressed as,

$$K_{ij} = \sigma_i^2 \delta_{ij} + k(t_i, t_j), \tag{3.11}$$

where δ_{ij} is the Kronecker delta function and k is the covariance function which is user-definable. Following Barclay et al. (2015); Rasmussen & Williams

(2006), etc., we use the Matérn-3/2 function for k given by,

$$k_{ij} = \alpha^2 \left(1 + \frac{\sqrt{3}|t_i - t_j|}{\tau}\right) \exp\left(-\frac{\sqrt{3}|t_i - t_j|}{\tau}\right), \tag{3.12}$$

where α and τ are two free parameters of the regression.

Accordingly, Equation 3.2 can be written as,

$$\ln p(f|\Theta, t, \sigma) = -0.5(y-m)^T K^{-1}(y-m) - 0.5 \ln \det K - \frac{N}{2} \ln(2\pi), \tag{3.13}$$

where N denotes the total number of data points. As evident from the above equations, the regression requires a mean model which in this case is the transit model itself.

3.8 wavelet Denoising and GP Regression on Transit Light Curves

In the case of transit photometry, wavelet denoising can efficiently remove the outliers, yield better MCMC posterior distributions and reduce the bias in the fitted transit parameters and their uncertainties (del Ser, Fors, & Núñez, 2018). We used the pywt package (Lee et al., 2018) and followed the same procedure as described in del Ser, Fors, & Núñez (2018). Also, we simulated a transit light curve assuming a set of values for the transit parameters along with uncertainties in each parameter. The uncertainties in the parameters then reflect the errorbars in the simulated transit light curve. The wavelet denoising process is expected not to affect a light curve with errorbars limited by the uncertainty in the transit parameters. In fact, we found that our simulated transit light curve was almost unchanged by the denoising process. This ensures that the light curves are not over-smoothed or the errorbars are not under-estimated by the denoising process.

The transit light curves with and without wavelet-denoising are shown in

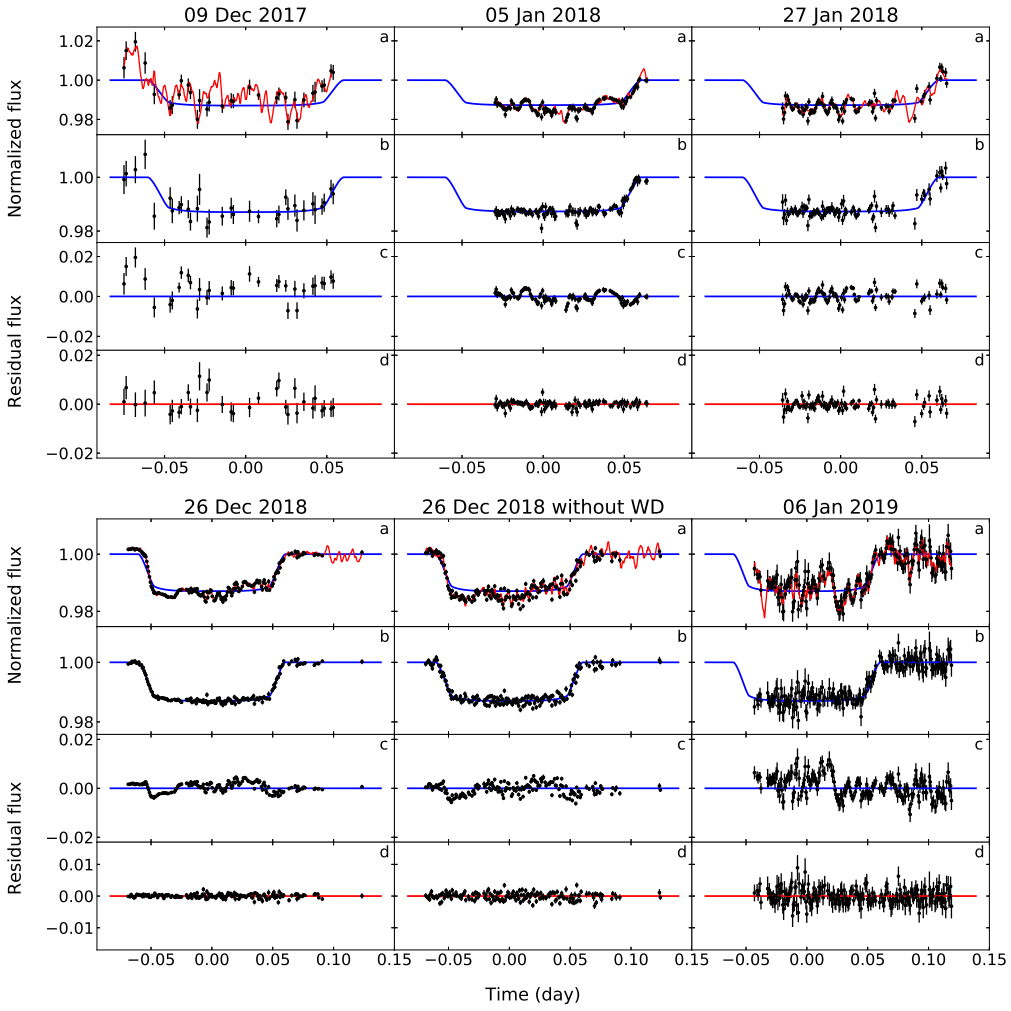

Figure 3.3: The normalized light curves, with and without the wavelet denoising process and the model fits for WASP-33b. The zero points on the time axes are set at the mid-transit ephemerides as shown in Table 3.1.
a - The black errorbars represent the normalized wavelet-denoised flux with associated error. On top of it the MCMC-fitted transit models with and without Gaussian process correlated noise (GP) models are shown with red and blue lines respectively. b - The black error-bars represent the normalized wavelet-denoised data minus the GP noise model. On top of it the MCMC-fitted transit models (without GP) are shown in blue lines. c - The black error-bars represent the residual flux with error after subtracting only the transit models (without GP). d - The black errorbars represent the residual flux plus error after subtracting both the transit model and the GP noise model.

Figure 2.9, Figure 2.10, Figure 2.11, Figure 2.12 and in Figure 2.13. The values of the planetary physical parameters deduced by modeling the transit light curves preprocessed with wavelet denoising are presented in Table 3.2. The same without wavelet denoising process are provided in Table 3.3. A comparison of the results presented in the two tables implies that the wavelet denoising

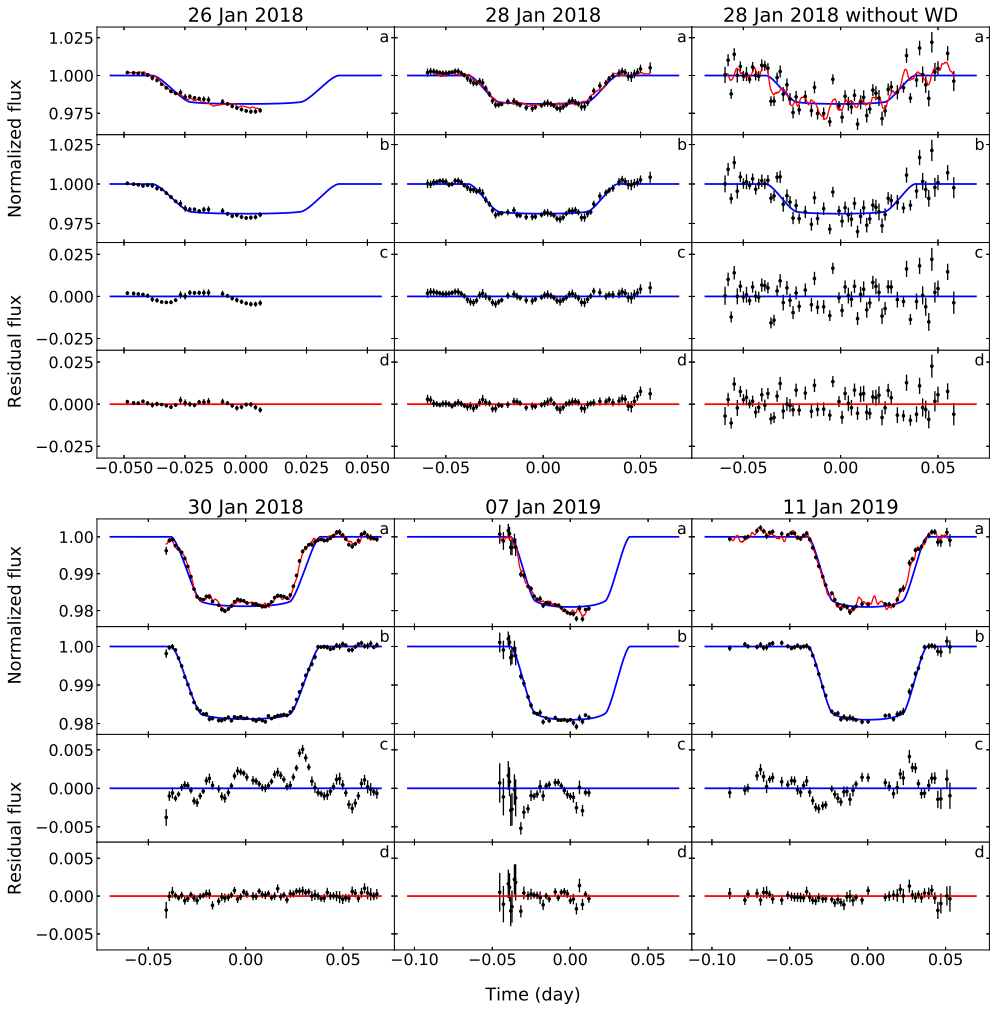

Figure 3.4: The normalized light curves, with and without the wavelet denoising process and the model fits for WASP-50b. The zero points on the time axes are set at the mid-transit ephemerides as shown in Table 3.1.
a - The black errorbars represent the normalized wavelet-denoised flux with associated error. On top of it the MCMC-fitted transit models with and without Gaussian process correlated noise (GP) models are shown with red and blue lines respectively. b - The black error-bars represent the normalized wavelet-denoised data minus the GP noise model. On top of it the MCMC-fitted transit models (without GP) are shown in blue lines. c - The black error-bars represent the residual flux with error after subtracting only the transit models (without GP). d - The black errorbars represent the residual flux plus error after subtracting both the transit model and the GP noise model.

process improves the precision in the deduced parameters significantly.

On the other hand, for GP regression we followed the techniques mentioned above. This technique is also explained in Barclay et al. (2015); Johnson et al. (2015), etc. The two parameters of the regression, α and τ, were used in the MCMC for model fitting. We have kept α and τ variable for each light

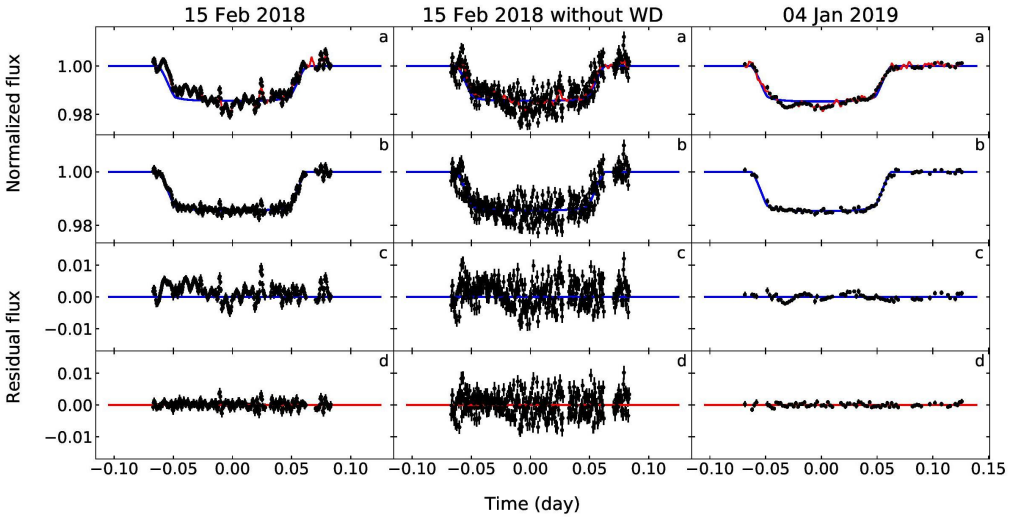

Figure 3.5: The normalized light curves, with and without the wavelet denoising process and the model fits for WASP-12b. The zero points on the time axes are set at the mid-transit ephemerides as shown in Table 3.1.
a - The black errorbars represent the normalized wavelet-denoised flux with associated error. On top of it the MCMC-fitted transit models with and without Gaussian process correlated noise (GP) models are shown with red and blue lines respectively. b - The black error-bars represent the normalized wavelet-denoised data minus the GP noise model. On top of it the MCMC-fitted transit models (without GP) are shown in blue lines. c - The black error-bars represent the residual flux with error after subtracting only the transit models (without GP). d - The black errorbars represent the residual flux plus error after subtracting both the transit model and the GP noise model.

curve. The prior functions of α and τ are also chosen to be uniform. The prior function for α is estimated from the amplitude of fluctuation at the pre-ingress or post-egress points of time and the prior function of τ is estimated from the high-frequency peaks on the Lomb-Scargle periodogram of each light curve.

3.9 Out-of-Transit Observations of the Host Stars

A key element of the capability testing of the telescopes used for transit observations is the proper characterization of the baseline of the light curves that ensures the precision in the transit parameters. For this purpose, we have observed some of the host stars out of transit.

We report the results of the out-of-transit photometric observations of the

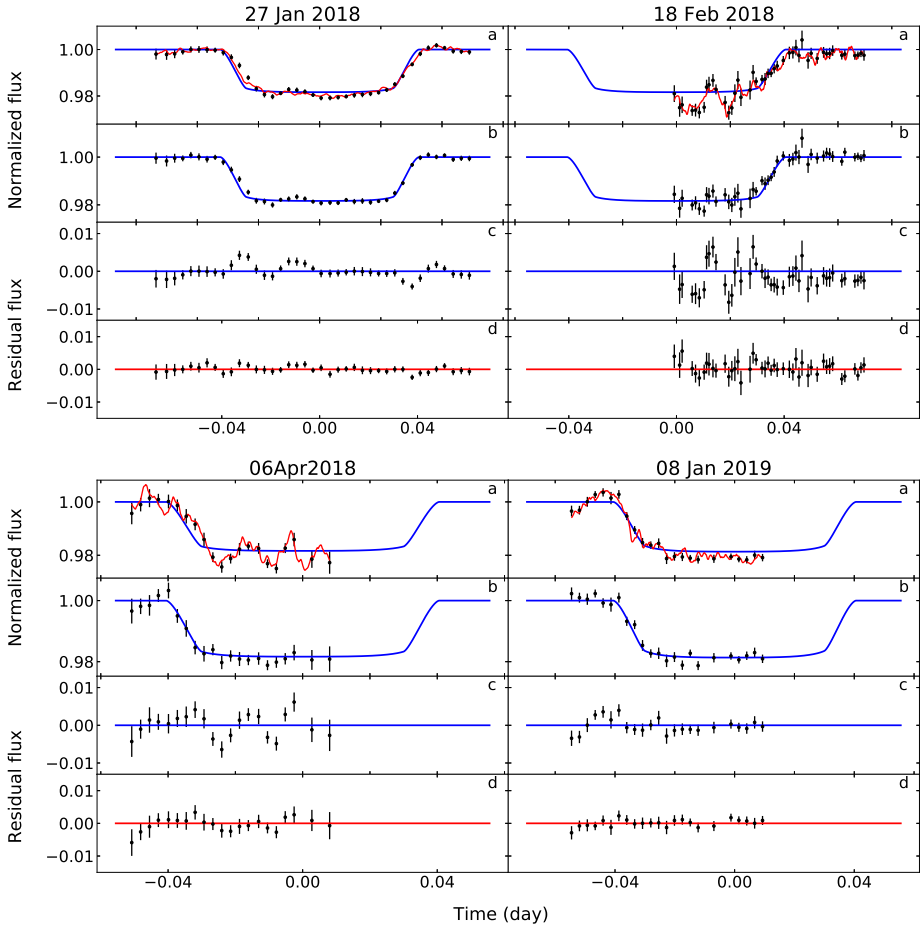

Figure 3.6: The normalized light curves and the model fits for HATS-18b. The zero points on the time axes are set at the mid-transit ephemerides as shown in Table 3.1.
a - The black errorbars represent the normalized wavelet-denoised flux with associated error. On top of it the MCMC-fitted transit models with and without Gaussian process correlated noise (GP) models are shown with red and blue lines respectively. b - The black error-bars represent the normalized wavelet-denoised data minus the GP noise model. On top of it the MCMC-fitted transit models (without GP) are shown in blue lines. c - The black error-bars represent the residual flux with error after subtracting only the transit models (without GP). d - The black errorbars represent the residual flux plus error after subtracting both the transit model and the GP noise model.

host stars WASP-33 and WASP-50. We observed WASP-33 from JCBT on 10 Jan 2019 in V-band at 13:30-15 UT when there was no planetary transit. Similarly, we observed WASP-50 from JCBT on 09 Jan 2019 in R-band at 13:20-15:40 UT right before the transit by its planet. After wavelet denoising, we found a fluctuation of $0.5 \pm 0.05\%$ in the light curve of WASP-33 which after the subtraction of the GP regression model was reduced to $0.3 \pm 0.04\%$. The

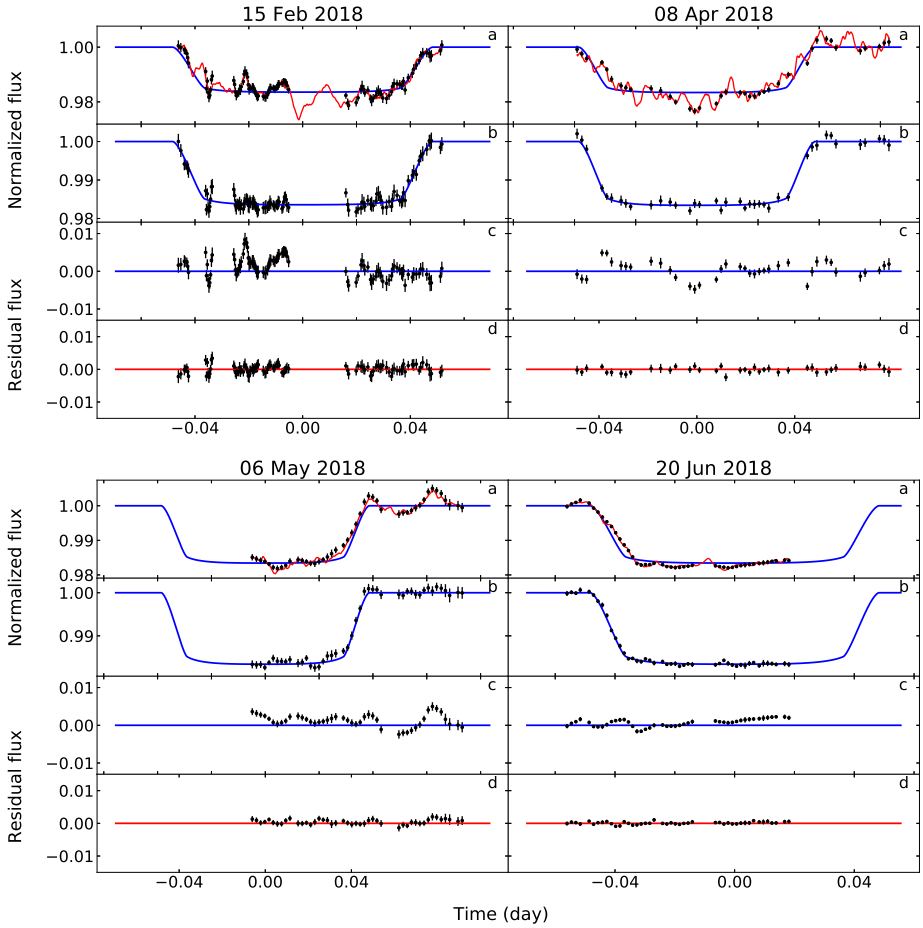

Figure 3.7: The normalized light curves and the model fits for HAT-P-36b. The zero points on the time axes are set at the mid-transit ephemerides as shown in Table 3.1.
a - The black errorbars represent the normalized wavelet-denoised flux with associated error. On top of it, the MCMC-fitted transit models with and without Gaussian process correlated noise (GP) models are shown with red and blue lines respectively. b - The black error-bars represent the normalized wavelet-denoised data minus the GP noise model. On top of it the MCMC-fitted transit models (without GP) are shown in blue lines. c - The black error-bars represent the residual flux with error after subtracting only the transit models (without GP). d - The black errorbars represent the residual flux plus error after subtracting both the transit model and the GP noise model.

peak signal-to-noise ratio (PSNR) was improved from 202 ± 19 to 297 ± 37 after the modeling. The light curve of WASP-50 shows a fluctuation of $0.1 \pm 0.007\%$ and a PSNR of 1119 ± 84, which requires no noise modeling because modeling does not improve it further. The out-of-transit light curves of WASP-33 and WASP-50 during the out-of-transit epoch are shown in Figure 3.8.

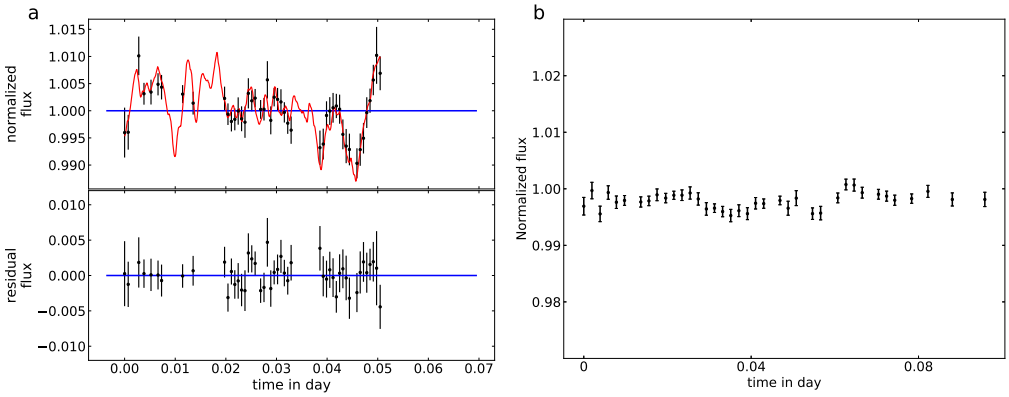

Figure 3.8: a - Light curve of WASP-33 observed on 10 Jan 2019 from JCBT, when there was no predicted transit event. The zero point on the time axis is set at 2458494.074141 BJD-TDB. Top-The black error-bars represent the flux and error values obtained right after wavelet denoising. The red line denotes the GP noise model. Bottom- The black error-bars represent the residual flux after subtracting the GP noise model from the wavelet denoised flux values. b - Pre-ingress wavelet denoised light curve of WASP-50 observed on 09 Jan 2019 from JCBT. The zero point on the time axis is set at 2458493.060419156 BJD-TDB. None of the plots on either side show any detectable transit signature as expected.

Table 3.1: Night-dependent parameters estimated by modeling the transit light curves

Planet	Date of Observation	Mid-transit ephemerides, t_{cen} $(BJD - TDB)$	α	τ
WASP-33 b	09 Dec 2017	$2458097.30431 \pm 0.00000786$	0.0060 ± 0.0001	20.0 ± 0.1
	05 Jan 2018	$2458124.14196 \pm 0.00000769$	0.0017 ± 0.0001	20.0 ± 0.1
	27 Jan 2018	$2458146.09962 \pm 0.00000765$	0.0029 ± 0.0001	19.99 ± 0.1
	26 Dec 2019	$2458479.12739 \pm 0.00000698$	0.0044 ± 0.0001	19.99 ± 0.1
	06 Jan 2019	$2458490.10444 \pm 0.00000696$	0.0039 ± 0.0001	18.99 ± 0.1
WASP-50 b	26 Jan 2018	$2458145.20327 \pm 0.00001057$	0.00141 ± 0.0001	12.0 ± 0.1
	28 Jan 2018	$2458147.15848 \pm 0.00001135$	0.00232 ± 0.0001	13.0 ± 0.1
	30 Jan 2018	$2458149.11405 \pm 0.00000886$	0.00096 ± 0.0001	10.0 ± 0.1
	07 Jan 2019	$2458491.25582 \pm 0.00000783$	0.00240 ± 0.00011	12.0 ± 0.1
	11 Jan 2019	$2458495.16601 \pm 0.00000811$	0.00240 ± 0.00011	12.0 ± 0.1
WASP-12 b	14 Feb 2018	$2458164.14255 \pm 0.00002867$	$0.00100^{+0.00025}_{-0.00014}$	10.0 ± 0.1
	15 Feb 2018	$2458165.23478 \pm 0.00001119$	$0.00293^{+0.0001}_{-0.0004}$	13.0 ± 0.1
	04 Jan 2019	$2458488.29489 \pm 0.00001192$	$0.00300^{+0.0007}_{-0.0001}$	12.0 ± 0.1
HATS-18 b	27 Jan 2018	$2458146.42651 \pm 0.00000928$	0.00099 ± 0.0001	12.0 ± 0.1
	18 Feb 2018	$2458168.21044 \pm 0.00000952$	0.004 ± 0.0001	10.0 ± 0.1
	06 Apr 2018	$2458215.12967 \pm 0.00001042$	0.00599 ± 0.0001	7.0 ± 0.1
	08 Jan 2019	$2458492.45583 \pm 0.00001028$	0.00091 ± 0.0001	7.0 ± 0.1
HAT-P-36 b	15 Feb 2017	$2458165.45507 \pm 0.00000686$	0.00301 ± 0.0001	13.0 ± 0.1
	08 Apr 2018	$2458217.22160 \pm 0.00000755$	0.00175 ± 0.0001	12.99 ± 0.1
	06 May 2018	$2458245.09464 \pm 0.00000737$	0.00099 ± 0.0001	13.0 ± 0.1
	20 Jun 2018	$2458290.22569 \pm 0.00000709$	0.00088 ± 0.0001	13.0 ± 0.1

Note. The values of t_{cen}, A and τ are shown along with 1-σ error margin.

Table 3.2: Planetary properties directly obtained and further deduced by modeling the wavelet denoised transit light curves

Parameters	WASP-33 b	WASP-50 b	WASP-12 b	HATS-18 b	HAT-P-36 b
Transit model parameters					
Impact Parameter, b	0.21 ± 0.002	$0.669^{+0.018}_{-0.007}$	0.339 ± 0.0017	0.3 ± 0.001	0.25 ± 0.007
Scaled Stellar radius, R_*/a	0.28 ± 0.0008	0.133 ± 0.003	$0.333^{+0.0002}_{-0.0017}$	0.273 ± 0.0006	$0.21^{+0.003}_{-0.0002}$
Planet/Star Radius Ratio, R_p/R_*	0.1118 ± 0.0002	0.139 ± 0.0006	0.117 ± 0.0002	0.132 ± 0.0004	0.1199 ± 0.0002
Limb darkening coefficients					
Linear Term for V filter, $C1_V$	0.5 ± 0.01	–	0.42 ± 0.01	0.5 ± 0.01	0.53 ± 0.01
Quadratic Term for V filter, $C2_V$	0.2 ± 0.01	–	0.31 ± 0.01	0.2 ± 0.01	0.23 ± 0.01
Linear Term for R filter, $C1_R$	–	0.4 ± 0.01	0.3 ± 0.01	0.41 ± 0.01	–
Quadratic Term for R filter, $C2_R$	–	0.2 ± 0.01	0.3 ± 0.01	0.18 ± 0.01	–
Linear Term for I filter, $C1_I$	0.31 ± 0.01	0.3 ± 0.01	0.29 ± 0.01	0.31 ± 0.01	0.32 ± 0.01
Quadratic Term for I filter, $C2_I$	0.18 ± 0.01	0.2 ± 0.01	0.31 ± 0.01	0.21 ± 0.01	0.19 ± 0.01
Deduced parameters					
Transit Duration, T_{14} (days)	0.1189 ± 0.0005	0.0764 ± 0.0011	$0.1267^{+0.00009}_{-0.0005}$	0.081 ± 0.0001	$0.093^{+0.0016}_{-0.00007}$
Planet Radius, R_p (R_J)	1.593 ± 0.074	1.166 ± 0.043	1.937 ± 0.056	1.329 ± 0.075	1.277 ± 0.02
Scale Parameter, a/R_*	3.571 ± 0.01	7.51 ± 0.10	$3.0^{+0.016}_{-0.0019}$	3.658 ± 0.008	4.95 ± 0.042
Orbital Separation, a (AU)	0.0239 ± 0.00063	0.0293 ± 0.0013	0.0232 ± 0.00064	0.0174 ± 0.00098	0.0241 ± 0.00047
Orbital Inclination, i (degrees)	86.63 ± 0.03	84.88 ± 0.27	83.52 ± 0.03	85.29 ± 0.013	$87.13^{+0.004}_{-0.13}$
Planet Mass, M_p (M_J)	2.093 ± 0.139	1.4688 ± 0.092	1.465 ± 0.079	1.9795 ± 0.076	1.8482 ± 0.087
Planet Mean Density, ρ_p (gcm^{-3})	0.689 ± 0.074	1.325 ± 0.214	0.267 ± 0.0288	1.1169 ± 0.216	1.175 ± 0.078
Surface Gravity, $\log g_p$ (cgs)	3.275 ± 0.04	3.469 ± 0.029	2.998 ± 0.01	3.45 ± 0.013	3.476 ± 0.027
Equilibrium Temp., T_{eq} (K)[a]	2781.70 ± 41.1	1394.84 ± 32.7	2592.6 ± 57.2	2069.48 ± 45.0	1780.97 ± 18.8

Note. The value of each parameter is shown along with 1-σ error margin. Also, some of the limb darkening coefficients are shown as –, which implies that no transit has been observed for that particular planet in that filter.
[a]Assuming zero Bond albedo and full re-distribution of the incident stellar flux.

Table 3.3: Same as Table 3.2 but without wavelet denoising

Parameters	WASP-33 b	WASP-50 b	WASP-12 b	HATS-18 b	HAT-P-36 b
Transit model parameters					
Impact Parameter, b	0.21 ± 0.003	$0.65^{+0.068}_{-0.005}$	0.339 ± 0.007	0.299 ± 0.019	0.247 ± 0.02
Scaled Stellar radius, R_*/a	0.28 ± 0.003	$0.133^{+0.01}_{-0.002}$	0.332 ± 0.002	0.26 ± 0.005	0.202 ± 0.004
Planet/Star Radius Ratio, R_p/R_*	0.1119 ± 0.003	0.135 ± 0.001	$0.117^{+0.002}_{-0.0002}$	$0.131^{+0.003}_{-0.0002}$	0.1199 ± 0.003
Limb darkening coefficients					
Linear Term for V filter, $C1_V$	0.5 ± 0.03	–	0.4 ± 0.04	0.48 ± 0.04	0.5 ± 0.05
Quadratic Term for V filter, $C2_V$	0.2 ± 0.03	–	0.3 ± 0.04	0.2 ± 0.05	0.2 ± 0.04
Linear Term for R filter, $C1_R$	–	0.39 ± 0.05	0.3 ± 0.05	0.4 ± 0.06	–
Quadratic Term for R filter, $C2_R$	–	0.21 ± 0.05	0.3 ± 0.05	0.21 ± 0.04	–
Linear Term for I filter, $C1_I$	0.3 ± 0.04	0.3 ± 0.06	0.29 ± 0.03	0.31 ± 0.05	0.3 ± 0.06
Quadratic Term for I filter, $C2_I$	0.2 ± 0.04	0.2 ± 0.06	0.3 ± 0.03	0.2 ± 0.05	0.2 ± 0.06
Deduced parameters					
Transit Duration, T_{14} (days)	0.1188 ± 0.0012	0.078 ± 0.003	0.1267 ± 0.0006	0.079 ± 0.0014	0.095 ± 0.0018
Planet Radius, R_p (R_J)	1.601 ± 0.057	1.144 ± 0.057	1.939 ± 0.058	1.341 ± 0.079	1.30 ± 0.03
Scale Parameter, a/R_*	3.571 ± 0.04	$7.485^{+0.1}_{-0.63}$	3.0 ± 0.019	3.724 ± 0.067	4.937 ± 0.1
Orbital Separation, a (AU)	0.0239 ± 0.00071	0.0289 ± 0.002	0.0231 ± 0.00068	0.0176 ± 0.001	0.0239 ± 0.00058
Orbital Inclination, i (degrees)	86.6 ± 0.05	$85.01^{+0.09}_{-1.01}$	$83.52^{+0.08}_{-0.16}$	85.38 ± 0.33	87.13 ± 0.23
Planet Mass, M_p (M_J)	2.093 ± 0.1404	1.4692 ± 0.092	1.465 ± 0.079	1.9794 ± 0.077	1.848 ± 0.088
Planet Mean Density, ρ_p (gcm^{-3})	0.6774 ± 0.095	1.2958 ± 0.21	0.266 ± 0.029	1.088 ± 0.217	1.042 ± 0.09
Surface Gravity, $\log g_p$ (cgs)	3.268 ± 0.037	$3.463^{+0.02}_{-0.1}$	2.99 ± 0.015	3.46 ± 0.03	3.432 ± 0.036
Equilibrium Temp.[a], T_{eq} (K)	2784.09 ± 45.9	1404.63 ± 58.3	2596.19 ± 58.1	2052.09 ± 51.4	1789.92 ± 23.2

Note. The value of each parameter is shown along with 1-σ error margin. Also, some of the limb darkening coefficients are shown as –, which implies that no transit has been observed for that particular planet in that filter.
[a]Assuming zero Bond albedo and full re-distribution of the incident stellar flux.

3.10 Results of Follow-up Observation and Discussion

The Bayesian retrieval analysis (MCMC) on the observed transit light curves allowed us to update the physical parameters of the hot Jupiters are updated with much more precise values. This high precision can be attributed to the high photometric SNR (see Table 2.3) and the techniques adopted to reduce

the fluctuations in the light curves. The reduced transit light curves with the best fit models are shown in Figure 3.3-3.7. As evident from these figures, the fluctuations in the residual light curves are comparable or even less than the uncertainties (errors) in the flux values. As we can see from these figures, after the first stage of preprocessing i.e., wavelet denoising, the light curves show different levels of fluctuations for different host stars. Transit light curves for WASP-33b show maximum fluctuations due to pulsation. This is consistent with the previous observations by Johnson et al. (2015); von Essen et al. (2014). These fluctuations could be significantly reduced by GP regression. The fluctuations in the transit light curves of WASP-50b, HATS-18b and HAT-P-36b are found to be moderate after wavelet denoising and the subsequent GP noise modeling has further improved the corresponding light curves. However, the transit light curves for WASP-12b are found to show minimum fluctuations after wavelet denoising and hence, wavelet denoising alone would be sufficient for noise reduction in this case.

The total transit durations (T_{14}) are estimated from the model parameters using the relation as follows:

$$T_{14} = \frac{P}{\pi} \arcsin\left(\frac{\sqrt{(1+R_p/R_*)^2 - b^2}}{\sqrt{(a/R_*)^2 - b^2}}\right) \tag{3.14}$$

The masses of the planets were determined by using the radial velocity of the host stars and the present updated values of the inclination angle using the relation:

$$M_p = M_*^{2/3} \left(\frac{P}{2\pi G}\right)^{1/3} \frac{K_{RV}\sqrt{1-e^2}}{\sin i}, \tag{3.15}$$

using the fact that, $M_P \ll M_*$. In the absence of any observational information, we have assumed circular orbits i.e., $e = 0$. For a few targets, the orbital eccentricities have been reported to be extremely low (Gillon et al., 2011; Turner et al., 2016) and therefore the assumption of circular orbit is justified.

We derived the surface gravity of the planets g_p as well by using the relation

(Southworth, Wheatley, & Sams, 2007):

$$\log g_p = \log \left(\frac{2\pi K_{RV} \sqrt{1-e^2} (a/R_*)^2}{P \sin i (R_p/R_*)^2} \right) \tag{3.16}$$

We also estimated the equilibrium temperatures T_{eq} of the planets by assuming zero Bond albedo and full re-distribution of the incident stellar flux. In term of the stellar effective temperature T_{eff}, T_{eq} can be written as

$$T_{eq} = T_{eff} \left(\frac{R_*}{2a} \right)^{1/2} \tag{3.17}$$

The values of M_p, T_{eq} and $\log g_p$ derived from the modeling of the transit light curves preprocessed with wavelet denoising are presented in Table-3.2. The same without the wavelet denoising process are presented in Table-3.3.

3.11 Conclusion

We have observed the transit events of five hot Jupiters of masses ranging from 1.17 M_J (WASP-33b) to 1.98 M_J (HATS-18b) and radii ranging from 1.15 R_J (HAT-P-36b) to 1.82 R_J (WASP-12b) by using two facilities in India at different places- 1.3m JCBT and 2m HCT. We have obtained the transit light curves of these targets with very high transit SNR (transit-depth/noise). This high transit SNR can be ascribed to the high photometric SNR owing to the large apertures of the telescopes used. However, apart from the noise emanating from the stellar pulsation, we find that noise from the fluctuating sky transparency contaminates the transit signals significantly. This is a major drawback of the ground-based observations even with a sufficiently large aperture of the telescope used. We have demonstrated that wavelet denoising can efficiently suppress the uncorrelated noises to a great extent. We have also shown that the correlated noises can be estimated with high accuracy and can be subtracted from the time-series photometric data by using the Gaussian pro-

cess regression. Both of these techniques are included in the modeling pipeline we have developed. Using the self-developed state-of-the-art pipelines for reduction and photometry (`pyapphot`) and for modeling of the light curves, we could update the transit parameters of the planets with very high precision (less 1-σ error) compared to the previously published results. Hence, by combining the host star properties, the physical parameters obtained through the radial velocity method and that obtained by precise transit observations, the values for the mass, radius, mean density, surface gravity etc. of the planets are obtained with improved precision. We have published the results in the Astrophysical Journal and due to the high precision achieved the publication has been selected as the reference for default parameters of the five planets by the NASA Exoplanet Archive.

Finally, the high stability ($\sim 500ppm$) of the light curves obtained from the observations of the stars during the out-of-transit epochs implies that the observational facilities along with the backend instruments are capable of detecting the signature of planets not yet discovered.

Chapter 4

Transit Spectroscopy[1]

4.1 Introduction

Transit spectroscopy is an essential tool to probe into the physical structure and the chemical composition of the atmospheres of the close-in planets. While transit photometry provides important physical properties of exoplanets, it cannot explore the planetary atmospheres. During the transit epoch of an exoplanet across its parent star, a part of the starlight transmits through the planetary atmosphere. The interaction of this transmitted starlight with the atmospheric material through absorption and scattering is imprinted on top of the stellar spectra. Hence, this method is also known as transmission spectroscopy. As pointed out for the first time by Seager & Sasselov (2000), it is the transmission spectroscopic method that can probe the physical and chemical properties of the atmosphere of exoplanets having near edge-on orientation. Transit or transmission spectra are calculated by taking spectra during and outside a transit event and then the difference spectra are divided by the out-of-transit spectra to get the transit depth as a function of wavelength.

Since this method requires us to calculate the differential spectra, signal to

[1] *Part of this chapter is published in The Astrophysical Journal, Sengupta, Chakrabarty and Tinetti, vol. 889:181, 2020.*

noise ratio (SNR) is a huge concern for transit spectra. For this reason, so far the transit spectra have been acquired predominantly for the hot Jupiters due to their enormous size (radius $\gtrsim$1 R_J) as well as the presence of thick atmospheres. High-resolution transmission spectra can tell us about the abundance of the different atomic and molecular species in the atmospheres. From the optical spectra, we can determine the abundance of the atomic species such as Na, K, Ca, etc. and on the other hand, infrared spectroscopy can help us determine the abundance of the molecular species such as H_2O , CO_2 , CH_4 , O_2 , CO, etc. Due to limited signal content, so far a few high-resolution transit spectra of some hot Jupiters have been taken only in the optical region by combining a bulk amount of spectra observed over multiple transit events of each planet with long exposures. In the infrared, the observed spectra are either of extremely low resolution (R$\sim$100) or calculated from multi-band photometry.

On the other hand, low-resolution transmission spectra can be acquired with relatively higher SNR. From such spectra broad absorption bands of e.g. H_2O , TiO, VO etc. can be detected. Also, low-resolution spectra give us information about the physical structure of the atmosphere such as pressure and temperature at different layers etc. Moreover, by analyzing the slope of the transit spectra from the visible region to the near-infrared (NIR) region, information about clouds and haze can be found out. A substantial number of low-resolution spectra have been obtained so far both in the optical and the infrared region using telescopes such as Hubble Space Telescope (HST), Spitzer Space Telescope (SST), Gran Telescopio Canarias (GTC), Gemini North etc. (Bean et al., 2011; Pallé et al., 2016; Sing et al., 2016; Stevenson et al., 2014; Tinetti et al., 2007a, etc.).

4.2 Overview of Previous Transit Spectroscopic Observations

After the discovery of the first planet using transit photometry namely HD 209458 b (Charbonneau et al., 2000; Henry et al., 2000), immediately many theoretical models predicted the possibility of detection of excess absorption lines due to the exoplanets' atmospheres in the strong resonance lines of Na I and other alkali metals in optical transmission spectra (Brown, 2001; Seager & Sasselov, 2000). This urged the observers across the world to acquire transmission spectra during transit in search for signature from planetary atmospheres.

4.2.1 High Resolution Observations

Charbonneau et al. (2002) made the first discovery of absorption lines in the medium-resolution (resolution, R ∼5540) transmission spectra of HD 209458 b due to Na I in the atmosphere using the Space Telescope Imaging Spectrograph (STIS) on board the Hubble Space Telescope (HST). After that, exospheric absorption was also detected for HD 209458b in several UV lines by Vidal-Madjar et al. (2003, 2004). The early ground-based attempts to detect absorption in the optical transmission spectra of bright transiting systems could measure only upper limits, due to limited observations of only a single effective transit (e.g., Arribas et al., 2006; Bundy & Marcy, 2000; Moutou et al., 2001; Narita et al., 2005, etc.). Redfield et al. (2008) detected absorption lines due to Na I in the transit spectra of another hot Jupiter, HD 189733 b, using multiple in-transit and out-of-transit high-resolution spectra (R∼60000) acquired from the High Resolution Spectrograph (HRS) at the backend of the 9.2 m Hobby-Eberly Telescope (HET). They reported the results with very high SNR (for in-transit ∼1600 and for out-of-transit ∼3400) and the relative absorption is found to be ∼3 times larger than that detected for HD 209458 b by Charbonneau et al. (2002). In the same year Snellen et al. (2008) reported the detection of excess

absorption in the Sodium Doublet lines of the planet HD 209458 b with higher value with greater SNR than reported by Charbonneau et al. (2002).

The main caveat to this method is that the signatures produced by molecular species in the planets' atmospheres are orders of magnitude weaker than those of the telluric and stellar lines. Snellen et al. (2010) overcame this hindrance by merging the information of thousands of CO rotational-vibrational lines in HD 209458 b transit spectra by applying a cross-correlation technique to high-resolution spectroscopy (R ∼100000) with the Cryogenic InfraRed Echelle Spectrograph (CRIRES) at the Very Large Telescope (VLT). This was the first confirmation of the presence of CO in the atmosphere of that planet. Moreover, Snellen et al. (2010) also probed into the atmospheric dynamics by finding a residual blueshift in the spectra of ∼2 kms^{-1} which they attributed to the day-to-night wind at the terminals of the planet.

Ever since, the field of atmospheric characterization using cross-correlation and high-resolution spectroscopy with ground-based large-aperture (8-10 m) telescopes and their backend instruments has flourished. There have been many reports of detection of various abosrption lines in high-resolution transit spectra due to species like H_2O (Birkby et al., 2013; Brogi et al., 2016; Sánchez-López et al., 2019), CO (Brogi et al., 2016; de Kok et al., 2013), atomic Fe and Ti (Hoeijmakers et al., 2018), TiO (Nugroho et al., 2017), Na, K, Ca and Hα (Chen et al., 2020; Keles et al., 2019; Turner et al., 2020; Wood et al., 2011), etc.

4.2.2 Low Resolution Observations

After the detection of Na I detection of HD 209458 b using medium-resolution spectra, Ballester, Sing, & Herbert (2007) acquired low-resolution transit spectra of the same planet using the STIS instrument of HST in the NUV and visible region. They detected broadband absorption at shorter wavelengths attributed to hot hydrogen in the upper atmosphere of the planet indicating

hydrodynamic outflow of gases. Meanwhile, there have been several attempts to detect the signature of water on the transit spectra. However, observers either found flat transit spectra with the absence of water absorption in the NIR (Berta et al., 2012; Gibson et al., 2012; Grillmair et al., 2007) or extremely weak water signatures (Deming et al., 2013). However, Tinetti et al. (2007a) report detectable water signature in the mid-infrared by comparing the transit depth calculated from the photometric observations in three different Infrared Array Camera (IRAC) bands of Spitzer Space Telescope (Beaulieu et al., 2008; Knutson et al., 2007). The transit depth calculated in the IR is found to be less than that calculated in the visible wavelength denoting visible-to-NIR slope in the transit spectra. The absence of water can be attributed to low water abundance with a clear atmosphere or obscuration of the absorption features by clouds or haze present in the atmosphere. On the other hand, the visible-to-NIR slope can be explained by the cloudy or hazy planetary atmospheres or the presence of starspots.

Sing et al. (2016) present the transit spectra of 8 hot Jupiters observed using the low-resolution spectroscopic mode of the Wide Field Camera 3 (WFC3) on board HST combining with previous observations of HD 189733 b and HD 209458 b along with models to explain the features. Transit spectra of the planets such as WASP-17 b, WASP-19 b, WASP-39 b and HAT-P-1 b show clear absorption features of Na and K as well as H_2O at 1.4 μm. Planets such as HD 209458 b, HD 189733 b, HAT-P-12 b, WASP-6 b show weak absorption features which can be modeled well with cloud-decks and haze. On the contrary, planets such as WASP-12 b and WASP-31 b almost show no absorption feature indicating the presence of thick clouds or haze. Of late, Carter et al. (2020) have reported the detection of Na and K lines in the transit spectra of WASP-6 b, which were not detected by Sing et al. (2016), along with signatures of H_2O at 1.4 μm.

4.3 Transit Spectra Observed by Us

We monitored some hot Jupiters spectroscopically in the optical region during and outside the transit events. We chose some of the bright sources ($V_{mag} < 11$ for high resolution and $V_{mag} < 13$ for low resolution) for that purpose. We chose the host stars with confirmed planets. We used the online database, namely the Exoplanet Transit Database [2], to get the predicted transit epochs of the known planets (Poddaný, Brát, & Pejcha, 2010). We have acquired high resolution spectra of some of the host stars during and outside the transit events using VBT. We have also acquired some low resolution spectra of hot Jupiters using VBT and HCT. The reduction and processing of the spectra are underway.

4.3.1 Details of Observation, Reduction and Analysis

We took transit spectroscopic observations using the Echelle Spectrograph of the 2.34-m Vainu Bappu Telescope, VBO, Kavalur and the $4k \times 4k$ CCD placed at the backend. We used the slitless mode of the spectrograph which gives a resolution, R∼27000. We took some in-transit spectra and out-of-transit spectra of the planet-hosting stars KELT-4A and HD 149026. The spectrograph covers a wavelength region of ∼4000-10000 $\mathring{A}$.

The reduction has been performed using IRAF (Image Reduction and Analysis Facility) Echelle package. Reduction involves bias correction, flat normalization, flat fielding, aperture extraction and wavelength calibration. For calibration, we used the iron-nickel (Fe-Ne) lamp and the calibration standard chart produced by the European Southern Observatory (ESO). After getting the final wavelength calibrated spectra we combined the in-transit spectra and the out-of-transit spectra and calculated the ratio of the difference between them to the out-of-transit spectra at the Sodium Doublet wavelength region

[2] http://var2.astro.cz/ETD/predictions.php

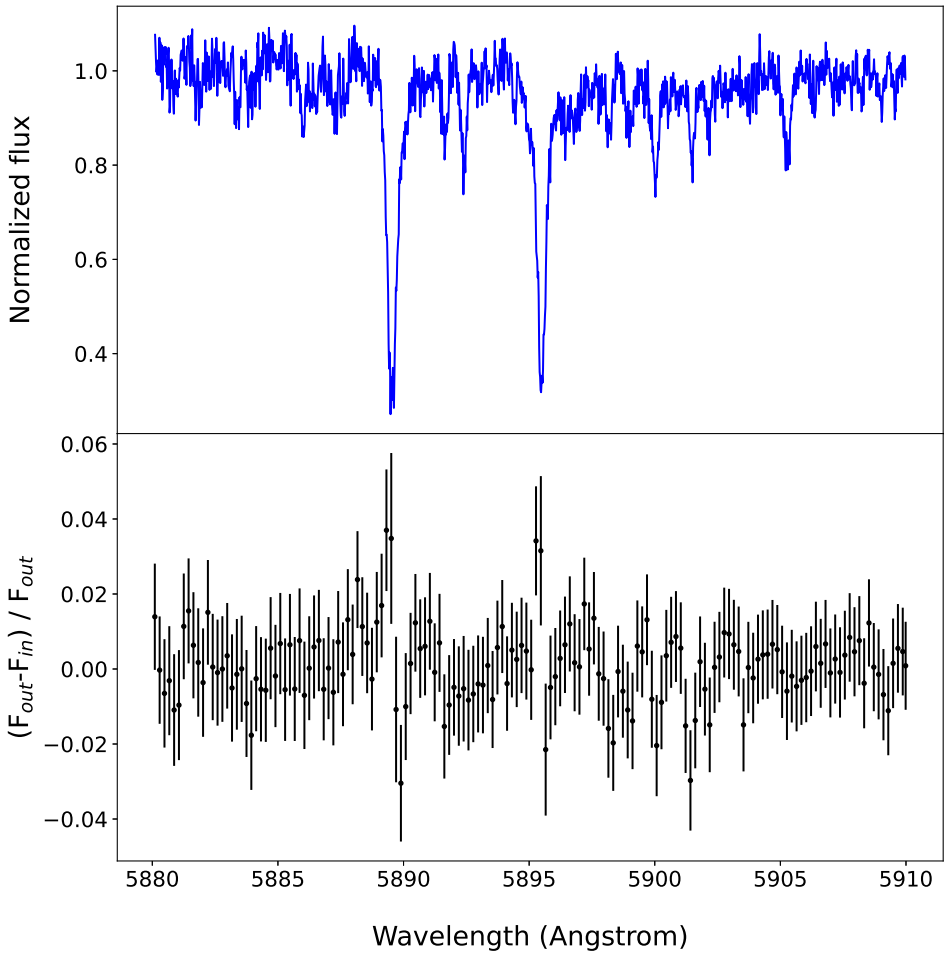

Figure 4.1: Top: Spectrum of the host star KELT-4A near the Na I doublet. Bottom: The ratio of the difference between the combined out-of-transit spectrum (F_{out}) and the combined in-transit spectrum (F_{in}) to F_{out} at the same wavelength region.

(5880-5910 $\mathring{A}$) to find out any planetary signature.

4.3.2 Results and Discussion

The combined spectroscopic SNR of KELT-4A b for in-transit was 110 and for out-of-transit was 90. Again, the combined spectroscopic SNR of HD149026 b for in-transit was 125 and out-of-transit was 260. Figure 4.1 and Figure 4.2 show the high resolution transit spectra for the host stars KELT-4A and HD149206 respectively over the wavelength region 5880-5910 $\mathring{A}$. We find some signal on the transit spectrum of KELT-4A at the Sodium D-lines (5889.95

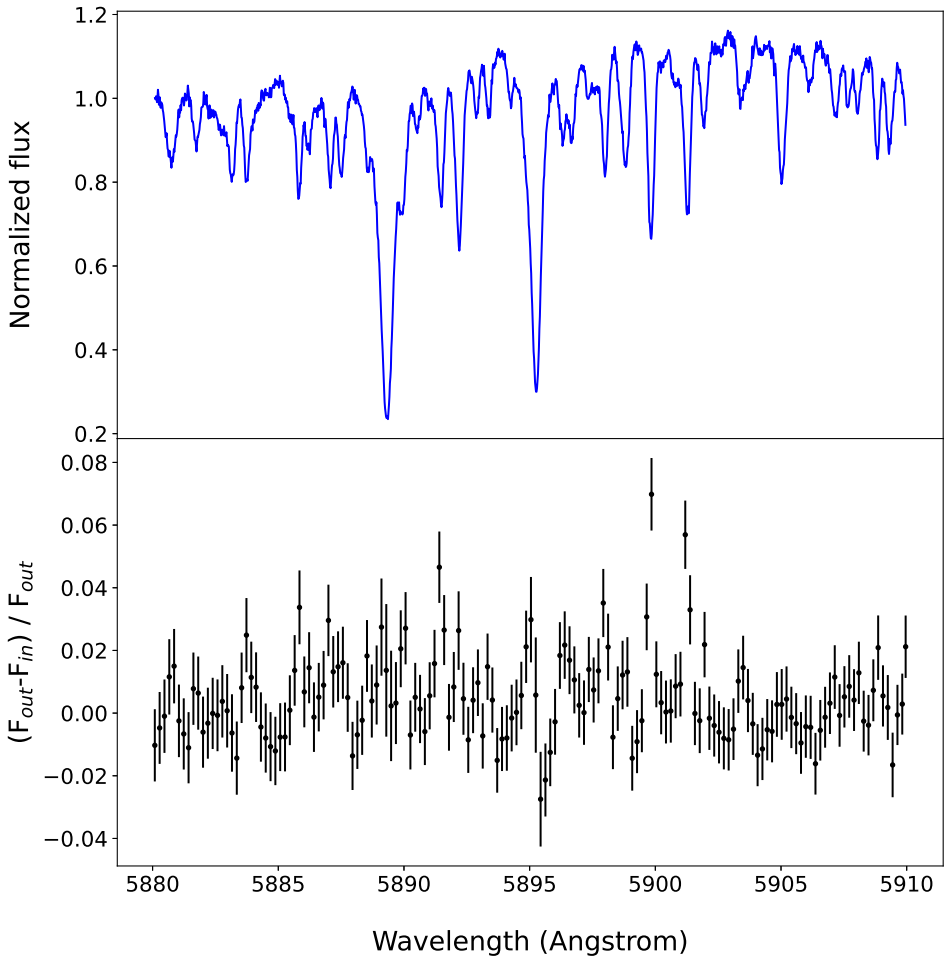

Figure 4.2: Top: Spectrum of the host star HD 149026 near the Na I doublet. Bottom: The ratio of the difference between the combined out-of-transit spectrum (F_{out}) and the combined in-transit spectrum (F_{in}) to F_{out} at the same wavelength region.

$\mathring{A}$ and 5895.92 $\mathring{A}$), indicating the contribution from the atmosphere of the planet KELT-4A b. However, the signal strength is not enough to extract any information about the planets‘ atmospheres.

We have also acquired low resolution transit spectra of those two host stars along with some more stars hosting hot Jupiters such as WASP-33, WASP-43 etc. using the Hanle Faint Object Spectroscopic Camera (HFOSC) with the grism mode at the backend of HCT and OMR spectrograph at the backend of VBT. The reduction and analysis of those spectra are underway.

4.4 Overview of Existing Models of Transmission (Transit) Spectra

With the advancement in the observational techniques for studying the exoplanets over the course of time, theoretical models have also evolved and become more and more precise and exhaustive in an attempt to realize all the physical and chemical processes occurring in the planetary atmospheres. Modeling of the transit or transmission spectra involves modeling of the planetary atmospheres, solving the equations that represent the interactions between light and the atoms and molecules present in the atmospheres, and interpretation of the spectral features in the context of planetary atmospheres. The basic concepts of modeling of exoplanetary atmospheres have been adopted from the early models of the solar system planets and moons (Chamberlain & Hunten, 1987; Marley & McKay, 1999; McKay, Pollack, & Courtin, 1989, etc.). These models are based on the solution of the radiative transfer equations using algorithms described in Chandrasekhar (1960); Peraiah & Grant (1973); Toon et al. (1989); etc. These theories have been modified and applied to the study of brown dwarfs and extra-solar giant planets. Models described in Burrows et al. (1997); Fortney et al. (2005, 2008, 2013); Marley et al. (1999, 1996); Morley et al. (2012, 2015); Saumon & Marley (2008), etc. are based on the algorithm by Toon et al. (1989), whereas, the models described in Sengupta, Chakrabarty, & Tinetti (2020); Sengupta & Marley (2009, 2010), etc. are based on the algorithm by Peraiah & Grant (1973).

Initial models of the transmission spectra (Barman, 2007; Brown, 2001; Seager & Sasselov, 2000; Tinetti et al., 2007a,b, etc.) mostly focused on the early detected transiting planets, HD 209458 b and HD 189733 b and at the same time, elaborately studied the effects of alkali metals, H_2O and clouds present in the atmospheres. Articles, such as Barstow et al. (2017); Madhusudhan & Seager (2009); Sing et al. (2016); Stevenson et al. (2014, 2016); Tinetti et al.

(2007a); etc., have presented both forward models as well as retrieval techniques for the observed transmission spectra of several hot Jupiters such as HD 209458 b, HD 189733 b, WASP-12 b, WASP-19 b, WASP-39 b, HAT-P-1 b, HAT-P-26 b, etc. These studies shed light on the various factors that affect the transmission spectra, such as absorption due to metals (e.g., Na, K etc.), absorption due to H_2O , TiO and VO, effects of clouds, haze and aerosols, flattening of the spectra due to the presence of clouds or haze etc. On the other hand, the implications for the spectra and the atmospheric structure of hot Jupiters from the Carbon-to-Oxygen ratio (C/O) estimated from the observed transmission spectra have been examined in detail by Madhusudhan et al. (2011a); Madhusudhan & Seager (2011); Madhusudhan et al. (2011b); Mollière et al. (2015); etc. There are many review articles and texts that provide insights into the atmospheric processes of the exoplanets such as Catling & Kasting (2017); Fortney (2018); Heng & Kitzmann (2017); Pierrehumbert (2010); Seager (2010); Tinetti, Encrenaz, & Coustenis (2013); etc. Recently, Chakrabarty & Sengupta (2020); Goyal et al. (2019, 2018); Heng, Malik, & Kitzmann (2018); Sengupta, Chakrabarty, & Tinetti (2020); etc. have presented more detailed and exhaustive grid-based models for transmission spectra, both generic parameter-based and planet-specific, by incorporating more and more physical and chemical processes.

An essential factor of the atmospheric modeling is the calculation of the pressure and temperature with varying altitudes which is represented by a pressure-temperature (P-T) profile. Although most of the models mentioned above calculate the P-T profiles self-consistently by simultaneously solving the radiative-convective equilibrium, chemical equilibrium and hydrostatic equilibrium equations, analytical models of P-T profiles have been published, mostly focusing on strongly irradiated planets, by Guillot (2010); Hansen (2008); Parmentier & Guillot (2014); Parmentier et al. (2015); Robinson & Catling (2012); etc. Calculation of both the atmospheric density and the absorption and scattering coefficients of the various chemical species in an atmosphere requires

the knowledge of their abundance, which is calculated as a function of local temperature and pressure, surface gravity and metallicity (e.g., Asplund et al., 2009; Lodders, 2003; Lodders & Fegley, 2002, etc.). Calculation of the absorption and scattering coefficients makes use of the atomic and molecular line-lists available, such as HITRAN (Gordon et al., 2017), Exomol (Tennyson et al., 2016), etc.

All these calculations are usually performed with the help of a single code containing many libraries and modules. These codes or pipelines are characterized by their performance, time taken and resources (number of cores, hence, power) consumed. Two of such codes are explained below briefly which are open-source and have been used by us for ideation, modification as well as access to the databases used in those codes.

4.4.1 Exo-Transmit

Exo-Transmit (Kempton et al., 2017) is a code based on the C language, available in the public domain[3]. It calculates the transmission spectra by using the Beer-Bouguer-Lambert law. The code takes various inputs from the user, such as a file containing P-T profiles, surface gravity, planet radius, stellar radius, the pressure of cloud top etc. and calculates the transit depth at different wavelengths ranging from 0.3 μm to 30 μm . The code also provides two databases: the equation of states (EOS) and the atomic and molecular absorption cross-sections. The equation of states (EOS) of various species that provide the abundances for the major atmospheric constituents as a function of temperature and pressure are calculated based on the solar system abundances of Lodders (2003). The abundances of all the species are in chemical equilibrium and they are provided for a temperature range of 100-3000 K, for a pressure range of 10^{-9}-1000 bars and for metallicity values of 0.1, 1, 5, 10, 30, 50, 100, and 1000 times the solar value. Abundances are provided for both the conditions: ignoring condensation and considering condensation with rain-

[3] https://github.com/elizakempton/Exo_Transmi

out. This database also includes abundances at solar composition but with varying C/O ratios ranging from 0.2 to 1.2, with 0.5 being the solar system value. Opacities for 28 molecular species as well as Na and K are tabulated at a fixed spectral resolution of 1000 over the same range of pressure and temperature and for wavelengths ranging from 0.3 μm to 30 μm. The line list used to generate the molecular opacity is tabulated in Lupu et al. (2014). The molecular opacities are also adopted from the well-known and well-used database of Freedman et al. (2014); Freedman, Marley, & Lodders (2008). Users can choose the active elements among the 30 species for the calculation of the absorption coefficients.

4.4.2 TauREx

TauREx (Tau Retrieval for Exoplanets) is an open-source code[4] written in Python that provides both forward models as well as bayesian inverse atmospheric retrieval framework (Waldmann et al., 2015a,b). It calculates the transmission spectra by using the Beer-Bouguer-Lambert law and besides, it can calculate the emission spectra from the planets. It intakes a parameter file that contains a vast number of user-configurable parameters for different purposes. Users can define the basic parameters such as planetary radius, stellar radius, metallicity, surface gravity of the planets, ranges of pressure, temperature and wavelength, etc., the active elements (partaking in atomic and molecular absorption) and their mixing ratios, pairs involved in collision-induced absorption (CIA) and their mixing ratios, scattering mechanism, viz., Rayleigh, Mie or both, cloud properties etc. Additionally, users either can define their P-T profiles or define isothermal P-T profiles or define the parameters used in the formalism described by Parmentier & Guillot (2014). In case, users use the code for retrieval, they can define the fitting algorithm and the additional fitting parameters. TauREx adopts line-lists from ExoMol (Tennyson & Yurchenko, 2012; Tennyson et al., 2016). The opacity data are provided

[4] https://github.com/ucl-exoplanets/TauREx_public

as wavelength-dependent low-resolution cross-sections, high-resolution cross-sections and k-tables (for the correlated-k method of calculation).

4.5 Basic Models Developed by Us

At first, we developed some basic models of the atmospheres of the hot Jupiters and their transmission spectra by assuming the entire atmosphere to comprise of a few species such as H2, H_2O, CO, CH4 etc. and only considering the effect of extinction due to true absorption and scattering. This laid the stepping stones towards the complete modeling of atmospheres of the hot Jupiters.

4.5.1 Underlying Principle

The transmission spectra of the exoplanets are expressed in terms of the wavelength-dependent transmission depth which is given by, e.g., Kempton et al. (2017); Tinetti, Encrenaz, & Coustenis (2013)

$$D_\lambda = 1 - \frac{F_{in}}{F_{out}}, \tag{4.1}$$

where $F_{out} = F_\star$ is the out-of-transit stellar flux. The in-transit stellar flux, F_{in}, which is the flux of the host star that transmits through the planetary atmosphere is given by

$$F_{in} = \left(1 - \frac{R_{PA}^2}{R_\star^2}\right) F_\star + F_P, \tag{4.2}$$

where R_{PA} is the combined base radius R_P of the planet and its atmosphere, $R_\star$ is the radius of the host star and F_P is the additional stellar flux that passes through the planetary atmosphere and suffers absorption and scattering. Clearly, the first term in the right-hand side of the above expression represents the stellar radiation during the transit of the planet and its atmosphere and

the second term represents the additional stellar radiation filtered through the planetary atmosphere. The base radius R_P is the planetary radius at which the planet becomes opaque at all wavelengths. For a rocky planet, R_P is the distance between the center to the planetary surface. But for gaseous planets, R_P is the height of the region below which no radiation can transmit from.

The transmission spectra is also expressed in terms of the wavelength dependent planet-to-star radius ratio which is the square root of the transit depth. From the above equations, the transmission depth (D_λ) and the wavelength-dependent radius ($\frac{R^2_{P,\lambda}}{R^2_*}$) of the can be written in a simple form

$$D_\lambda = \frac{R^2_{P,\lambda}}{R^2_*} = \frac{R^2_{PA}}{R^2_\star} - \frac{F_P}{F_\star}. \tag{4.3}$$

The stellar radiation F_P that filters through the planetary atmosphere is calculated from the incident stellar intensity. If the calculation of transmission spectra assumes only absorption of starlight passing through the planetary atmosphere, Beer-Bouguer-Lambert law can be used which is given by

$$I(\lambda) = I_0(\lambda)e^{-\tau_\lambda/\mu_0}, \tag{4.4}$$

where I_0 is the intensity of the incident stellar radiation, I is the stellar intensity filtered through the planetary atmosphere, τ is the optical depth along the ray path and μ_0 is the cosine of the angle between the direction of the incident starlight and the normal to the planetary surface. Due to the edge-on orientation, $\mu_0 = 1$ has been adopted in our studies such that the starlight during planetary transit always incident along the normal to the planetary atmosphere.

4.5.2 Basic Definitions for Irradiated Atmospheres

The bolometric flux (flux integrated over wavelength) from a star can be expressed in terms of its effective temperature, T_*, as,

$$F_{bol,*} = \sigma_{SB} T_*^4, \tag{4.5}$$

where σ_{SB} is the Stefan-Boltzmann constant, the bolometric flux received by an irradiated planet at its substellar point can be expressed in terms of irradiation temperature, T_{irr0} which can be related to the T_* as (Guillot, 2010),

$$T_{irr0} = T_* \left(\frac{R_*}{D} \right)^{\frac{1}{2}}, \tag{4.6}$$

where R_* and D denote the stellar radius and the distance between the star and the planet respectively. However, the total energy received by the planet averaged over the entire planetary surface is expressed in terms of its equilibrium temperature T_{eq0}, which is related to T_{irr0} as,

$$T_{eq0} = \frac{1}{\sqrt{2}} T_{irr0} \tag{4.7}$$

Note that, the suffix 0 in T_{eq0} and T_{irr0} denotes that these temperatures are for the case when no incident light is reflected back by the planetary atmosphere. However, the entire energy irradiated on the planet is not received by it, a part is reflected back by the planet, which is governed by the factor Bond albedo, A_B . The equilibrium temperature corresponding to finite Bond albedo, A_B is given by (Guillot, 2010; Parmentier et al., 2015),

$$T_{eq}^4 = 4f(1 - A_B) T_{eq0}^4, \tag{4.8}$$

where f is the flux parameter. This parameter helps us adopt the correct equilibrium temperature depending on whether we limit our study to the substellar point ($f = 1$) or averaged over the dayside ($f = 0.5$) or whether we study the

heat received and re-emitted from the entire planetary surface ($f = 0.25$). However, the parameter f does not tell us anything about the temperature contrast between the dayside and the night-side. These close-in planets are so close to the host stars that they must be tidally locked. This means one side of such a planet always faces the host star, which is the dayside and the other side is always the night-side. For this reason, these planets can show high day-night temperature contrast which has also been found from observation (Arcangeli et al., 2019; Keating & Cowan, 2017, etc.). However, due to the advection process in the atmosphere, heat from the dayside does get transferred to the night-side and the efficiency of heat transfer is characterized by the parameter ϵ which denotes the heat re-circulation (also, re-distribution) efficiency (Cowan & Agol, 2011; Keating & Cowan, 2017, etc.). The dayside (T_d) and night-side (T_n) average temperatures can be expressed in terms of ϵ as (Cowan & Agol, 2011; Guillot, 2010; Keating & Cowan, 2017; Parmentier et al., 2015, etc.),

$$T_d^4 = T_{eq0}^4(1 - A_B)\left(\frac{8}{3} - \frac{5}{3}\epsilon\right) \quad and \tag{4.9}$$

$$T_n^4 = T_{eq0}^4(1 - A_B)\epsilon \tag{4.10}$$

Clearly, $\epsilon = 1$ implies $T_d = T_n$ which is equivalent to the case of $f = 0.25$ in Equation 4.8. Moreover, the planets' atmospheres can also receive heat from various other sources such as heat from the interior radiated (for gaseous planets) or released by tectonic and volcanic activities (for planets with rocky surfaces), tidal heating etc., which altogether can be expressed in terms of internal temperature, T_{int} and these internal sources contribute to the total emission from the planets. The total effective temperature of the planets is given by (Parmentier et al., 2015, etc.),

$$T_{eff}^4 = T_{eq}^4 + T_{int}^4 \tag{4.11}$$

However, for old close-in planets (age>100 Myr) the internal temperature is

negligible with respect to the irradiation or equilibrium temperature (Burrows et al., 1997).

4.5.3 Pressure-Temperature Grids for Irradiated Atmospheres

The atmospheric temperature structure is an important input in the calculation of the transmission spectra. The self-consistent way to obtain the pressure-temperature (P-T) profile is to solve the radiative equilibrium equations simultaneously with the radiative transfer equations and hydrostatic equilibrium equations. The presence of molecules makes it more difficult to estimate the temperature structure as chemical equilibrium equations too need to be solved self-consistently. Further, for strongly irradiated exoplanets, the internal temperature is negligible compared to the temperature due to irradiation and the incident stellar flux at the top-most layer determines the atmospheric temperature structure as it interacts with the medium through absorption and scattering. Therefore, the atmospheric temperature at different depths is determined by the optical depth of the medium. At the same time, the optical depth is governed by the temperature structure making it an involved and complicated numerical procedure. For stars, brown dwarfs and self-luminous exoplanets with weak or negligible irradiation, the analytical formula for the P-T profile in Grey or "slightly" non-Grey atmosphere was derived by Chandrasekhar (1960). Analytical formalisms of temperature structure for non-Grey strongly irradiated planets are presented by Guillot (2010); Hansen (2008); Parmentier & Guillot (2014); Parmentier et al. (2015). In order to model the transmission spectra of close-in exoplanets, isothermal sP-T profiles with $T(P) = T_{eq}$ were adopted by Goyal et al. (2019); Kempton et al. (2017); Sing et al. (2016). The radially inwards incident radiation usually penetrates quite deep, about 10-100 bars pressure level. However, in the transit geometry considered for calculating the transmission spectrum, the atmosphere below approximately 1

bar pressure level is opaque because of the large path length that the radiation traverses. Therefore, a very small part of the overall atmosphere is probed in the transmission spectrum. So, isothermal approximation although not completely accurate, especially for hotter planets where temperature inversion due to the presence of TiO and VO becomes dominant, does not make much difference in the results for the comparatively cooler planets (Goyal et al., 2018) with current observations.

We have used the FORTRAN implementation of the analytical model for the $P-T$ profiles of non-Grey irradiated planets presented by Parmentier & Guillot (2014); Parmentier et al. (2015). This code available in public domain[5] uses the functional form for Rosseland opacity provided by Valencia et al. (2013) which is based on the Rosseland opacities of Freedman, Marley, & Lodders (2008). The analytical model takes into account the opacities both in the optical and in the infra-red region. The analytical models are compared with state-of-the-art numerical models and the different coefficients in the analytical models are calibrated for a wide range of surface gravity and equilibrium temperature.

4.5.4 Abundance, Opacity and Optical Depth

The abundance of different chemical species can also be obtained self-consistently by simultaneously solving the radiative equilibrium, hydrostatic equilibrium and chemical equilibrium equations. However, many groups have created databases for the opacities of different chemical species for a different choice of metallicity, pressure, temperature and C/O ratio (e.g. the `Exo-Transmit` code as explained in Section 4.4.1). At first, we developed some basic models with a few gases such as H_2, He, CO, H_2O, and CH_4. We kept the abundance of the species as free parameters and set uniform (independent of altitude) values for them as explained in Section 4.5.5. Later, we also modeled the atmosphere and the transmission spectra including 30 atomic (Na, K, He etc.) and molecular

[5] http://cdsarc.u-strasbg.fr/viz-bin/qcat?J/A+A/574/A35

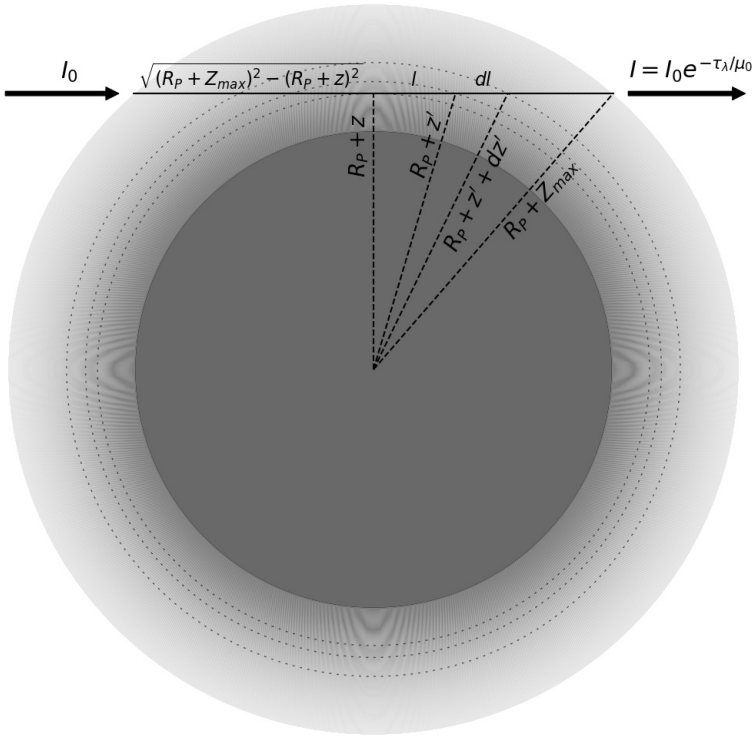

Figure 4.3: Transit geometry showing optical path along which light from the host star traverses through the planetary atmosphere to reach us during primary transit. It only shows one layer of the atmosphere along the optical path (along line-of-sight with respect to observer) at a distance $R_p + z$ from the center. A point on the path at a distance l from the mid-point of the path is at a distance $R_P + z'$ radially from the center of the planet.

species (H_2 , H_2O , CO_2 , CO, CH_4 , TiO, VO, SiO, C_2H_2, C_2H_4, etc.) using the EOS file of `Exo-Transmit` corresponding to solar metallicity.

To calculate the transmission flux using Equation 4.4 we need to calculate the optical depth following the transit geometry. We calculate the line-of-sight (LOS) optical depth at every hemispheric angle on the disc of the planet from the disc center. We only need to calculate the total extinction for our basic models and for that, we require the absorption and scattering coefficients. Calculation of the absorption coefficients, again, involves the computation of atomic and molecular absorption due to species like Na, K, H_2O , CO, CH4 etc. as well as collision-induced absorption (CIA) due to the pairs of the most abundant species like H2-H2, H2-He, He-He, etc. We first considered scattering only due to the atoms and molecules of the gases of the dominant species i.e.

H2, He etc. and hence applied Rayleigh theory to calculate the scattering coefficients (van de Hulst, 1957).

The atomic and molecular absorption and CIA are calculated from the cross-sections which are extracted as 3-D arrays over the grids of wavelength, pressure and temperature from the different databases available for atomic and molecular line-lists. We primarily use the opacity cross-section database available with the code `Exo-Transmit` (Kempton et al., 2017) which has been calculated from the HITRAN (Gordon et al., 2017) database of line lists. We have also used the cross-section database (personal communication) used in the code `TauREx` (Waldmann et al., 2015a,b) and compared the results for the testing of consistency. These cross-sections are calculated from the `Exomol` (Tennyson & Yurchenko, 2012; Tennyson et al., 2016) database of line lists. We assume the atmosphere to be stratified which means that the properties such as pressure, temperature, density, absorption and scattering coefficient etc., only vary with the altitude measured in the radially outward direction from the center of the planet. The absorption coefficients are calculated from the cross-sections for ith chemical species (absorber) by (Goody et al., 1989; Tinetti, Encrenaz, & Coustenis, 2013),

$$\kappa_i(\lambda, z) = \sigma_i(\lambda, z) \left(\frac{P(z)}{K_B T(z)} \right) X_i(z), \tag{4.12}$$

where we focus on a layer at an altitude (radially outward) z above R_P. $\kappa_i(\lambda, z)$ and $\sigma_i(\lambda, z)$ denote the absorption coefficient and absorption cross-section respectively at wavelength λ at that layer for the ith absorber with mass fraction $X_i(z)$. $P(z)$ and $T(z)$ denote the pressure and temperature at that layer and K_B is the Boltzmann constant. The total extinction coefficient ($\chi(\lambda, z)$) is the sum of all the absorption and scattering coefficients of all the chemical species.

Figure 4.3 shows the transit geometry for an optical path inside the atmosphere traversed by the stellar photons (along LOS) which is the chord shown in the figure. The distance between the center of the chord and the center of

the planet is $R_P + z$. The optical depth along that path can be expressed as (Goody et al., 1989; Tinetti, Encrenaz, & Coustenis, 2013),

$$\tau(\lambda, z) = 2 \int_0^{L(z)} \chi(\lambda, z') dl, \tag{4.13}$$

where L(z) denotes the half of the length of the chord and dl denotes the differential segment in the direction of the ray at a distance l along the chord from the center of the chord. The radial distance between that segement, dl and the center of the planet is $R_P + z'$. Thus we have,

$$l = \sqrt{(R_P + z')^2 - (R_P + z)^2}$$
$$dl = \frac{(R_P + z')dz'}{\sqrt{(R_P + z')^2 - (R_P + z)^2}}$$

Hence, Equation 4.13 becomes,

$$\tau(\lambda, z) = 2 \int_0^{Z_{max}} \chi(\lambda, z') \frac{(R_P + z')}{\sqrt{(R_P + z')^2 - (R_P + z)^2}} dz', \tag{4.14}$$

where Z_{max} denotes the altitude of the top of atmosphere above R_P .

In practice, we actually divide the atmosphere into several stratified layers and calculate the optical depth shown in Equation 4.14 by summing the discrete path segments multiplied by corresponding extinction coefficients.

4.5.5 Procedure and Results

We calculated the transmission depth for a Jupiter-sized exoplanet with $T_{eq} = 2700K$ and surface gravity g = 30 ms^{-2} transiting a solar-type star. We first calculated the spectra using the opacity database from the code `Exo-Transmit` following Equation 4.4 and compared the spectra with the spectra produced using the `TauREx` model (obtained by personal communication). The atmosphere was assumed to be dominated by H_2 and He with a mean molecular

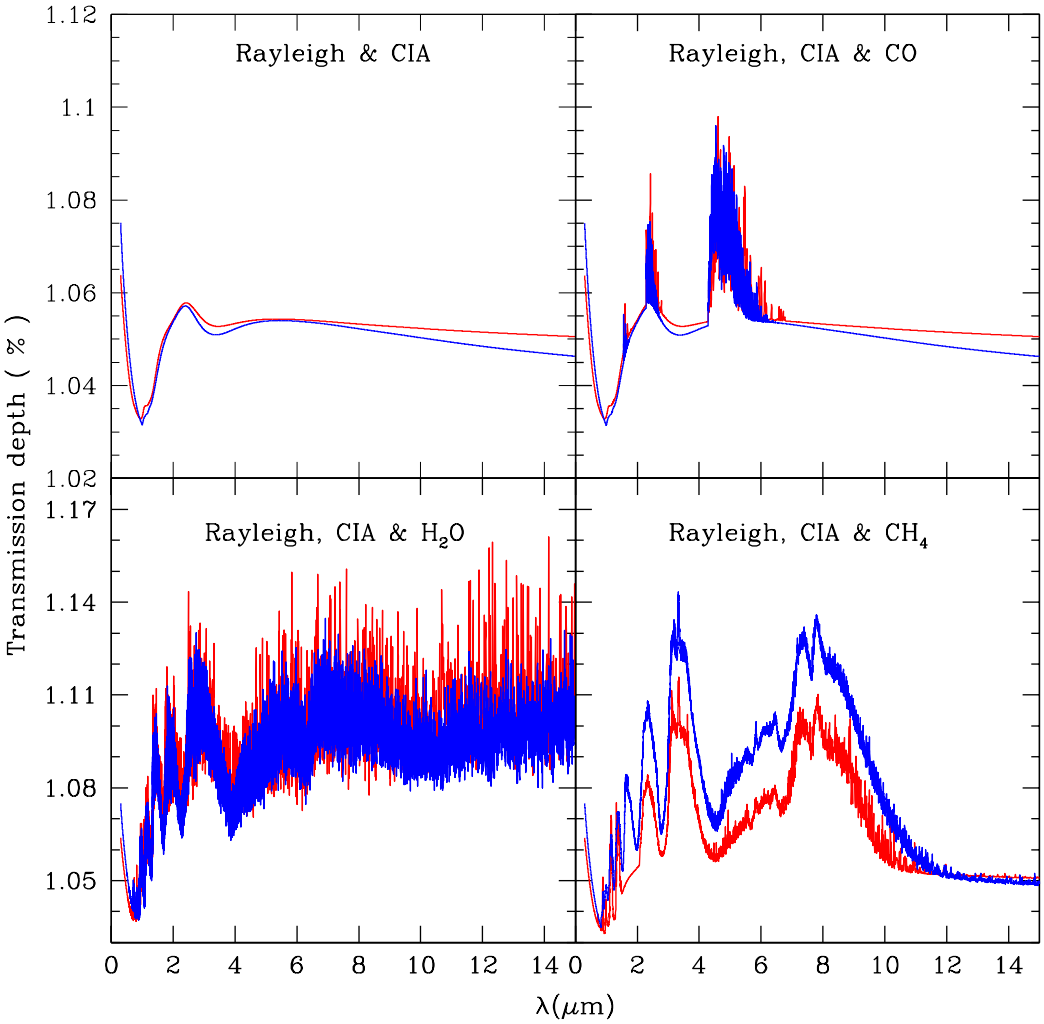

Figure 4.4: Comparison between the transmission depth calculated by us using the abundance and opacity databases provided with the code `Exo-Transmit` (in red) and that computed using the code `TauREx` (in blue). A Jupiter-size planet with $T_{eq} = 2700K$ and $g = 30ms^{-2}$ transiting a star with solar radius is considered in calculating the transmission depth.

weight of 2.29. The different conditions for which we calculated and compared are i) only Rayleigh scattering and CIA due to H_2 and He, ii) Rayleigh scattering and CIA due to H_2 and He, and absorption due to CO having a mass fraction of 10^{-4}, iii) Rayleigh scattering and CIA due to H_2 and He, and absorption due to H_2O having a mass fraction of 10^{-4}, and iv) Rayleigh scattering and CIA due to H_2 and He, and absorption due to CH_4 having a mass fraction

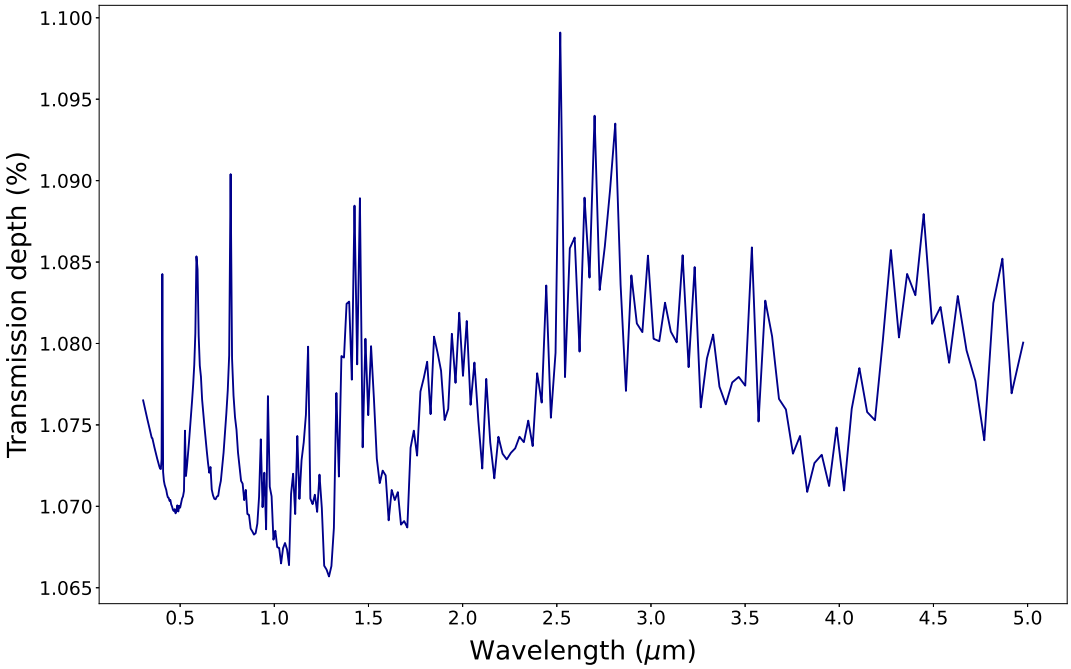

Figure 4.5: Transmission depth calculated by us for a Jupiter sized planet with T_{eq} =1500 K and g=30 ms^{-2} around a solar-type star considering 30 atomic (Na, K, He etc.) and molecular (H_2 , H_2O , CO_2 , CO, CH_4 , TiO, VO, SiO, C_2H_2, C_2H_4 etc.) species. We used the rain-out composition corresponding to solar metallicity and the absorption and scattering cross-sections of those species provided with the open-source code `Exo-Transmit` (Kempton et al., 2017).

of 10^{-4}. Figure 4.4 shows the corresponding transmission spectra.

Figure 4.5 shows the model of transit spectra of a Jupiter-sized planet with T_{eq} =1500 K and g = 30 ms^{-2} including 30 atomic and molecular species as explained in Section 4.5.4. It shows the contribution from the different chemical species to the transmission spectra of the hot Jupiters.

4.6 Conclusion

We started the high resolution transit spectroscopic observation with the motive of detecting traces of metals such as Na, K, Ca etc. in the atmospheres of the hot Jupiters, motivated by previous studies. However, we found that the SNR achieved with the 2m class telescope on a single observation is not enough to remark on the atmospheric contents conclusively. In fact, the achieved SNR shows that to detect an excess absorption due to Na of -50×10^{-5} (See Char-

bonneau et al. (2002); Redfield et al. (2008) for the convention) we would require ∼5 times more SNR which is equivalent to combining transit spectra of ∼25-30 of such events. On the other hand, we find that low resolution spectra have a low constraint on SNR requirement. In fact, low resolution spectra can be acquired in both the optical and IR region and can be modeled well with the current models of planetary atmospheres conveying more information about the atmospheres of the hot Jupiters. Hence, our future focus will be on the observation and modeling of low resolution transit spectra.

The basic models showed us that we had all the necessary tools and inputs for full-scale modeling of planetary atmospheres and the observed spectra. This study motivated us to develop complex atmospheric models by incorporating more physical processes for more accurate representations of the atmospheres of the hot Jupiters. The two aspects that we considered were the effect of the scattering albedo and the effect of the emission from the night-sides which are presented in Chapter 5 and Chapter 6 respectively. Moreover, the comparison between the two most popular models of atomic and molecular opacities shows that the correct choice of opacity database is a serious concern for the precise derivation of the planetary properties from the observed transit spectra from the current missions like HST etc. and the upcoming missions like JWST, ARIEL etc. This calls for more comparative studies between these models and the observed spectra.

Chapter 5

Detailed Modeling of Transmission Spectra in the Optical[1]

5.1 Introduction

A correct interpretation of the transmission spectra needs a comparison with a consistent theoretical model that incorporates all the physical and chemical processes in the planetary atmosphere. Theoretical models for transmission spectra of stars with transiting exoplanets having a wide range of equilibrium temperature and surface gravity have already been presented by several groups, as explained in 4.4. In all these models mentioned above, only the absorption of starlight passing through the planetary atmosphere is incorporated and thus the reduced intensity I due to the interaction of atoms and molecules in the atmosphere is calculated by using the Beer-Bouguer-Lambert law $I = I_0 e^{-\tau}$, where I_0 is the incident stellar intensity and τ is the line-of-sight optical depth of the medium that imprint the signature of the planetary atmosphere. In these models, although opacity due to scattering is added up to the opacity due to true absorption, angular distribution of the transmitting photon due to scat-

[1] *This chapter is also published in The Astrophysical Journal, Sengupta, Chakrabarty and Tinetti, vol. 889:181, 2020.*

tering is not incorporated. Since the scattering coefficient and hence the single scattering albedo at longer wavelengths, e.g., in infrared is extremely small or zero, this approximation is valid at wavelengths beyond the optical region. But it overestimates the transmission depth at shorter wavelength and hence does not provide correct results for optical region where scattering albedo is comparable to 1 and the diffused transmission and reflection due to scattering plays an important role in determining the radiation field. A correct treatment is thus to solve the multi-scattering radiative transfer equations for the diffused reflection and transmission as demonstrated by de Kok & Stam (2012) who presented three dimensional Monte Carlo simulation for Titan's atmosphere at wavelengths ranging between 2.0 and 2.8 μm and reported significant underestimation in the calculation of the transmission flux if forward scattering by haze and gas is neglected in the retrieval models.

We calculated the transmission depth as the solution of the detailed multiple-scattering radiative transfer equations for the atmosphere of exoplanets with a wide range of equilibrium temperature and surface gravity.

Today a few tens of gaseous exoplanet atmospheres have been probed in the optical and near-IR through transit observations with the Wide Field Camera 3 on board Hubble Space Telescope (Tsiaras et al., 2018). For a sub-sample of those, also optical spectra using the Space Telescope Imaging Spectrograph are available (Sing et al., 2016). This survey was complemented by photometric transit observations at two more longer wavelengths 3.6 μm and 4.5 μm by using the Spitzer Space Telescope Infrared Array Camera. Although one needs to be careful in combining data from multiple instruments (Yip et al., 2019), these observational data provide an excellent opportunity to understand the scope and limitations of various theoretical models.

We compared our model spectra with the existing theoretical models and with the observed HST and Spitzer data. In Section 5.2 we provide the formalisms for calculating the transmission depth. In Section 5.3 we discuss the model absorption and scattering opacity adopted in our present models. Sec-

tion 5.4 outlines the numerical method for solving the multiple scattering radiative transfer equations. The non-isothermal temperature-pressure profiles for non-Grey planetary atmosphere used in our models are described in Section 5.5. In Section 5.6 we present a simple haze model that is incorporated in order to include additional absorption and scattering opacities. The results are discussed in Section 5.8 followed by a specific conclusion in the last section.

5.2 The Transmission Depth

Although in many previous models, opacity due to scattering is added to the true absorption, scattering into and out of the ray is not explicitly considered before. This assumption is reasonable for calculating the transmission spectra at longer wavelengths, e.g., in the infrared region where the scattering albedo is negligible. But it grossly overestimates the transmission depth and hence does not provide correct results for the optical region where scattering albedo ω which is the ratio of the scattering coefficient to the extinction coefficient is non-zero and plays an important role in determining the radiation field. It's worth mentioning that ω depends on the wavelength as well as the atmospheric depth. A true treatment is thus to solve the multi-scattering radiative transfer equations for diffused reflection and transmission which for a plane-parallel geometry is given by e.g., Chandrasekhar (1960)

$$\mu \frac{dI(\tau_{LOS}, \mu, \lambda)}{d\tau_{LOS}} = I(\tau_{LOS}, \mu, \lambda) - \frac{\omega}{2} \int_{-1}^{1} p(\mu, \mu') I(\tau_{LOS}, \mu, \lambda) \mathrm{d}\mu' - \frac{\omega}{4} F e^{-\tau_{LOS}/\mu_0} p(\mu, \mu_0) \quad (5.1)$$

where $I(\tau_{LOS}, \mu, \lambda)$ is the specific intensity of the diffused radiation field along the direction $\mu = \cos\theta$, θ being the angle between the axis of symmetry and the ray path, F is the incident stellar flux in the direction $-\mu_0$, ω is the albedo for single scattering, $p(\mu, \mu')$ is the scattering phase function that describes the angular distribution of the photon before and after scattering and τ_{LOS} is the

optical depth along the line of sight expressed in 4.5.4.

The scattering phase function depends on the nature of scatterers. For scattering by non-relativistic electrons (Thomson scattering) and by atoms and molecules, the angular distribution is described by Rayleigh scattering phase function and is given by (Chandrasekhar, 1960)

$$p(\mu, mu') = \frac{3}{4}[1 + \mu^2\mu'^2 + \frac{1}{2}(1 - \mu^2)(1 - \mu'^2)], \tag{5.2}$$

where μ' and μ are the cosines of the angle before and after scattering with respect to the normal.

A beam of radiation traversing in a medium gets weakened by its interaction with matter by an amount $\mathrm{d}I_\nu = -k_\nu \rho I_\nu \mathrm{d}s = -I_\nu \mathrm{d}\tau_{LOS}$ where ρ is the density of the medium and κ_ν is the mass absorption co-efficient. Integration of this expression yields into the Beer-Bouguer-Lambert law. As pointed out by Chandrasekhar (1960), while passing through a medium, this reduction in intensity suffered by a beam of radiation is not necessarily lost to the radiation field. A fraction of the energy lost from an incident beam would reappear in other directions due to scattering and the remaining part would have been truly absorbed in the sense that it may get transformed into other forms of energy or of radiation of different frequencies. For a scattering atmosphere, the scattered radiation from all other directions contribute to the emission coefficients into the beam of the direction considered.

In a scattering medium, the radiation field has two components: the reflected and the transmitted intensities which suffer one or more scattering processes and the directly transmitted flux $\pi F e^{-\tau/\mu_0}$ in the direction $-\mu_0$. So, the reflected and the transmitted intensities that is incorporated through the second term in the right-hand side of Equation 5 does not include the directly transmitted flux which is described by the third term. In other words, the reduced incident radiation $\pi F e^{-\tau/\mu_0}$ which penetrates to the atmospheric level τ without suffering any scattering is different than the diffuse radiation field

$I(\tau, \mu)$ which has arisen because of one or more scattering processes. Therefore, in the absence of scattering, i.e., when $\omega = 0$, the emergent intensity obtained by integrating Equation 5 reduces to that given by Beer-Bouguer-Lambert law. As a consequence, in the infra-red wavelength region where the scattering albedo is negligibly small or zero, use of Beer-Bouguer-Lambert law $I = I_0 e^{-\tau}$ in calculating the transmission depth is appropriate.

The solution of the above radiative transfer equation provides the intensity along the direction μ of the stellar radiation that passes through the planetary atmosphere. The reduced stellar flux F_P that emerges out of the planetary atmosphere is obtained by integrating the intensity in each beam of radiation, over the solid angle subtended by the atmosphere.

5.3 The Absorption and Scattering Opacity

The main aim of this work was to calculate the transmission spectra appropriate in the optical wavelength region. We did not intend to investigate the chemistry under different conditions of the atmosphere. Therefore we developed models with a fixed metallicity - solar metallicity and solar system abundances for the atoms and molecules in the planetary atmosphere. We calculated the gas absorption and scattering coefficients by adopting the corresponding cross-section values provided with the package `Exo-Transmit` (described in Section 4.4.1). Using `Exo-Transmit` package we calculated the total extinction coefficients (true absorption plus scattering) as well as the scattering coefficients for a given $P-T$ profile and surface gravity. The calculation of the coefficients is explained in Section 4.5.4. The albedo for single scattering at each wavelength and each pressure point is calculated by taking the ratio of the scattering coefficient to the extinction coefficient. We have incorporated all the species provided in the package and their EOS for solar metallicity without any change. The EOS for Rain-out condensation are adopted in all the calculations.

Finally, we have not included cloud opacity or additional scattering sources

in our use from the `Exo-Transmit` package. We have incorporated haze in our radiative transfer code and we discuss the cloud model in section 5.6.

5.4 Numerical Method to Solve the Radiative Transfer Equations

We use the absorption and scattering coefficients at different pressure levels in the planetary atmosphere and calculate the line of sight optical depth as given in Equation 6. The wavelength-dependent albedo for single scattering ω at different pressure levels is the ratio between the scattering coefficients $\sigma(\lambda)$ and the extinction co-efficient $\chi(\lambda)$. We solve the multiple scattering radiative transfer equation as given in Equation 5 by using discrete space theory developed by Peraiah & Grant (1973). The numerical code is extensively used to solve the vector radiative transfer equations in order to calculate polarized spectra of cloudy brown dwarfs and self-luminous exoplanets (Marley & Sengupta, 2011; Sengupta, 2018; Sengupta & Marley, 2009, 2010, 2016). For this work, we have used the scalar version of the same numerical code.

In this method we adopt the following steps :

1. The medium is divided into a number of "cells" whose thickness is defined by τ. The thickness of each cell is less than a critical optical thickness τ_c which is determined on the basis of the physical characteristics of the medium.

2. The integration of the radiative transfer equation is performed on the cell which is bounded by a two-dimensional grids $[\tau_n, \tau_{n+1}] \times [\mu_{j-1/2}, \mu_{j+1/2}]$.

3. These discrete equations are compared with the canonical equations of the interaction principle and the transmission and reflection operators of cells are obtained.

4. Lastly, all the cells are combined by the "star" algorithm and the radiation field is obtained.

A detailed description of the numerical method can be found in Peraiah & Grant (1973); Sengupta & Marley (2009).

Using 2.5 GHz Intel Core i5 processor with 8 GB RAM, it takes typically 10-12 minutes for one complete run of the FORTRAN version of the code that calculates the transmission spectra for wavelength ranging from 0.3-30 μm with a total number of 4616 wavelength points. We have also developed a Python version of the code which provides the same results in a shorter time.

In order to validate the numerical method as well as the molecular and atomic opacity used in the present work, we present in Figure 5.1 a comparison of our model spectrum with a model by Stephens et al. (2009) for a cloud-free methane-dwarf (T8) and with the observed Spex prism spectrum (Burgasser et al., 2004) of the T-dwarf 2MASSI J0415-0935. We also compare our model spectrum with the model presented by Fortney et al. (2008) for a self-luminous directly imaged Jupiter-type exoplanets with $T_{eff} = 600$K and surface gravity $g = 30\text{ms}^{-2}$. The comparison is presented in Figure 5.2. The model spectra and the pressure-temperature profiles for both the cases have kindly been provided by M. Marley (private communication).

The slight miss-match of our synthetic spectrum with that of Stephens et al. (2009) at the infra-red region of the T-dwarf, as presented in Figure 5.1, is due to the disagreement in the opacity of methane as detected while comparing the model transmission depth derived by using Exo-Transmit and Tau-REx. The difference may also be attributed to different elemental abundances adopted. It is worth mentioning here that for the case of self-luminous exoplanets, the model spectrum of Fortney et al. (2008) incorporates condensate clouds in the visible atmosphere while we have considered a cloud-free atmosphere.

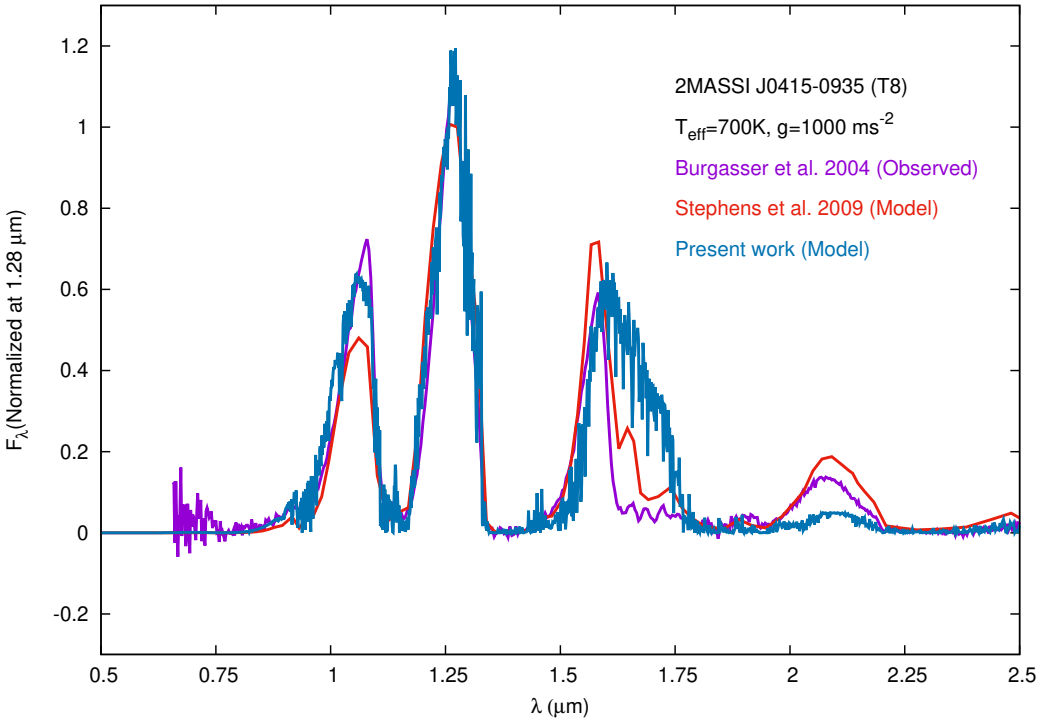

Figure 5.1: Comparison of model spectra with the observed Spex prism spectrum of a cloud-free brown dwarf (T8) 2MASSI J0415-0935.

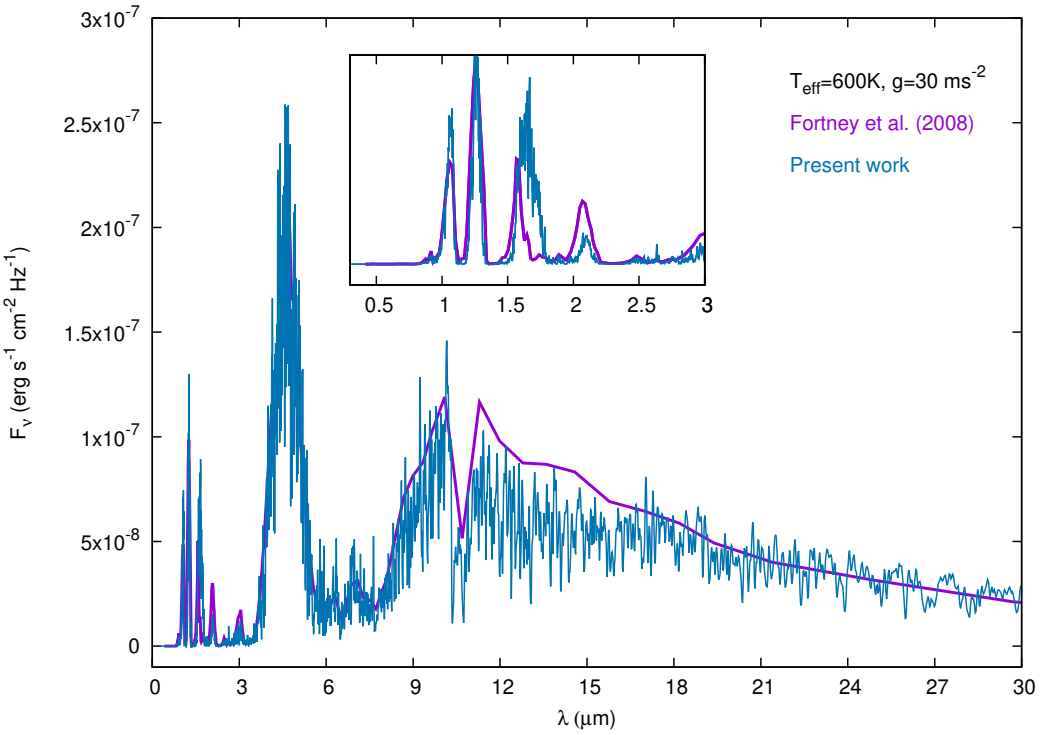

Figure 5.2: Comparison of model spectra for a self-luminous giant exoplanet

5.5 The Pressure-Temperature Profiles for Irradiated Exoplanets

The atmospheric temperature structure is an important input in the calculation of the transmission spectra. We have used the FORTRAN implementation of the analytical model for the $P-T$ profiles of non-Grey irradiated planets presented by Parmentier & Guillot (2014); Parmentier et al. (2015) as explained in Section 4.5.3

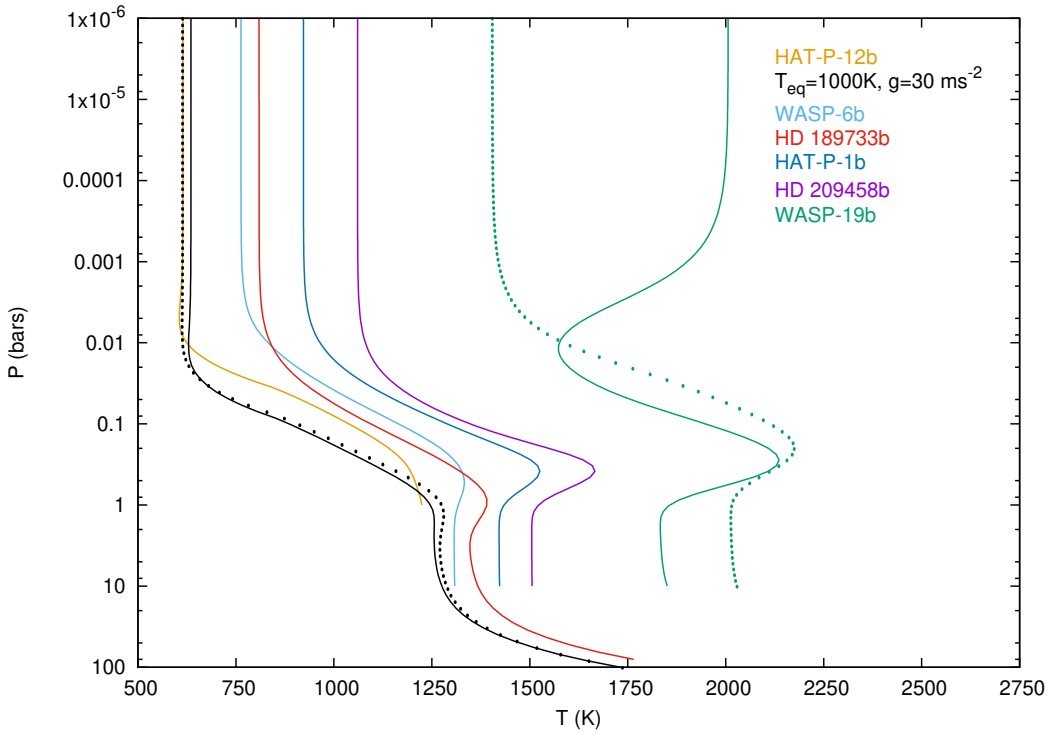

Figure 5.3: Pressure-Temperature ($P-T$) profiles of hot-Jupiters derived from the analytical formalisms presented by Parmentier et al. (2015). Dotted lines represent the corresponding $P-T$ profiles without the presence of TiO and VO in the atmosphere. T_{eq} and g used for each planet are listed in Table 1.

In Figure 5.3 we present the $P-T$ profiles derived by using the above-mentioned computer code for a number of exoplanets with a wide range of surface gravity g and equilibrium temperature T_{eq}. The values of g and T_{eq} for various exoplanets are given in Table 5.1. We considered a planet-averaged (see Parmentier & Guillot (2014); Parmentier et al. (2015)) thermal profile with

Table 5.1: Best fit parameters for the model transmission spectra in the infrared region of six exoplanets

Name	T_{eq} (K)	g (ms^{-2})	$R_P(R_J)$	$R_*(R_\odot)$	n_0	d_0 (μm)
WASP-19b	2050	14.2	1.34	1.01	0.0	0.0
HD 209458	1448	9.4	1.38	1.2	5×10^4	0.4
HAT-P-1b	1320	7.5	1.33	1.195	3×10^4	0.4
HD 189733	1200	21.4	1.19	0.8	2×10^5	0.4
HAT-P-12b	960	5.6	0.9	0.71	1×10^6	0.2
WASP-6b	1150	8.7	1.18	0.87	2×10^5	0.4

flux parameter, f = 0.25. Solar flux is assumed in the calculations. We have not considered a convective zone at the bottom of the models as such a zone should be situated much below the pressure level corresponding to R_P.

We have included the effect of TiO and VO on the $P - T$ profile. As shown in Figure 5.3, the effect is not significant for planets with $T_{eq} \leq 1000$K. However, as T_{eq} increases, the atmospheric temperature increases significantly in the upper atmosphere due to the presence of TiO and VO in the atmosphere. For a planet as hot as WASP-19b (T_{eq}=2050K), the presence of TiO and VO introduces temperature inversion which disappears in the absence of TiO and VO. It's worth mentioning here that in the absence of internal energy of the planet, the $P-T$ profile is used only to calculate the absorption and scattering coefficients. The radiation field is determined by the incident stellar flux at the uppermost boundary.

5.6 Additional Absorption and Scattering due to Atmospheric Cloud/Haze

Condensation clouds may play important roles in shaping the transmission spectra of hot-Jupiters (Fortney et al., 2010; Sing et al., 2016). Under the appropriate combination of temperature and surface gravity and based on the chemical equilibrium process, cloud or haze may form in the visible region of the planetary atmosphere (Sudarsky, Burrows, & Hubeny, 2003). It is well-known

that the optical spectra of hotter L-brown dwarfs are shaped by the presence of condensation cloud (Cushing et al., 2008) while in comparatively cooler T-brown dwarfs, the cloud gets rained down below the visible atmosphere. Detail models of cloud and haze under chemical equilibrium in exo-planetary atmospheres have been presented by Ackerman & Marley (2001); Burrows, Budaj, & Hubeny (2008); Cooper et al. (2003).

In this work, we have considered a simple model for thin haze in the uppermost atmosphere following the approach of Griffith, Yelle, & Marley (1998); Saumon et al. (2000). In this model the dust absorption and scattering cross-sections as well as the scattering phase functions are calculated with the Mie theory of scattering (Bohren & Huffman, 1983). The cloud is confined within a thin region of the atmosphere bound by a base and deck. The vertical density distribution of the cloud particle is given by

$$n(P) = n_0 \frac{P}{P_0}, \tag{5.3}$$

where $n(P)$ is the number density of dust particle, P is the ambient pressure, P_0 is the pressure at the base radius R_P and n_0 is a free parameter with the dimension of number density. The deck of the haze is fixed at 0.1 Pa pressure level and the base is located at 1.5-2.5 Pa. A log-normal size distribution of the dust particles given by

$$f(d) = \frac{d}{d_0} \times \exp\left[\frac{\ln(d/d_0)}{\ln \sigma}\right]^2 \tag{5.4}$$

where d is the diameter of the dust particle, d_0 is the median diameter in the distribution and σ is the standard deviation. Without loss of generality, in the present model, we fix $\sigma = 1.3$ and the fraction of the maximum amplitude of the distribution function at which we set the cutoff of the distribution is taken to be 0.02. We have used the wavelength-dependent real and imaginary parts of the refractive index for amorphous Forsterite (Mg_2SiO_4) which is believed to be the dominant constituent of the atmospheric cloud.

It must be emphasized that although cloud or haze may play crucial role in determining the transmission as well as the emission spectra of hot-Jupiters, it is not necessary that the atmosphere of all hot-Jupiters should have clouds in the visible atmosphere. For low surface gravity and strong irradiation, clouds may evaporate from the atmosphere. On the other hand, for high surface gravity and low temperature, clouds may rain down below the visible region. The absence of alkaline and water absorption features in the transmission spectra of many hot-Jupiters is usually interpreted as the presence of clouds. The whole purpose of this work is to invoke additional absorption and scattering opacities in the form of condensates and investigate how the optical spectra are affected by dust (Mie) scattering over Rayleigh scattering. In future we shall incorporate more complicated and self-consistent cloud models.

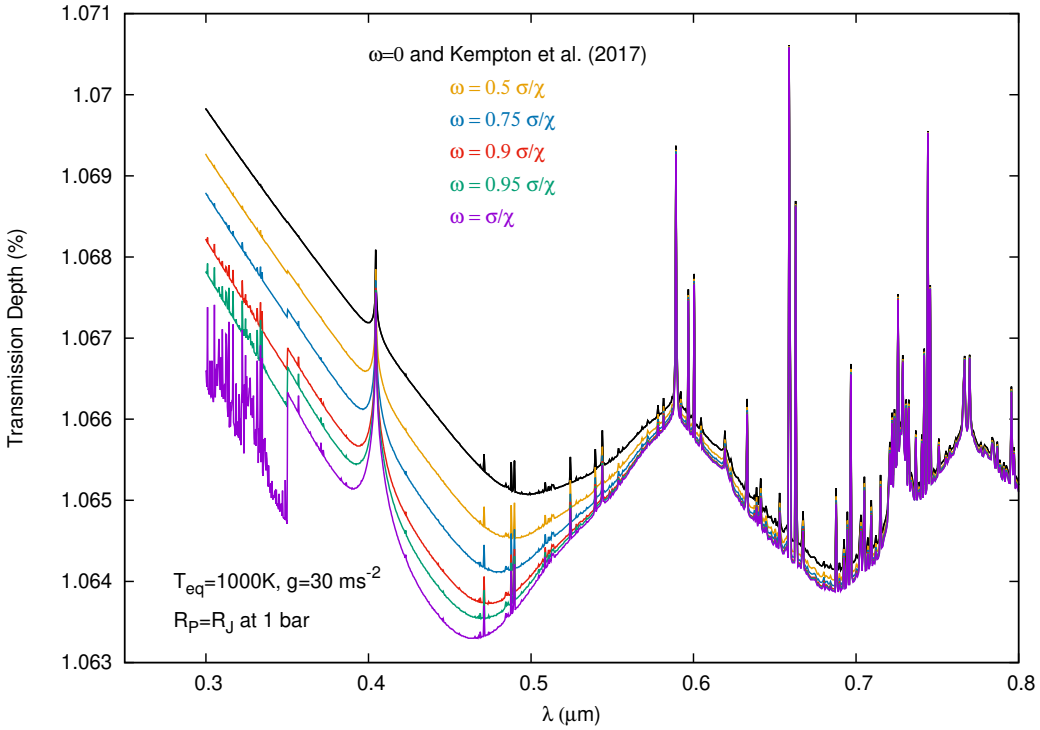

Figure 5.4: Transmission depth of a hot-Jupiter for different values of the scattering albedo $\omega = \sigma/\kappa$. The optical depth is unaltered for all cases. The model by Kempton et al. (2017) adopts Beer-Bouguer-Lambert law $I = I_0 e^{-\tau}$ which overlaps with the present model when ω is set at zero. All of our models use the solution of the radiative transfer equations.

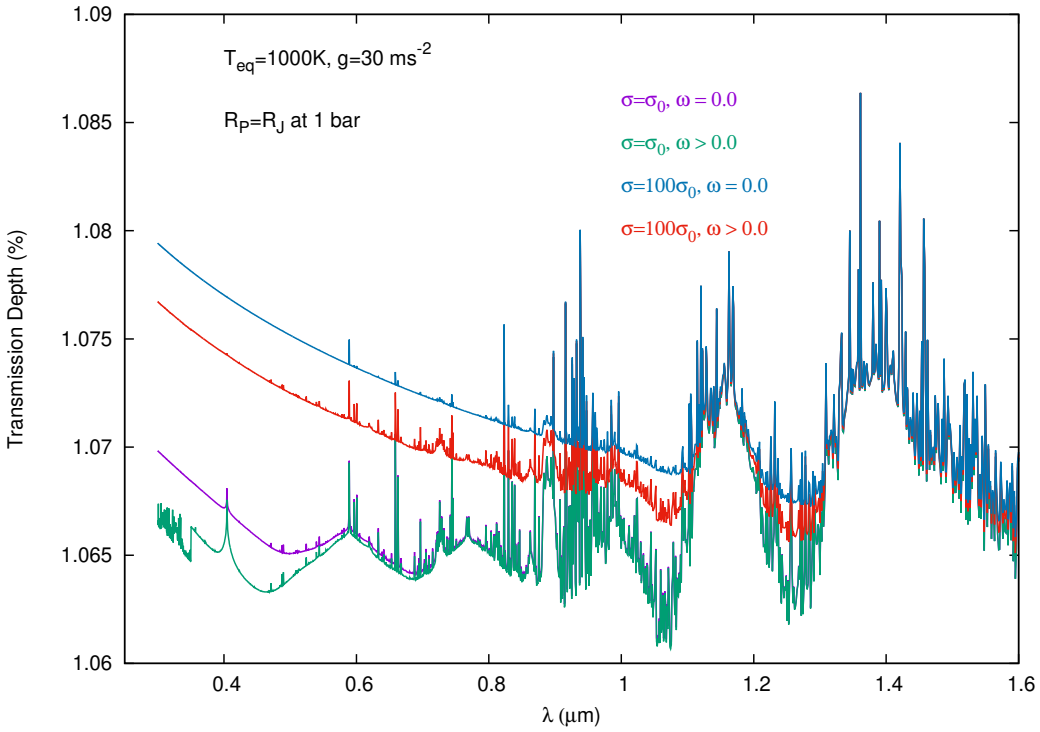

Figure 5.5: Comparison of transmission spectra with increased scattering opacity for zero and non-zero albedo. σ_0 is the actual opacity due to Rayleigh scattering derived by using solar system abundances. ω is the corresponding scattering albedo. The absorption co-efficients at all wavelengths are kept unaltered.

5.7 Results and Discussions

We have shown the results for wavelength region ranging from near optical to infrared. Figure 5.4 shows the difference in the transmission depth calculated by solving the multiple scattering radiative transfer equations and by using Beer-Bouguer-Lambert law. The transmission depth presented by the model of Kempton et al. (2017) using Beer-Bouguer-Lambert law overlaps at all wavelengths with that of our model when $\omega = 0$. Note that the opacity due to scattering is, however, included in the calculations of the optical depth.

Considering a Jupiter-type exoplanet with $T_{eq} = 1000$K and surface gravity $g = 30\text{ms}^{-2}$, we investigate the effect of scattering albedo by increasing its value while unaltering the optical depth due to scattering. Figure 5.4 shows that with the increase in the scattering albedo ω, the amount of diffuse radia-

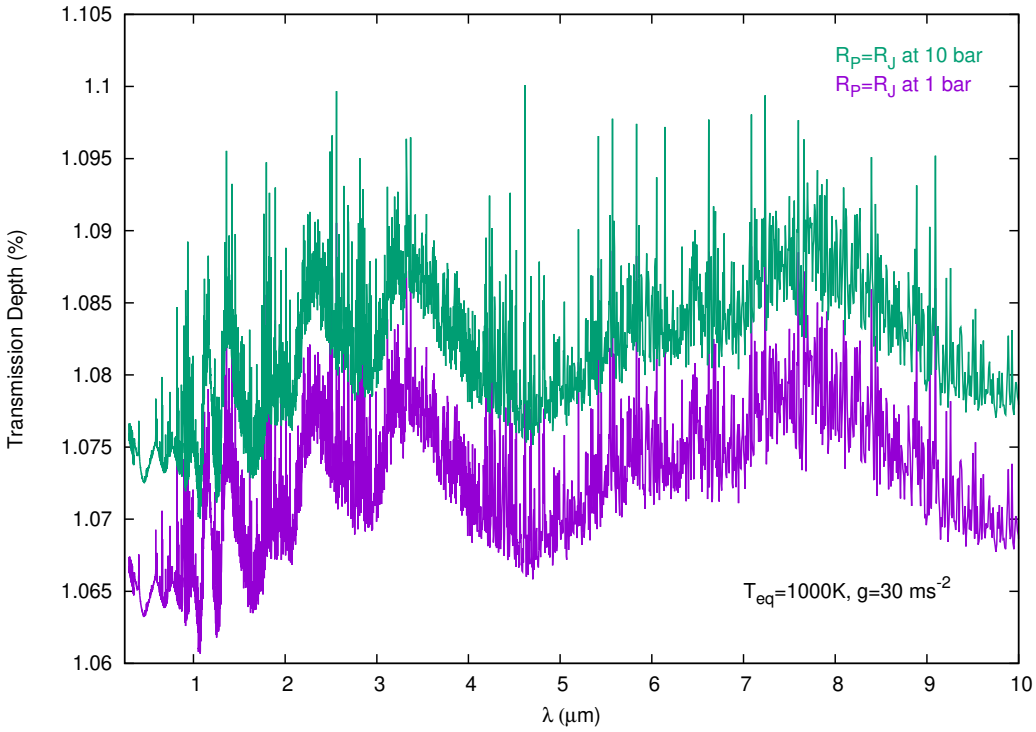

Figure 5.6: Comparison of transmission spectra with the base radius R_P located at different pressure levels.

tion due to scattering increases. Part of this diffuse radiation is added to the reduced stellar light that transmit the planetary atmosphere. Consequently, the transmitted flux increases amounting to a decrease in the transmission depth. However, at wavelengths longer than about 0.6 μm, the Rayleigh scattering albedo becomes negligibly small and therefore the transmission spectra coincide to that without scattering. Hence, Figure 5.4 demonstrates that scattering plays an important role in determining the optical transmission spectra. Clearly, scattering contributes in two ways - (1) the opacity due to scattering adds up to the opacity due to pure absorption and hence increases the total optical depth which reduces the transmitted stellar flux and (2) increases the transmitted stellar flux by adding the diffuse radiation due to scattering to the outgoing stellar flux. The net effect yields into a decrease in the transmission depth as shown in Figure 5.4. However, at about 0.35μm, we notice a sudden rise in the transmission depth which remains unexplained. The effect of scattering becomes negligible at wavelengths longer than about 0.7μm where the

opacity due to scattering also becomes negligible. This is also demonstrated in Figure 5.5. However, with the increase in the scattering coefficients, the effect of scattering albedo is significant even in the near-infrared.

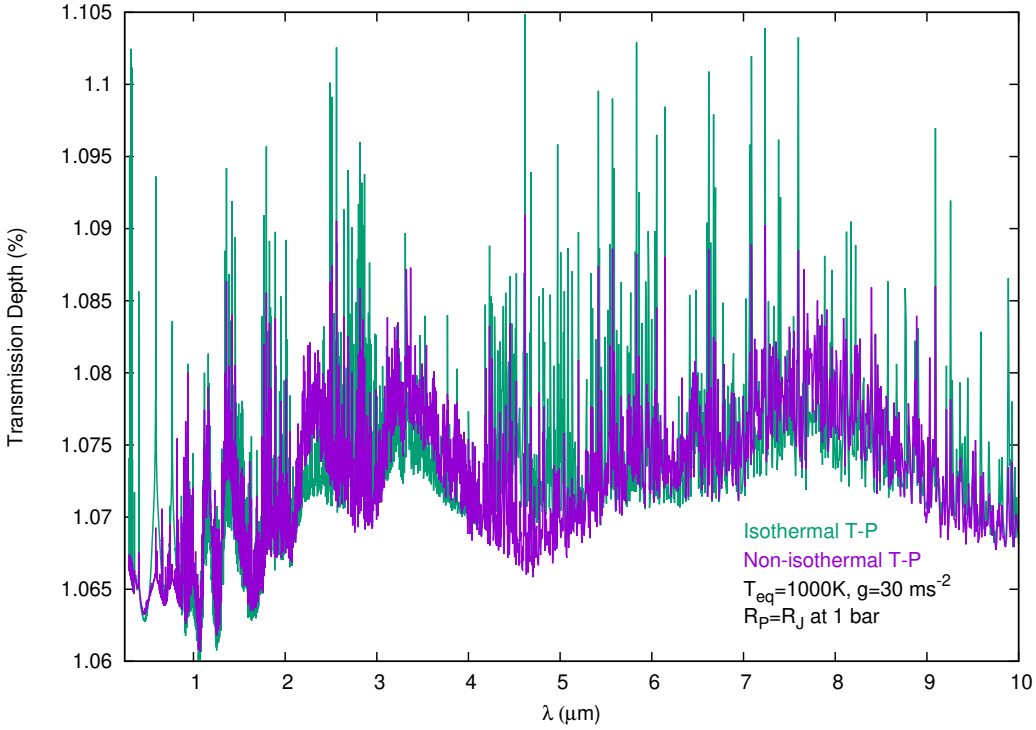

Figure 5.7: Comparison of transmission spectra with isothermal and non-isothermal temperature-pressure profile. For isorthermal case, the temperature is taken to be equal to T_{eq} at all pressure points.

Figure 5.6 demonstrates that the transmission depth increases if the stellar flux passes through the deeper region of the atmosphere. If we consider that the planetary atmosphere through which the stellar flux is transmitted is extended up to a pressure level of 10 bar instead of 1 bar, the transmission depth increases by an amount given in Equation 3. Note that, in that case, both the first and the second terms in the right-hand side of Equation 3 should affect the transmission depth. However, Figure 5.6 shows a constant difference in the transmission depth even up to 10 μm implying that the change in the atmospheric radius R_{PA} plays a dominant role over the change in the transmitted flux. However, as mentioned in Section 5.5, because of the transit geometry considered for calculating the transmission spectrum, the atmosphere below

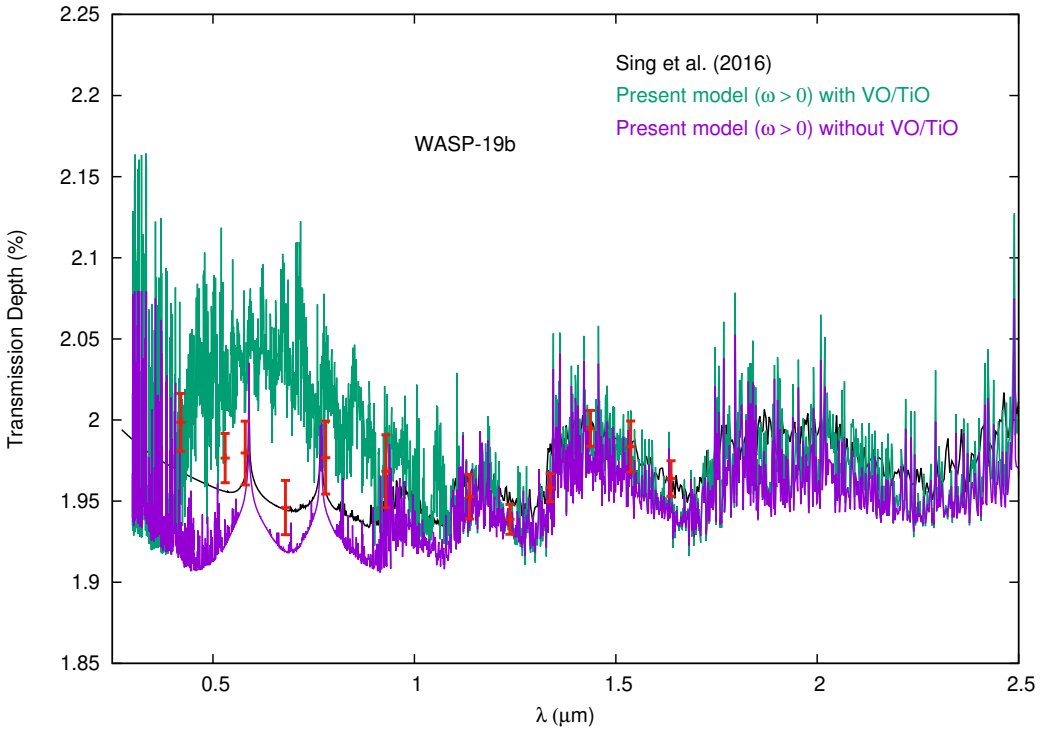

Figure 5.8: Comparison of model transmission spectra with and without the presence of VO and TiO and with the observed data (red) for WASP-19b.

approximately 1 bar pressure level is sufficiently opaque to the transmitted stellar radiation. Therefore, in all models, we calculate R_{PA} at 1 bar pressure level of the planetary atmosphere.

Similarly, Figure 5.7 shows that the transmission spectra do not differ significantly if an isothermal pressure-temperature profile is considered instead of non-isothermal temperature-pressure profile derived through detail numerical procedure. However, as Figure 5.3 implies, the isothermal approximation is reasonable only if the planet is not strongly irradiated. For planets with equilibrium temperature higher than about 1400K, presence of TiO/VO introduces significant inversion in the temperature and therefore even at the upper layer of the atmosphere isothermal approximation may not be appropriate. Therefore, in order to calculate the transmission spectra in the optical region, accurate non-isothermal temperature-pressure profiles are needed to be used for relatively hotter planets.

Using non-isothermal temperature-pressure profiles, we calculated the ab-

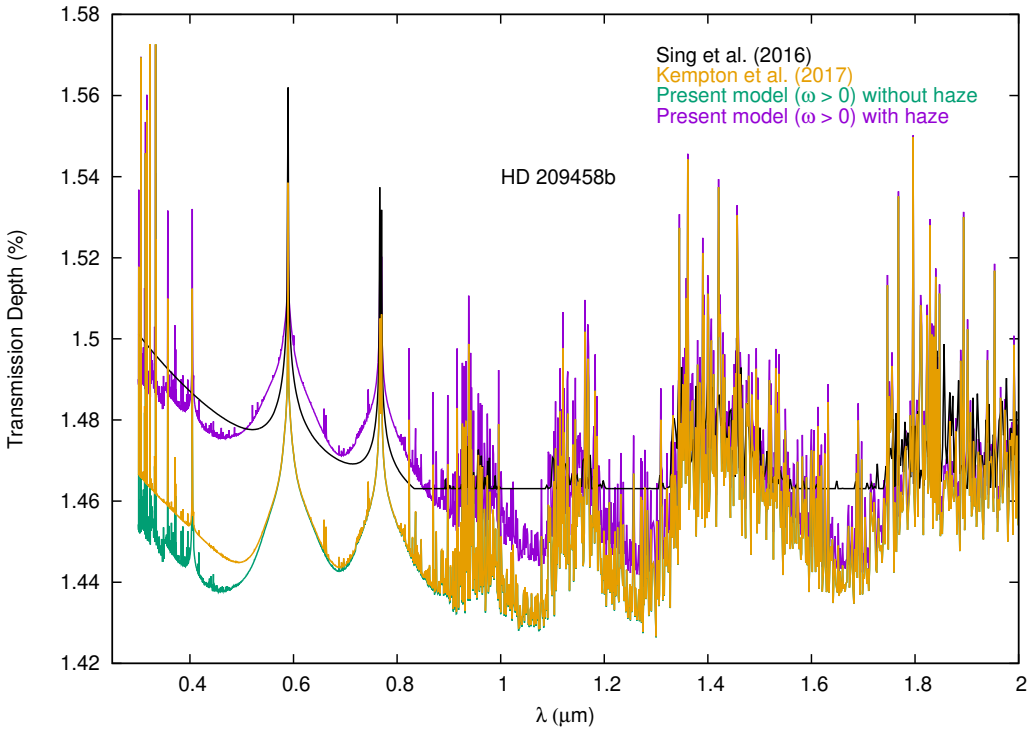

Figure 5.9: Comparison of model transmission spectra with and without the effect of Rayleigh scattering albedo and that by haze for exoplanet HD 209458b.

sorption and scattering coefficients and then the transmission depth is calculated by solving multiple scattering radiative transfer equations for plane-parallel stratification of the planetary atmosphere. We compare our model spectra for a few hot-Jupiters with the existing model spectra and observed data presented by Sing et al. (2016). The model spectra of Sing et al. (2016) and the observed data are available in public domain[2]. The detail about these model grids and about the observed data are described in Sing et al. (2016). The various physical parameters adopted in order to obtain the best fit (by eye) at the infra-red region where scattering is negligible are listed in Table 1.

In order to explain the high transmission depth in the optical, Sing et al. (2016) incorporated additional Rayleigh scattering opacity by increasing the scattering cross-section of hydrogen molecules 10 to 1000 times its value at 350 nm.. However, as can be seen in Figure 5.8, the present model for the exoplanet WASP-19b yields much higher transmission depth at optical region

[2]https : //pages.jh.edu/ dsing3/David$_S$ing/Spectral$_L$ibrary.html

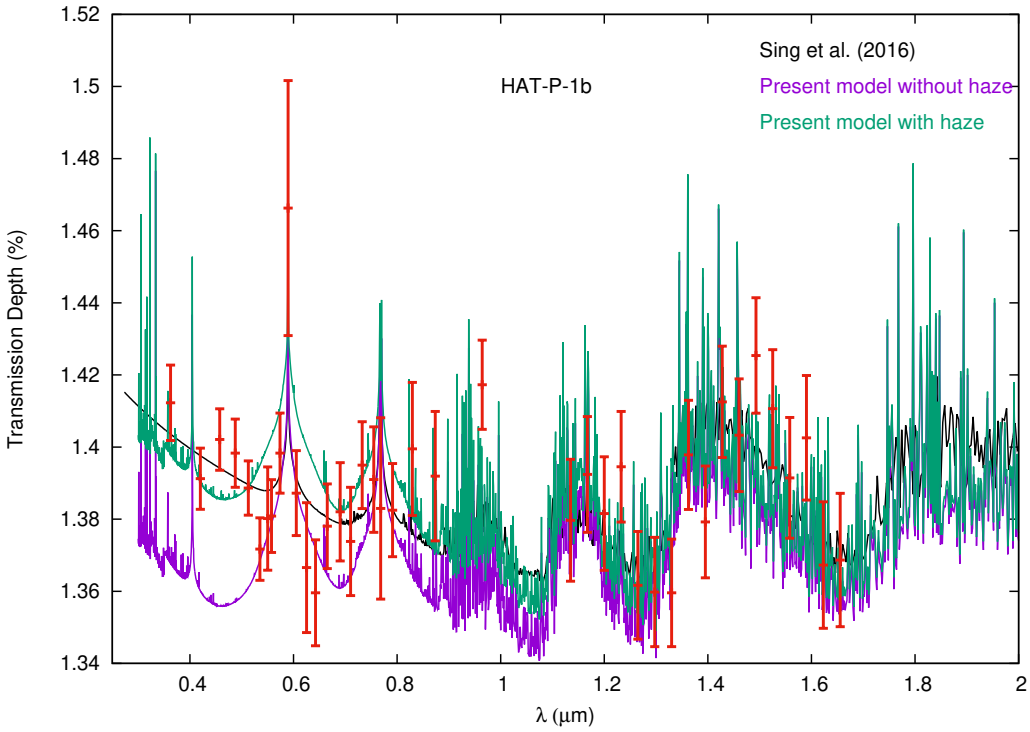

Figure 5.10: Comparison of model transmission spectra with and without the effect of haze and with the observed data (red) for HAT-P-1b.

up to 1.0 μm than that presented by Sing et al. (2016). We have not included any additional opacity source for this model. This difference is attributed to the presence of TiO and VO. In the absence of TiO and VO, the transmission depth profile qualitatively matches well with the model by Sing et al. (2016). However, since diffusion by scattering reduces the transmission depth, the two models do not overlaps. The two models, however, match at wavelengths longer than 1.0 μm where the scattering is negligible..

As mentioned before, the formation of clouds in the planetary atmosphere needs an appropriate combination of temperature and surface gravity. Strong irradiation or strong thermal radiation can cause evaporation of the cloud while low temperature and high surface gravity may cause rain out of the condensates. The disappearance of atomic and molecular absorption lines in the optical is usually interpreted as the evidence of cloud or haze. However, for planetary atmosphere that has no or negligible thermal radiation, scattering by cloud may alter the absorption features in the transmission spectra. The presence of

cloud or haze not only changes the total opacity of the atmosphere, but it also alters the scattering albedo of the medium.

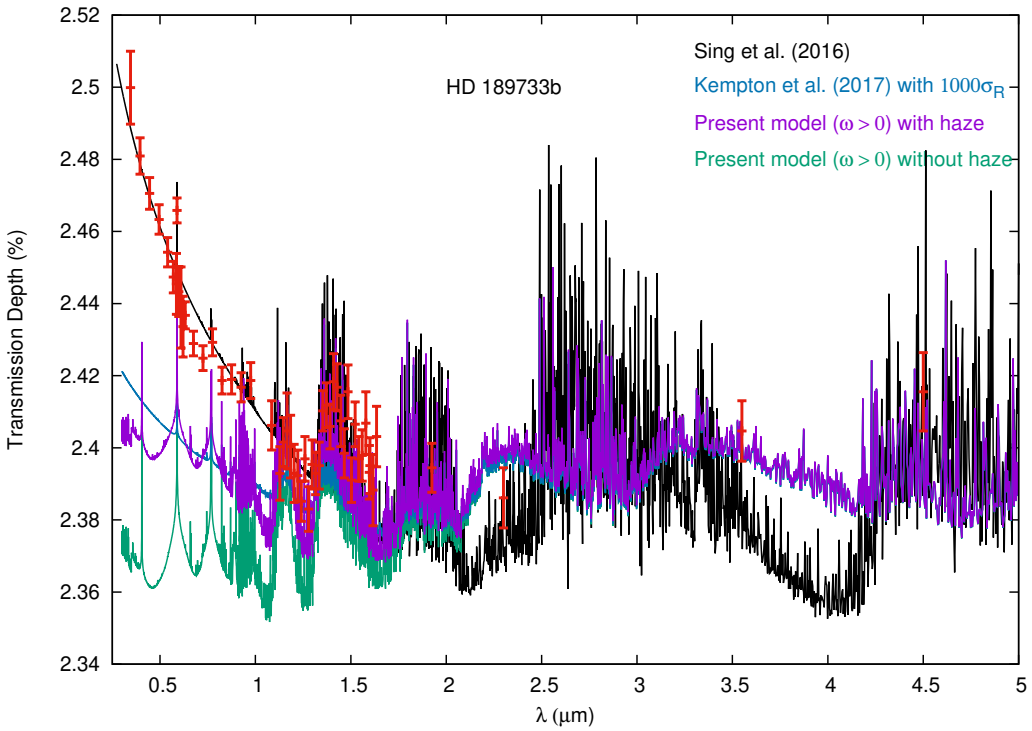

Figure 5.11: Comparison of observed data (red) and model transmission spectra for HD 189733b with and without haze in the upper atmosphere.

For all models except that of WASP-19b, we have included a thin haze in the upper atmosphere as described in section 5.6. In Figure 5.9, we present a comparison of the transmission spectra for HD 209458b with and without haze. We also present in the same figure the transmission spectra obtained with $\omega = 0$. For both the cases - with zero and non-zero albedo, the total extinction i.e., the opacity due to true absorption as well as scattering is kept unchanged. With the inclusion of haze, the extinction increases yielding into higher optical depth at the upper atmosphere. The scattering albedo also changes due to cloud particles. Figure 5.9 shows that the transmission depth calculated with or without Rayleigh scattering albedo is much lower than that presented by Sing et al. (2016). But a reasonably good match with the model by Sing et al. (2016) in the optical is obtained by the inclusion of haze. The model spectra with and without haze converge at wavelengths longer than 1.3

μm. For this case, we have not presented the observed data as it fits with the model by Sing et al. (2016) which fits the observed data in the optical.

Similarly, we have obtained a reasonably good match with the model by Sing et al. (2016) as well as with the observed data for HAT-P-1b by invoking haze in the planetary atmosphere. A comparison is presented in Figure 5.10. The transmission depth calculated without haze is significantly less than that calculated with haze. Note that in both cases, the effect of scattering albedo is included. All the model spectra, however, converge at wavelengths longer than about 1.3 μm where scattering becomes negligible..

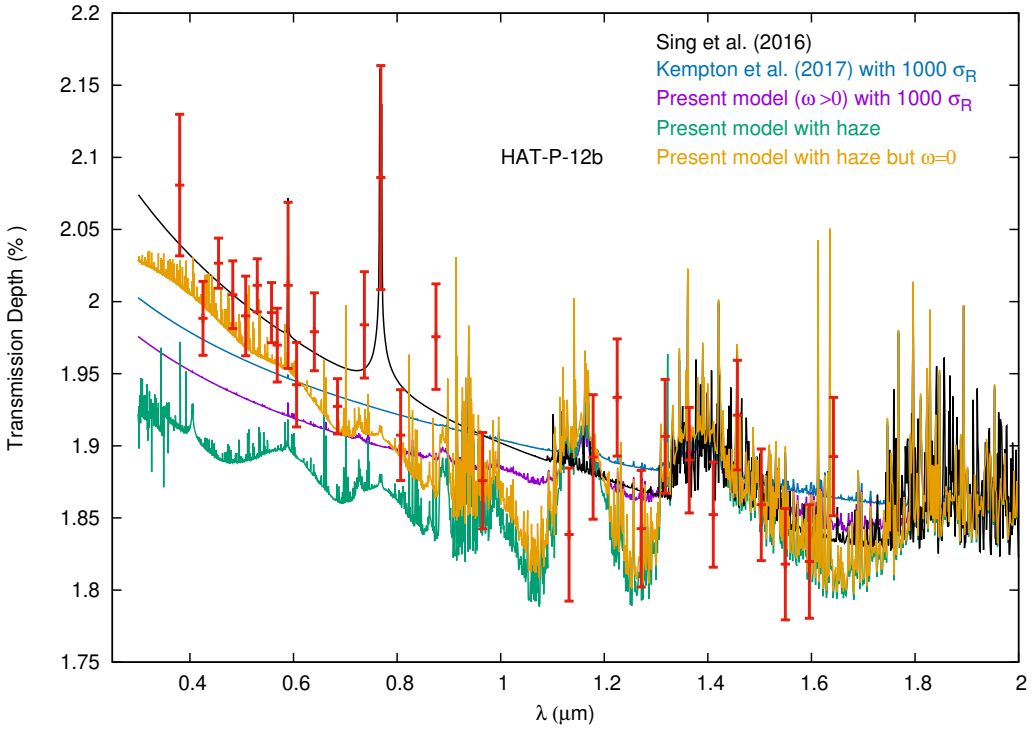

Figure 5.12: Comparison of observed data (red) and model transmission spectra for HATP-P-12b with and without haze in the upper atmosphere. The model transmission spectrum of Kempton et al. (2017) with thousand times of the actual scattering co-efficient is also presented for comparison. Further, an atmospheric model with absorption by haze but without the effect of scattering albedo is presented in this figure.

The sharp increase in the values of observed transmission depth for HD 189733b and HAT-P-12b at wavelengths shorter than 1.0 μm however do not fit our model transmission spectra even by increasing the scattering opacity a thousand times or by incorporating haze. Figure 5.11, however, demonstrates

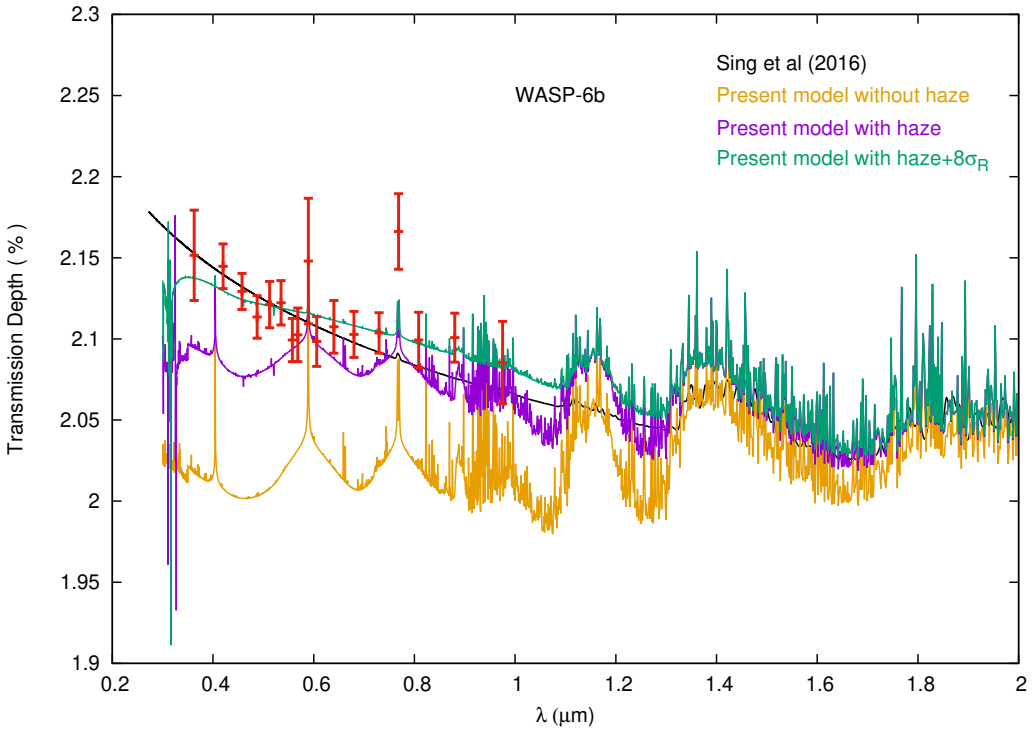

Figure 5.13: Comparison of observed data (red) and model transmission spectra for WASP-6b with and without haze.

that inclusion of sub-micron size haze can produce a comparable transmission spectrum that is obtained by invoking additional Rayleigh scattering opacity in the model by Kempton et al. (2017). Figure 5.12 also demonstrates the difference in the transmission spectra with and without the effect of scattering albedo when the scattering opacity is increased by a thousand times. The inclusion of haze results in transmission depth comparable to that presented by Sing et al. (2016) in the optical only if the diffusion by scattering is excluded in the model. Clearly, the diffuse radiation due to scattering increases the transmitted flux resulting into a decrease in the transmission depth even up to 2.0 μm. However, all the models converge at wavelengths longer than 2.0 μm as the scattering coefficient and hence the scattering albedo becomes negligible beyond this wavelength. We point out here that the rapid increase in the transmission depth at wavelengths shorter than 0.5 micron may be due to other effects, e.g., stellar activities, star-spots etc.

Finally, we present in Figure 5.13 the model transmission spectra for WASP-

6b with and without incorporating haze. It is worth mentioning that our numerical method ensures that the dust number density does not exceed the mass of heavy elements. Figure 5.13 shows that even with the maximum allowed values of dust number density, the transmission depth fails to fit the observed data in the optical region. We have achieved a good model fit with the observed data by increasing the Rayleigh scattering opacity eight times its original value in addition to incorporating haze. This indicates that a better cloud model is needed to fit the observed data.

5.8 Conclusions

We have presented detail numerical models of transmission spectra for hot Jupiter-like exoplanets by solving the multiple scattering radiative transfer equations with non-zero scattering albedo instead of using the Beer-Bouguer-Lambert law. We have demonstrated that the solution of the radiative transfer equations that incorporate the diffuse reflection and transmission radiation field due to scattering yields significant changes in the transmission depth at the optical wavelength region, especially if the atmosphere is cloudy. However, at longer wavelength scattering becomes negligible and the transmission spectra overlap with that derived by using Beer-Bouguer-Lambert law. We have compared our model spectra with the observed data and with two different theoretical models that include opacity due to scattering but do not take into account the diffuse reflection and transmission of the incident radiation field due to atmospheric scattering. We also include additional opacity and scattering albedo due to condensate cloud by adopting a simplified dust model. The most important message conveyed by the present work is that in order to analyze the observed optical transmission spectra of exoplanets, the retrieval models need to incorporate the scattering albedo that gives rise to diffused radiation field which is added to the stellar radiation transiting through the planetary atmosphere. Thus a correct and consistent procedure is to solve the

multiple scattering radiative transfer equations. A substantial amount of diffuse stellar radiation increases the transmitted flux resulting in a decrease in the transmission depth. However, in the infrared wavelength region where the effect of scattering is negligible, Beer-Bouguer-Lambert law can very well be employed to calculate the transmission depth.

Chapter 6

Detailed Modeling of Transmission Spectra in the Infrared[1]

6.1 Introduction

Transit spectroscopy is an essential tool for probing into the upper atmospheres of the close-in exoplanets (Charbonneau et al., 2002; Sengupta, Chakrabarty, & Tinetti, 2020; Sing et al., 2016). An accurate interpretation of the observed transit spectra, however, requires a self-consistent theoretical model that must incorporate the physical and chemical properties of the planetary atmospheres in sufficient detail, including scattering albedo (e.g. de Kok & Stam, 2012; Sengupta, Chakrabarty, & Tinetti, 2020) and thermal re-emission from the night side (this work). We have already demonstrated in Chapter 5 that the inclusion of the diffused reflection and transmission due to scattering of the starlight transmitted through a planet's atmosphere affect the transmitted flux. This alters the transit depth significantly in the optical compared to the previous models (see Section 4.4 and Sengupta, Chakrabarty, & Tinetti, 2020) that have only considered the effect of the total extinction coefficient and ignored the ef-

[1] *This chapter is also published in The Astrophysical Journal, Chakrabarty and Sengupta, vol. 898:89, 2020.*

fect of scattering albedo in calculating the transmission spectra. However, we have also shown that the effect of scattering albedo on transmission spectra is less than 10 ppm in the infrared region.

On the other hand, because of the extreme proximity to their parent stars, many gas giants are extremely hot. As they are tidally locked with their host stars, the dayside of such a planet is so hot due to the intense irradiation that its equilibrium temperature for zero albedo, T_{eq0} can reach as high as $\sim$4000 K (Gaudi et al., 2017). The heat is redistributed to the night side by the advection process and the night side of the planet facing the observer during transit also becomes hot depending on the heat re-circulation efficiency, ϵ of the planetary atmosphere. The average temperature T_n of the night side of the planet can be estimated by the relation (Cowan & Agol, 2011; Keating & Cowan, 2017)

$$T_n = T_{eq0}(1 - A_B)^{\frac{1}{4}} \epsilon^{\frac{1}{4}} = T_{n0}(1 - A_B)^{\frac{1}{4}} \tag{6.1}$$

where A_B is the Bond albedo of the atmosphere. We define T_{n0} as the night-side average temperature for zero Bond albedo. Even with a small value of ϵ, the average night side temperature T_n can be quite high if T_{eq0} is high enough. Some previous studies provide an estimation of the night-side temperature of a few exoplanets. For example, Keating & Cowan (2017) report $T_n = 1080 \pm 11$ K for WASP-43 b; Demory et al. (2016) report a night-side brightness temperature of 1380 ± 400 K for 55 Cancri e based on their observation in the 4.5-μm channel of the Spitzer Space Telescope Infrared Array Camera (IRAC); Arcangeli et al. (2019) report $T_n \leq 1430$ K for WASP-18 b at 3-σ level; etc. Such a hot region facing the observer would emit radiation in the infrared wavelengths which should be added up with the transmitted stellar radiation. Thus the transmitted flux would be affected by the re-emission of hot planets in the longer wavelengths.

In this chapter, we have demonstrated the effect of thermal re-emission on the transit spectra of the hot Jupiters of different size and surface gravity and

with equilibrium temperature ranging from 1200K to 2400K. In Section 6.2 we provide the formalisms for calculating the transit depth with and without thermal re-emission. Section 6.3 outlines the detailed procedure followed to calculate the transmitted and the re-emitted flux from the hot-Jupiters. In Section 6.4 we discuss the 1D pressure-temperature grids calculated and the databases adopted for the calculation of abundance and absorption and scattering opacity for the modeling of the atmospheres of the hot-Jupiters. In Section 6.5 we discuss the results from all the case studies as well as the results from the testing of detectability of the effect of thermal emission on the transit spectra of hot Jupiters by simulating observational transit spectroscopic data to be observed from the upcoming James Webb Space Telescope (JWST) using the open-source Pandexo code (Batalha et al., 2017) available in the public domain [2]. In the last section, we conclude the key points.

6.2 The Transit Depth with Planetary Thermal Re-emission

The transit spectra of an exoplanet are expressed in term of transit depth $D(\lambda)$ which is the difference in stellar flux during out of transit and during the transit of the planet and normalized to the unblocked stellar flux. When the planetary radiation does not contribute to the stellar flux, it can be written as (see Equation 4.5.1)

$$D_{NE}(\lambda) = 1 - \frac{F_{in}}{F_{out}} = 1 - \frac{(1 - \frac{R_{PA}^2}{R_*^2})F_* + F_P}{F_*} \tag{6.2}$$

where, D_{NE} is the transit depth with no thermal radiation from the transitting planet, R_{PA} is the sum of the base radius R_P and the atmospheric height of the planet, F_{in} and F_{out} are the in-transit and out-of-transit stellar flux respectively. In case of pure transmission when thermal emission of the planet is ignored, F_{out}

[2] https://github.com/natashabatalha/PandExo

is the stellar flux F_*. F_P is the portion of the stellar flux which is transmitted through the upper atmosphere of the planet and undergoes absorption and scattering through the medium. The above equation can also be written as:

$$D_{NE}(\lambda) = \frac{R_{PA}^2}{R_*^2} - \frac{F_P}{F_*} \tag{6.3}$$

For a transiting planet with a hot night side facing the observer, the re-emitted radiation flux F_{Th} is added to the observed fluxes. Hence, the transit spectra including the effect of the re-emission from the planet can be expressed as:

$$D_E(\lambda) = 1 - \frac{(1 - \frac{R_{PA}^2}{R_*^2})F_* + F_{Th}\frac{R_{PA}^2}{R_*^2} + F_P}{F_* + F_{Th}\frac{R_{PA}^2}{R_*^2}} \tag{6.4}$$

A transit spectrum is usually produced from observation by calculating the transit depth at different wavelengths normalized with respect to the baseline flux, i.e., the flux observed right before ingress or immediately after egress. One of the methods is to calculate the wavelength-dependent transit depth from the light curves at different wavelength bins extracted from the time-series spectra of the host stars observed during a transit event using space-based instruments like HST+STIS, HST+WFC3, etc. (Berta et al., 2012; Charbonneau et al., 2002; Deming et al., 2013; Gibson et al., 2012; Sing et al., 2016, etc.) or ground-based instruments like VLT+FORS, VLT+FORS2, Magellan+MMIRS, GEMINI-N+GMOS, GTC+OSIRIS etc (Bean et al., 2011; Huitson et al., 2017; Nikolov et al., 2016; Pallé et al., 2016; Stevenson et al., 2014, etc.). The wavelength-dependent transit depth can also be calculated directly from the photometric light curves at different wavelength bands observed using ground-based instruments or space-based instruments like Spitzer Space Telescope Infrared Array Camera (IRAC) etc. during a transit event (Sing et al., 2016; Tinetti et al., 2007a). In either case, the normalized wavelength-dependent transit depth (equivalently, the wavelength-dependent radius) can be more accurately modeled with the incorporation of the planetary thermal

emission F_{Th}. However, the impact on the accuracy by omitting the effect of F_{Th} might be, in some cases (e.g., at a wavelength shorter than 2 μm), small compared to the uncertainties in the data. We discuss the significance of the effect of F_{Th} with respect to the uncertainties in the observational data elaborately in Section 6.5.

Finally, Equation 6.2 and Equation 6.4 gives

$$\frac{D_{NE}(\lambda)}{D_E(\lambda)} = 1 + \frac{F_{Th}}{F_*}\frac{R_{PA}^2}{R_*^2}. \tag{6.5}$$

As evident from Equation 6.5 the contribution from the thermal re-emission of the planet reduces the transit depth.

6.3 Calculations of Transmission and Emission Flux

To calculate the transmitted stellar flux F_P that passes through the atmosphere of a hot Jupiter we calculate the reduced stellar intensity that suffers absorption and scattering in the planetary atmosphere and then integrate over the angle subtended by the annular region of the atmosphere. Sengupta, Chakrabarty, & Tinetti (2020) have shown that an accurate approach to calculate the reduced intensity is to solve the multi-scattering radiative transfer equations that incorporate the diffused reflection and transmission of radiation due to scattering. The radiative transfer equations including diffused reflection and transmission for a plane-parallel geometry can be expressed as (e.g. Chandrasekhar, 1960; Sengupta, Chakrabarty, & Tinetti, 2020)

$$\mu\frac{dI(\tau_{LOS},\mu,\lambda)}{d\tau_{LOS}} = I(\tau_{LOS},\mu,\lambda) - \frac{\omega}{2}\int_{-1}^{1} p(\mu,\mu')I(\tau_{LOS},\mu,\lambda)\mathrm{d}\mu' - \frac{\omega}{4}F_* e^{-\tau_{LOS}/\mu_0}p(\mu,\mu_0) \tag{6.6}$$

where $I(\tau_{LOS},\mu,\lambda)$ is the specific intensity of the diffused radiation field

along the direction $\mu = \cos\theta$, θ being the angle between the axis of symmetry and the ray path, F_* is the incident stellar flux in the direction $-\mu_0$, ω is the albedo for single scattering i.e. the ratio of scattering co-efficient to the extinction coefficient, $p(\mu, \mu')$ is the scattering phase function that describes the angular distribution of the photon before and after scattering and τ_{LOS} is the optical depth along the line of sight to the observer. The detail method for calculating τ_{LOS} is given in Sengupta, Chakrabarty, & Tinetti (2020). We adopt the Rayleigh phase function (e.g. Chandrasekhar, 1960) for cloud-free atmospheres. For cloudy atmospheres, we use the Mie phase function. This is elaborated in Section 6.5.5. The planetary thermal emission is important only at longer wavelengths where the effect of scattering albedo is negligible, less than 10 ppm (Sengupta, Chakrabarty, & Tinetti, 2020), even in the presence of atmospheric clouds. Therefore, in this work, we have ignored the effect of scattering albedo in the calculation of F_P.

On the other hand, to calculate the flux of the planetary thermal radiation F_{Th}, we treat the planet as a self-luminous object and solve the radiative transfer equations in the following form:

$$\mu \frac{dI(\tau, \mu, \lambda)}{d\tau} = I(\tau, \mu, \lambda) - \frac{\omega}{2} \int_{-1}^{1} p(\mu, \mu') I(\tau, \mu, \lambda) \mathrm{d}\mu' - (1 - \omega) B(\tau, \lambda) \quad (6.7)$$

where, $I(\tau, \mu, \lambda)$ denotes the specific intensity of the thermal radiation field along the direction μ, τ is the optical depth in the radial direction, $B(\tau, \lambda)$ is the Planck function corresponding to the temperature of the atmospheric layer with optical depth τ at a particular wavelength.

The above radiative transfer equations are solved by using the Discrete Space Theory method (Peraiah & Grant, 1973). The numerical method is described in Sengupta, Chakrabarty, & Tinetti (2020) and in Sengupta & Marley (2009). F_P and F_{Th} are calculated separately and used into Equation 6.2 and in Equation 6.4 to derive D_{NE} and D_E respectively.

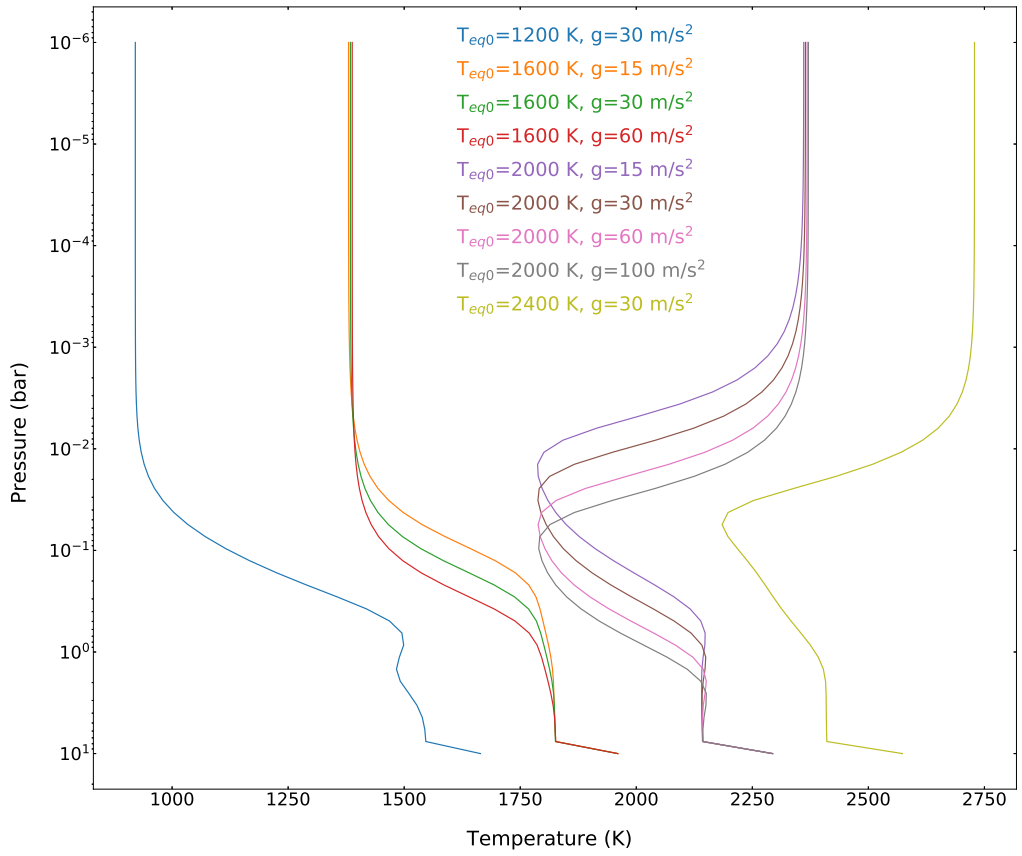

Figure 6.1: Pressure-Temperature profiles for different T_{eq0} and g adopted in this work. For all the cases, the effect of TiO and VO is included.

6.4 Pressure-Temperature Grids and the Opacity and Abudance Data

The atmospheric pressure-temperature structure plays an important role not only in determining the optical depth of the medium but also in estimating the thermal radiation of the planet. In order to calculate the pressure-temperature profiles, we use the FORTRAN implementation of the analytical models of non-Grey irradiated planets provided by Parmentier & Guillot (2014); Parmentier et al. (2015) as explained in Section 4.5.3. For $T_{eq0} \geq 1700K$, the pressure-temperature (P-T) profiles show temperature inversion when TiO and VO are included. Previous studies, including, e.g., Sengupta, Chakrabarty, & Tinetti (2020) find that the hot-Jupiters are almost opaque to the transmitted flux at

pressures level below 1 bar. Therefore, in the present work, we have considered the P-T profiles up to 1 bar pressure level such that the base radii R_P of the hot Jupiters considered in the calculations of the transmission spectra are located at 1 bar pressure level.

However, the thermal radiation of a hot planet emerges from a deeper layer of the atmosphere and so we have considered the P-T profiles of hot Jupiters with T_{eq0} ranging between 1200K to 2400K and the surface gravity over a range of 15-100 m/s^2 at 10 bar pressure level. Figure 6.1 shows the P-T profiles for all the case-studies with different T_{eq0}.

For all the calculations we have adopted solar metallicity and solar system abundance for the atoms and the molecules present in the atmospheres. We have considered 28 molecular and atomic species as mentioned in Sengupta, Chakrabarty, & Tinetti (2020). The abundance for all these atoms and molecules has been calculated using the abundance database given in the open-source package `Exo-Transmit` (Kempton et al., 2017, See Section 4.4.1). Also, to calculate the absorption and scattering coefficients we have used the opacity database from the same package. These opacities are based on the molecular databases of Freedman, Marley, & Lodders (2008) and Freedman et al. (2014). We have also calculated the opacity due to atmospheric clouds comprising mainly of amorphous Forsterite by using Mie theory (see Section 6.5.5).

Modeling an atmosphere with a high day-night temperature contrast is not straightforward because 1D pressure-temperature (P-T) profile may not be adequate in such a scenario and therefore one requires a 3D P-T mapping using Global Circulation Model (GCM) or a limb-averaged P-T profile (Evans et al., 2018; Kataria et al., 2015, 2016). In order to avoid such complications, we have assumed a hot-Jupiter atmosphere with $\epsilon = 1$ ($T_{n0} = T_{eq0}$) i.e. a globally averaged P-T profile in all the cases as our main motive is to demonstrate the effect of the night-side temperature T_n. This corresponds to $f = 0.25$, where f is the flux parameter as defined in Burrows, Sudarsky, & Hubbard (2003) and

also, used in Guillot (2010); Parmentier & Guillot (2014); Parmentier et al. (2015); etc.

The night side of the planetary atmosphere may also get warmed up by the release of the internal energy characterized by the internal temperature (T_{int}) and may cause thermal radiation (self-emission) but this radiation should be insignificant as compared to the thermal re-emission from planet older than 100 Myr (Burrows et al., 1997) in age.

6.5 Case Studies: Simulation and Testing of Detectability

We checked the detectability of the effect of thermal emission on the transit spectra by using the simulated data. We also investigate the extent to which the transit spectra D_E depend on the planetary properties such as T_n, R_P/R_*, the atmospheric clouds and the surface gravity as well as the spectral types of the host stars. The following subsections describe the results from these case studies.

6.5.1 Detectability with JWST

To understand the significance of the effect of thermal emission from transiting hot Jupiters on the transit spectra, we need to compare the difference between D_{NE} and D_E with the noise levels of the actual observed data. For that purpose, we have focused on the observing capability of the upcoming James Webb Space Telescope (JWST) as this mission is going to be at the forefront of exoplanet characterization. Considering the contribution of thermal emission from hot Jupiters to the transit spectra, we use our model calculations for D_E and, simulate some observational transit spectra with error-bars that can be observed using the IR instruments of JWST. The simulation is done by using the open-source code Pandexo (Batalha et al., 2017). A host star of spectral

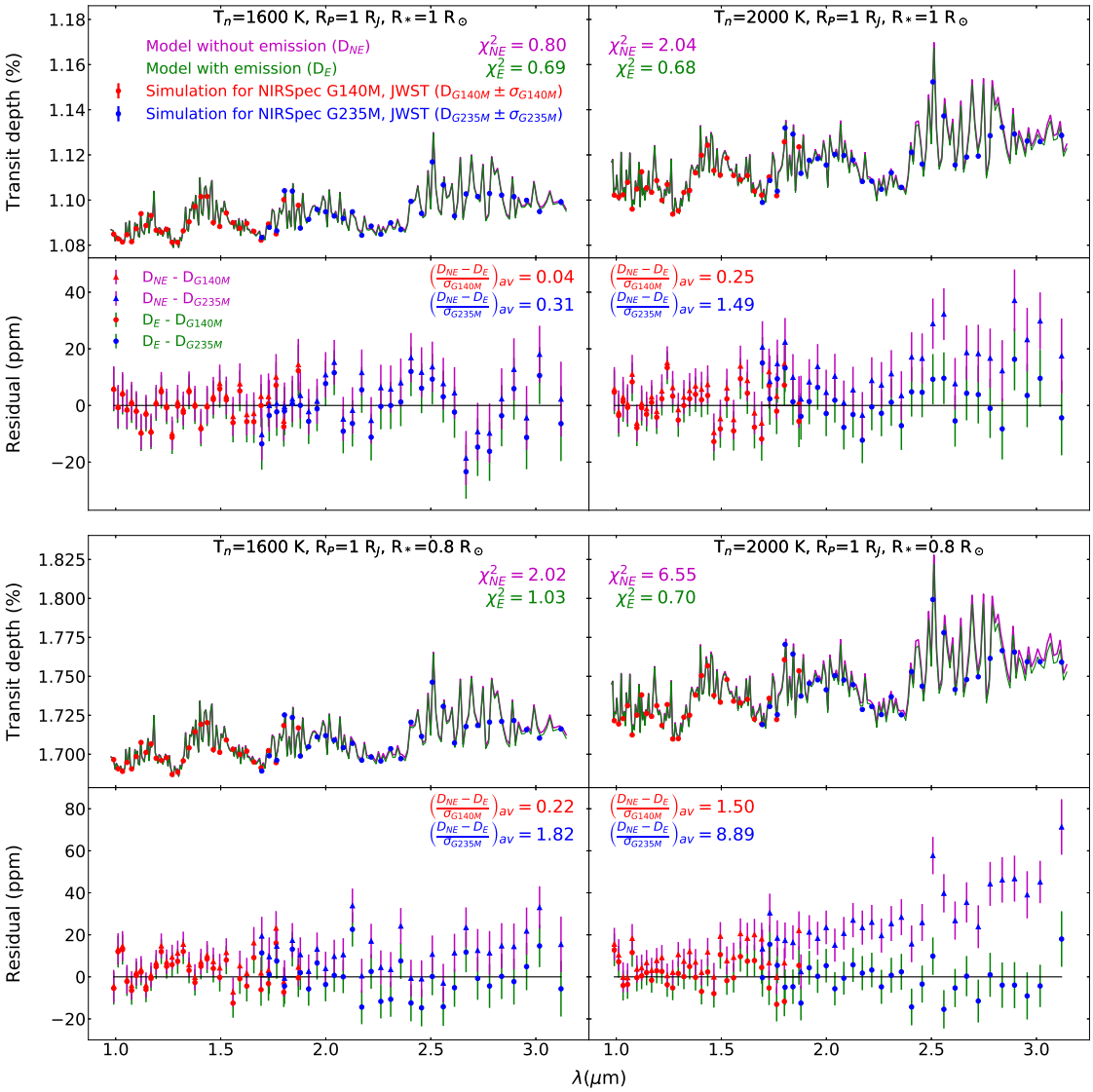

Figure 6.2: Simulated observational data of transit depth with emission combined over 4 observed transit events using instrument modes NIRSpec G140M and NIRSpec G235M of JWST with error-bars, viz. $D_{G140M} \pm \sigma_{G140M}$ (red) and $D_{G235M} \pm \sigma_{G235M}$ (blue) respectively, are shown in the top panels assuming a G2V host star with J-band magnitude = 8. Models without and with thermal emission (D_{NE} in magenta and D_E in green respectively) for different values of T_n and R_* with $R_P = 1\ R_J$ are shown with corresponding chi-square values, keeping g fixed at g = 30 m/s^2. The bottom panels show the difference between the model without emission and the simulated observational data (red and blue triangles with magenta error-bars) as compared to the difference between the the model with emission and the same simulated observational data (red and blue circles with green error-bars). Also, the mean of the ratio of the difference between the two models to the noise levels of the two modes, viz. $\left(\frac{D_{NE}-D_E}{\sigma_{G140M}}\right)_{av}$ and $\left(\frac{D_{NE}-D_E}{\sigma_{G235M}}\right)_{av}$, are shown in the bottom panels.

type G2V with J-mag=8 and a saturation level equal to 70 % of the full well potential are considered for this simulation. The spectra with noise-levels with

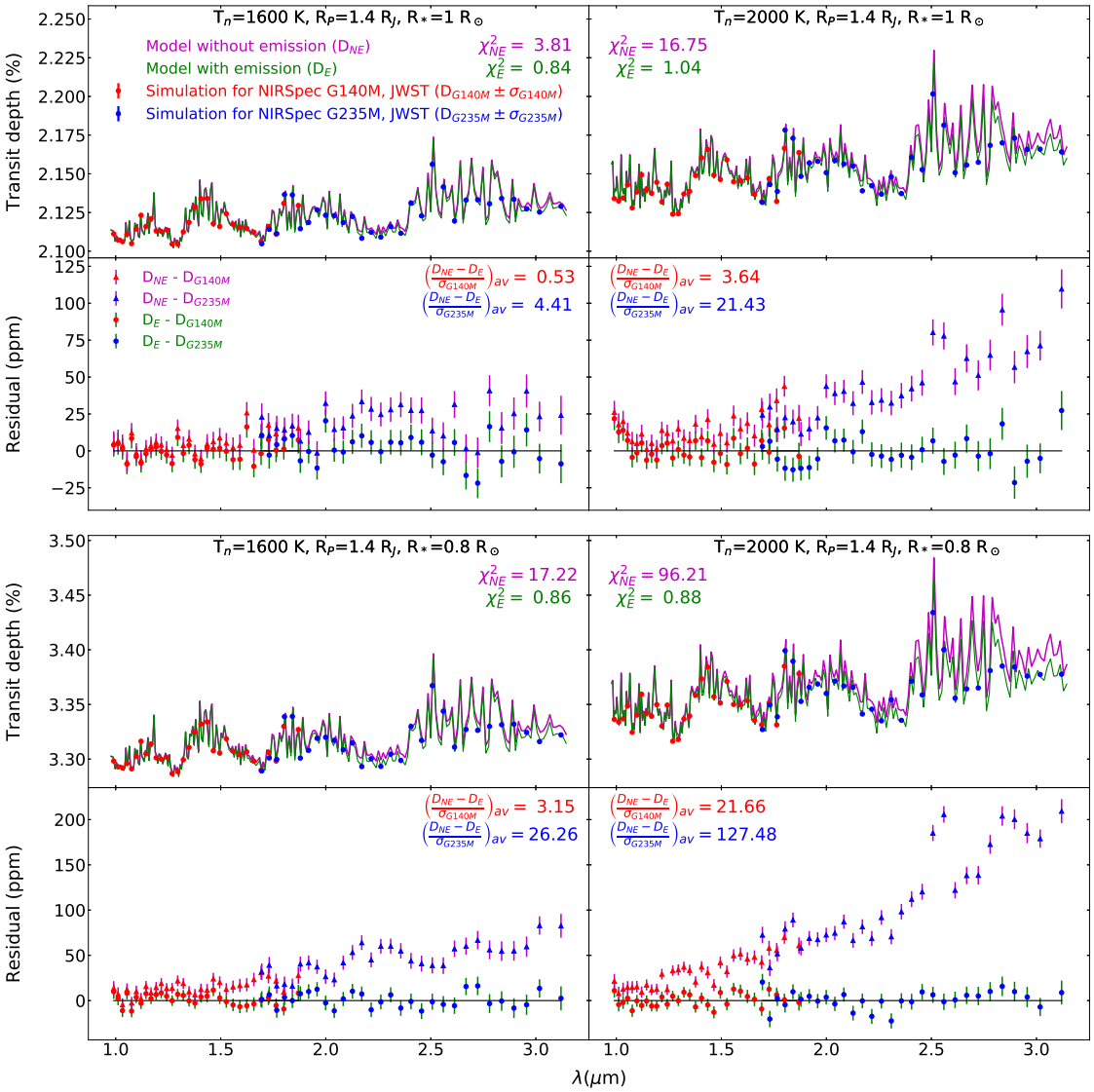

Figure 6.3: Same as Figure 6.2 but with $R_P = 1.4\ R_J$.

a resolution of $R \sim 50$ are calculated by combining the data over 4 observed transit events, each with a duration of 2 hours (T_{14}). We have considered the instrument modes viz. NIRSpec G140M and NIRSpec G235M for the wavelength region 1-3 μm and NIRSpec G395M and MIRI LRS (slitless) for the wavelength region 3-8 μm (see Table 1 of Batalha et al. (2017)) and the corresponding simulated transit depth and noise levels are denoted by $D_{G140M} \pm \sigma_{G140M}$, $D_{G235M} \pm \sigma_{G235M}$, $D_{395M} \pm \sigma_{G395M}$ and $D_{LRS} \pm \sigma_{LRS}$ respectively. For each pair of instrument modes we present the comparison of the models

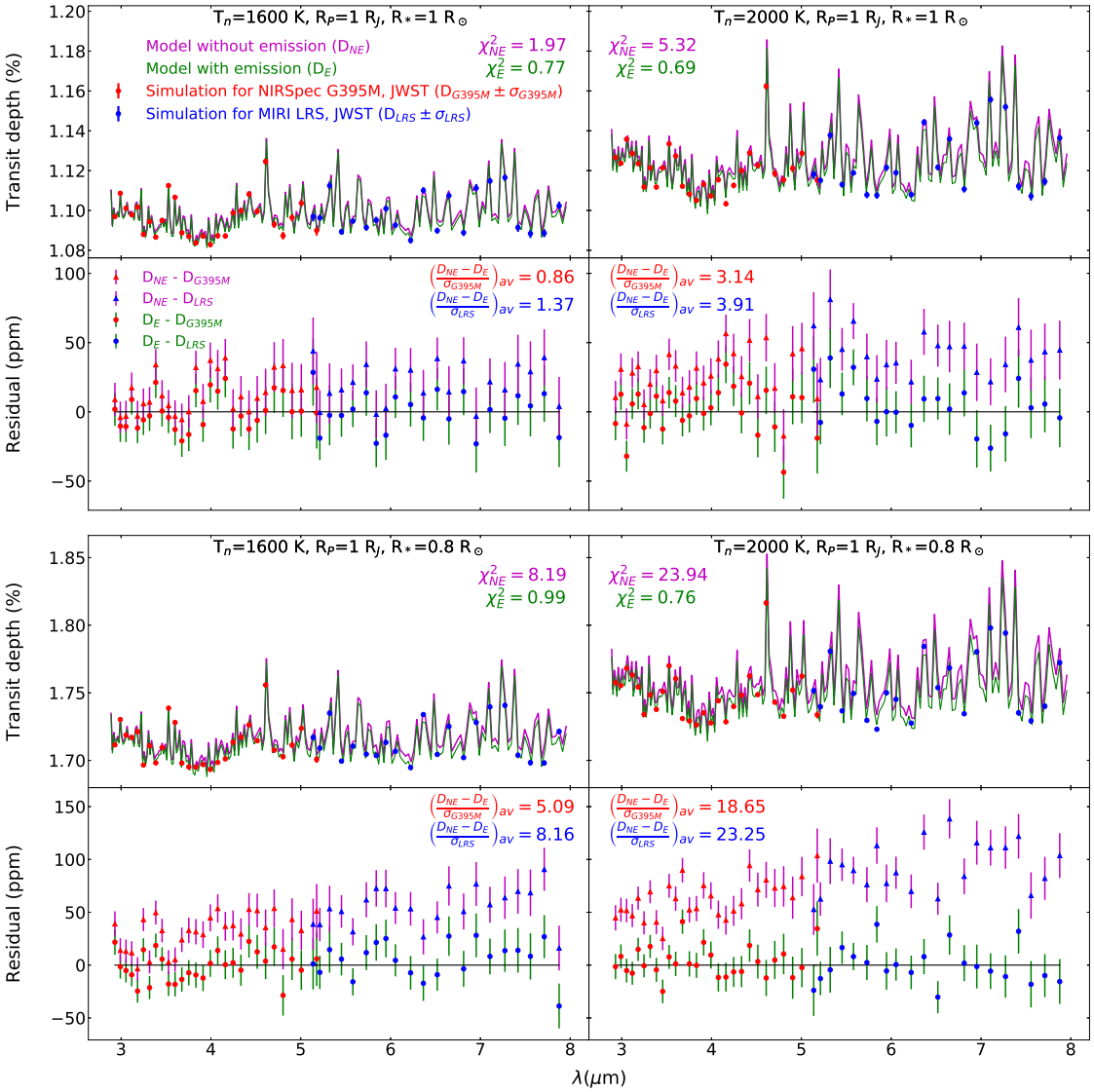

Figure 6.4: Simulated observational data of transit depth with emission combined over 4 observed transit events using instrument modes NIRSpec G395M and MIRI LRS (slitless) of JWST with error-bars, viz. $D_{G395M} \pm \sigma_{G395M}$ (red) and $D_{LRS} \pm \sigma_{LRS}$ (blue) respectively, are shown in the top panels assuming a G2V host star with J-band magnitude = 8. Models without and with thermal emission (D_{NE} in magenta and D_E in green respectively) for different values of T_n and R_* with $R_P = 1\ R_J$ are shown with corresponding chi-square values, keeping g fixed at g=30 m/s^2. The bottom panels show the difference between the model without emission and the simulated observational data (red and blue triangles with magenta error-bars) as compared to the difference between the the model with emission and the same simulated observational data (red and blue circles with green error-bars). Also, the mean of the ratio of the difference between the two models to the noise levels of the two modes, viz. $\left(\frac{D_{NE}-D_E}{\sigma_{G395M}}\right)_{av}$ and $\left(\frac{D_{NE}-D_E}{\sigma_{LRS}}\right)_{av}$, are shown in the bottom panels.

(D_{NE} vs D_E), constructed using different sets of planetary paramters, with the simulated data along with their residuals in Figure 6.2-6.5. In Figure 6.2

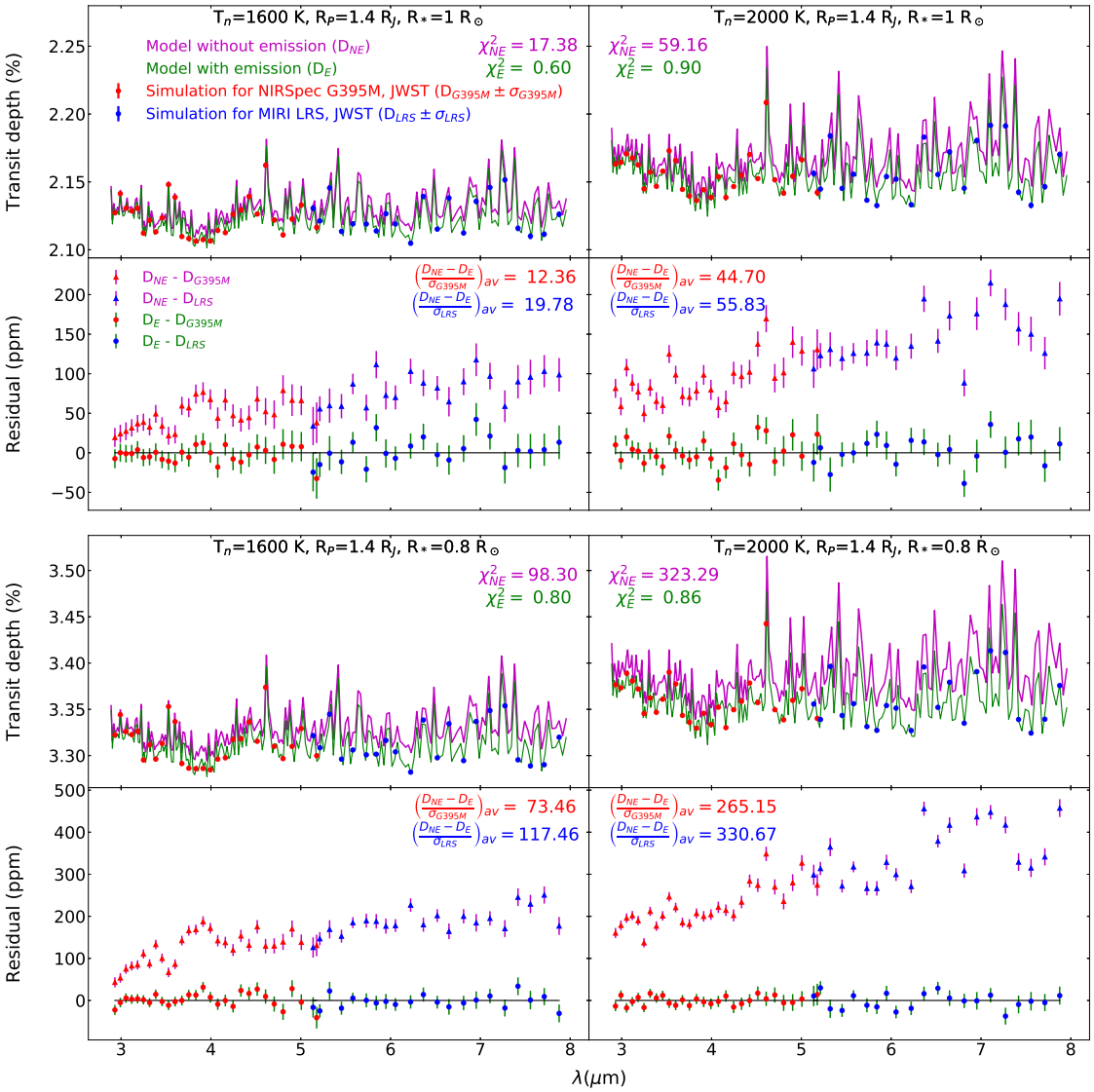

Figure 6.5: Same as Figure 6.4 but with $R_P = 1.4\ R_J$.

and Figure 6.4 the model parameters are (i) $T_n = 1600$K, $R_P = 1\ R_J$, $R_* = 1\ R_\odot$, (ii) $T_n = 2000$ K, $R_P = 1\ R_J$, $R_* = 1\ R_\odot$, (iii) $T_n = 1600$ K, $R_P = 1\ R_J$, $R_* = 0.8\ R_\odot$, and (iv) $T_n = 2000$ K, $R_P = 1R_J$, $R_* = 0.8R_\odot$. In Figure 6.3 and Figure 6.5, the model parameters are (i) $T_n = 1600$ K, $R_P = 1.4\ R_J$, $R_* = 1.4\ R_\odot$, (ii) $T_n = 2000$ K, $R_P = 1.4\ R_J$, $R_* = 1\ R_\odot$, (iii) $T_n = 1600$ K, $R_P = 1.4\ R_J$, $R_* = 0.8\ R_\odot$, and (iv) $T_n = 2000$ K, $R_P = 1.4R_J$, $R_* = 0.8R_\odot$. The figures also show the chi-square values of the models (top sub-panels) and the mean of the ratio of $(D_{NE} - D_E)$ to the 1-σ noise-levels of the above modes

(viz. σ_{G140M}, σ_{G235M}, σ_{G395M}, and σ_{LRS}).

These figures show that the difference between D_{NE} and D_E for $R_P/R_* = 1$ is of no or extremely low significance ($<$ 20 ppm and $<$ 4-σ). Also, at wavelengths up to 2 μm, the difference between D_{NE} and D_E is significant ($>$ 25 ppm and $\sim$ 22-σ) only for $T_n = 2000$ K, $R_P = 1.4R_J$, $R_* = 0.8R_\odot$. For all other combinations of T_n, R_P, and R_*, the difference is of no or low significance ($<$ 25 ppm and $<$ 4-σ). However, for wavelengths longer than 2 μm, we find that the difference between the models increases with increasing T_n and R_P/R_* and reaches up to 500 ppm (330-σ) for $T_n = 2000$ K, $R_P = 1.4R_J$, $R_* = 0.8R_\odot$. The chi-square values shown in these figures imply that for higher values of T_n and R_P/R_* and wavelength $\gtrsim 2\ \mu m$, the simulated data are fitted well with the model transit spectra only when planetary thermal emission is incorporated. This demonstrates the fact that in order to achieve the precision level of the instruments on-board JWST, the effect of thermal emission from hot Jupiters must be taken into consideration in the retrieval model for transit spectra.

6.5.2 Host Stars of Different Spectral Types

The transit depth with no planetary thermal emission, D_{NE}, is absolutely independent of the stellar spectrum, as evident from Equation 6.6. The factor $\frac{F_P}{F_*}$ solely depends on the physical and chemical properties of the planetary atmospheres and provides only the reduction in the stellar flux due to absorption. However, Equation 6.7 suggests that, when planetary emission is included, the transit depth, D_E, for planets with the same T_n, becomes dependent on the flux of the host star. Consequently, it depends on the spectral types of the host stars. Figure 6.6 displays the difference between D_{NE} and D_E for planets with $R_P/R_* = 1.4R_J/R_\odot$ ($\sim$0.144), g=30m/s^2 and T_n =1600K orbiting stars of spectral types F5V, G5V, K5V, and M5V. Also, the 1-σ noise levels of the JWST instrument modes NIRSpec G140M, NIRSpec G235M, NIRSpec

G395M, and MIRI LRS (slitless) for the number of observed transits equal to 2 and 4 and host stars with J-band magnitude of 8 and 10 are shown in this figure. The model spectra show that the transit depths D_E for stars of different spectral types differ significantly at wavelengths longer than 3 μm. The cooler the host stars are, the more significant the difference is between the models with respect to the noise levels, as evident from Equation 6.5.

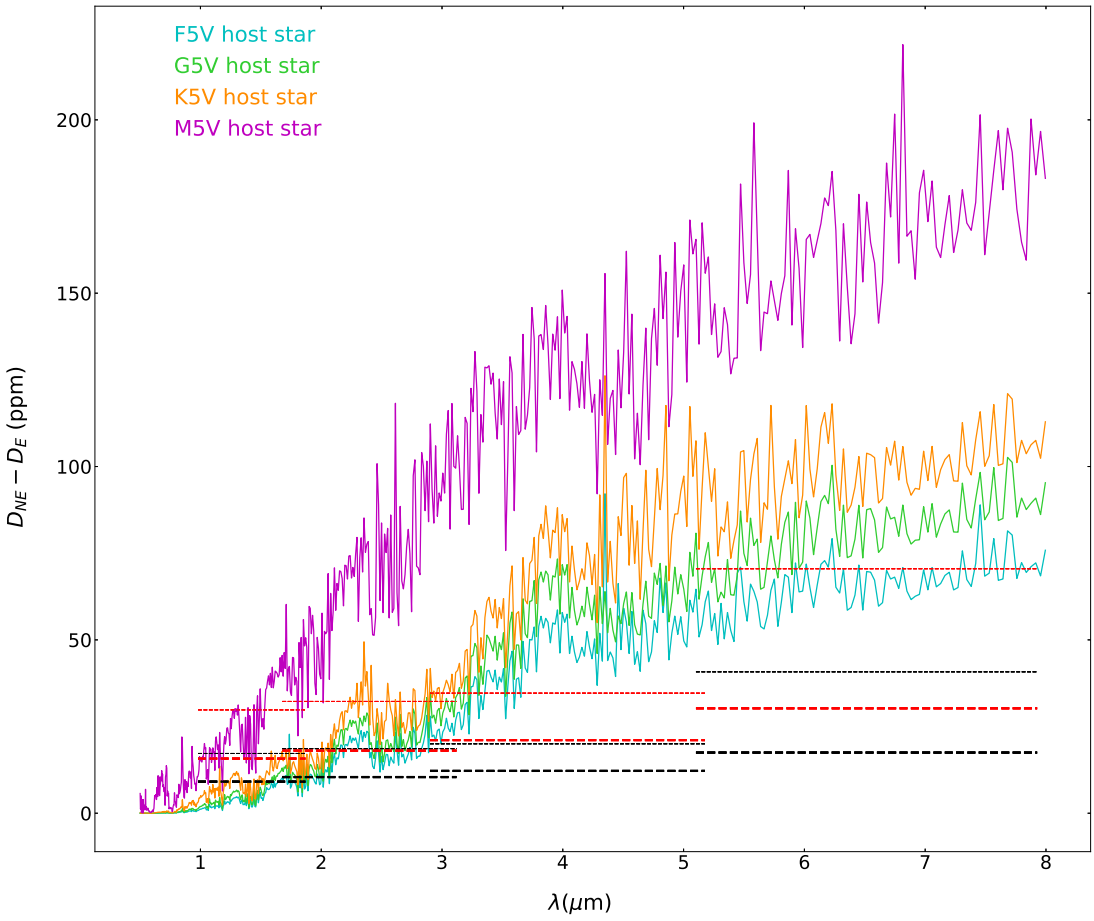

Figure 6.6: Difference between the models of transit depth without and with thermal emission from the hot-Jupiters with T_n = 1600 K, g=30 m/s^2, $R_P/R_* = 1.4R_J/R_\odot$ (∼0.144), orbiting around stars of different spectral types. Transit depth without emission is independent of the host star spectral type. The 1-σ noise-levels are shown in dashed lines from left to right for the JWST channels NIRSpec G140M, NIRSpec G235M, NIRSpec G395M, and MIRI LRS (slitless) respectively. The red and black dashed lines correspond to noise-levels for the number of observed transits equal to 2 and 4 respectively. The thick and thin dashed lines correspond to noise-levels for host stars with a J-band magnitude of 8 and 10 respectively.

6.5.3 Average Night-Side Temperature and Planetary Size

In order to investigate the effect of T_n, we calculate the difference between D_{NE} and D_E at different values of T_{n0} e.g., 1200K, 1600K, 2000K and 2400K. Figure 13 of Parmentier & Guillot (2014) demonstrates that the Bond albedo of planets with high equilibrium temperature is extremely low (< 0.01) for solar composition. Consequently, from Equation 6.1 it follows that, $T_n \approx T_{n0}$. These values of T_n correspond to atmospheric scale heights of 138 km, 186 km, 254 km and 387 km respectively. Figure 6.7 shows the difference between D_{NE} and D_E for these values of T_n and for different values of R_P and R_* e.g., (i) $R_P = 1R_J$, $R_* = 1R_\odot$, (ii) $R_P = 1R_J$, $R_* = 0.8R_\odot$, (iii) $R_P = 1.4R_J$, $R_* = 1R_\odot$ and (iv) $R_P = 1.4R_J$, $R_* = 0.8R_\odot$. It is clear from the figure that with the increase in T_n, the difference between D_{NE} and D_E increases because the thermal re-emission from the planet increases. The factor R_P/R_* also strongly dictates the significance of the difference with respect the noise-levels. This happens due to the fact that, with increasing R_P/R_*, the ratio of the thermal luminosity of the planet to the luminosity of the host star increases. Obviously, for a fixed planetary radius, the difference in D_{NE} and D_E increases with the decrease in the size of the host star.

Also, the 1-σ noise levels of the JWST instruments NIRSpec G140M, NIRSpec G235M, NIRSpec G395M and MIRI LRS (slitless) for the number of observed transit equal to 2 and 4 and host stars with J-band magnitude of 8 and 10 are shown in Figure 6.7. This helps us comprehend the significance of the difference between the models with respect to the noise levels for different numbers of observed transits and different host star J-band magnitudes. However, it can be safely ascertained that for higher values of R_P/R_* (see bottom 2 panels of Figure 6.7) and for $T_n > 1200$ K, the deviation of D_E from the standard model of transmission spectra (D_{NE}) at wavelength beyond 2 μm is so significant that observed transit spectra can be misinterpreted by the standard

model by 10-300 σ (representing a change up to 0.5% in transit depth).

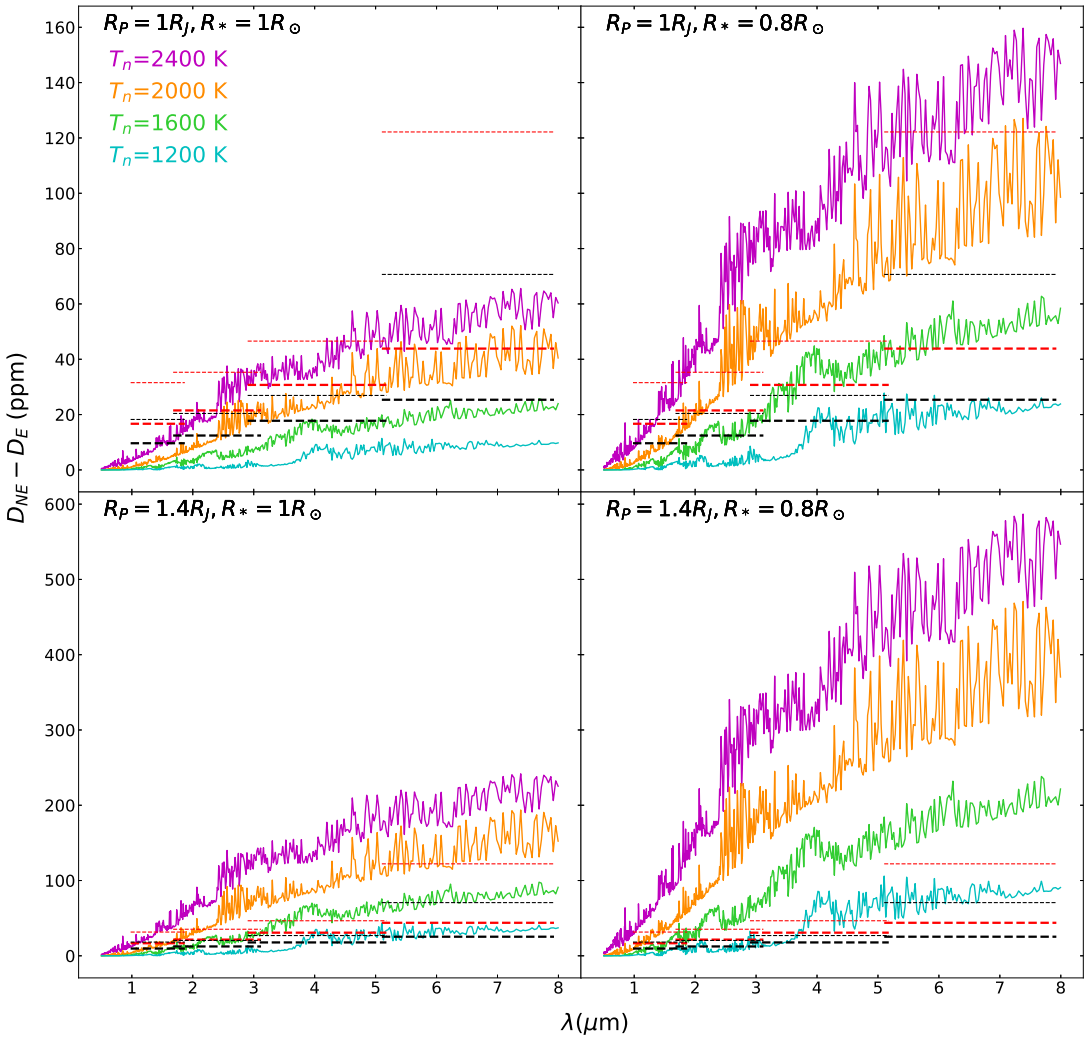

Figure 6.7: Difference between the models of transit depth without and with planetary thermal emission for different values of T_n, R_P and R_*, keeping g fixed at 30m/s^2. The 1-σ noise-levels are shown in dashed lines from left to right for the JWST channels NIRSpec G140M, NIRSpec G235M, NIRSpec G395M and MIRI LRS (slitless) respectively. The red and black dashed lines correspond to noise-levels for the number of observed transits equal to 2 and 4 respectively. The thick and thin dashed lines correspond to noise-levels for host stars with J-band magnitude of 8 and 10 respectively.

6.5.4 Surface Gravity

We have calculated D_{NE} and D_E for g=15, 30, 60 and 100 m/s^2 as shown in Figure 6.8 for a fixed values of T_n =2000K, $R_P = 1.4R_J$ and $R_* = 1R_\odot$. These values of g correspond to atmospheric scale heights, estimated by using

T_n=2000K, of 508 km, 254 km, 127 km and 76 km respectively. We find that with increasing g the transmission flux F_P decreases. However, the value of g has almost no effect on the calculation of F_{Th} and hence, the difference between D_{NE} and D_E is almost independent of g, the surface gravity of the planet.

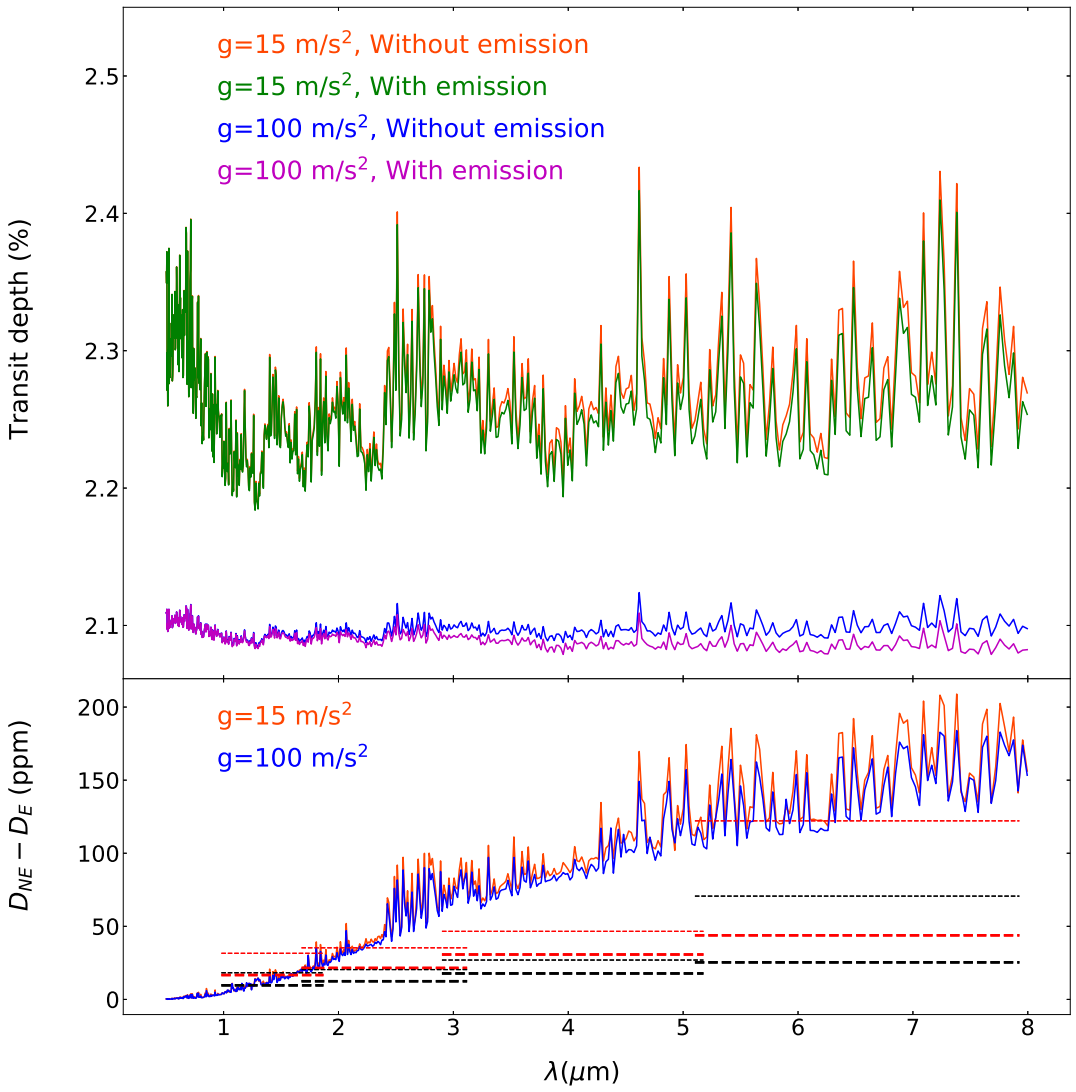

Figure 6.8: Top - Models of transit depth without and with thermal emission for different values of g and for T_n=2000K, R_P=1.4R_J and R_*=1$R_\odot$. Bottom - Difference between the above models for each value g which shows no dependence on g. The 1-σ noise-levels are shown in dashed lines from left to right for the JWST channels NIRSpec G140M, NIRSpec G235M, NIRSpec G395M and MIRI LRS (slitless) respectively. The red and black dashed lines correspond to noise-levels for the number of observed transits equal to 2 and 4 respectively. The thick and thin dashed lines correspond to noise-levels for host stars with J-band magnitude of 8 and 10 respectively.

6.5.5 Atmospheric Clouds

Clouds and hazes are a ubiquitous feature in the planetary atmospheres. For hot exoplanets, silicates may condensate in the upper atmosphere. Gas giant planets with comparatively cooler night sides can have thick atmospheric clouds that may affect the spectra in the optical and near-infrared wavelength region. However, at higher day or night temperatures, clouds may either completely evaporate or may form a thin layer of haze in the uppermost atmosphere. As discussed in the previous subsection, the effect of thermal emission is significant only at wavelengths longer than 2μm and for a night-side temperature $T_n >$ 1200 K. Therefore, even in the presence of a thin layer of haze, we don't expect the transmission spectra of planets having $T_n > 1200$ K to be affected in the infra-red region where thermal re-emission is important. Nevertheless, we have investigated the effects of the thin clouds on the transmission spectra of a planet with $T_n = 1600$ K. For this purpose, we have considered a simple model for thin haze in the uppermost atmosphere. The formalism is adopted from Griffith, Yelle, & Marley (1998); Saumon et al. (2000). We consider grains of amorphous Forsterite (Mg_2SO_4) of mean diameter 0.5 μm as the dominant constituent of the clouds, located within a thin region of the atmosphere bound by a base and a deck. Within this region, the sizes of the particles follow a log-normal distribution and the vertical density distribution of the cloud particles follows the relation (See Section 5.6)

$$n(P) = n_0 \frac{P}{P_0}$$

where, n(P) is the number density of the cloud particles at pressure level P, P_0 is the pressure at the base radius, and n_0 is a free parameter with the dimension of number density. The details of the model adopted can be found in Sengupta, Chakrabarty, & Tinetti (2020). The deck and base of the haze are fixed at 0.1 Pa and 100 Pa pressure levels respectively.

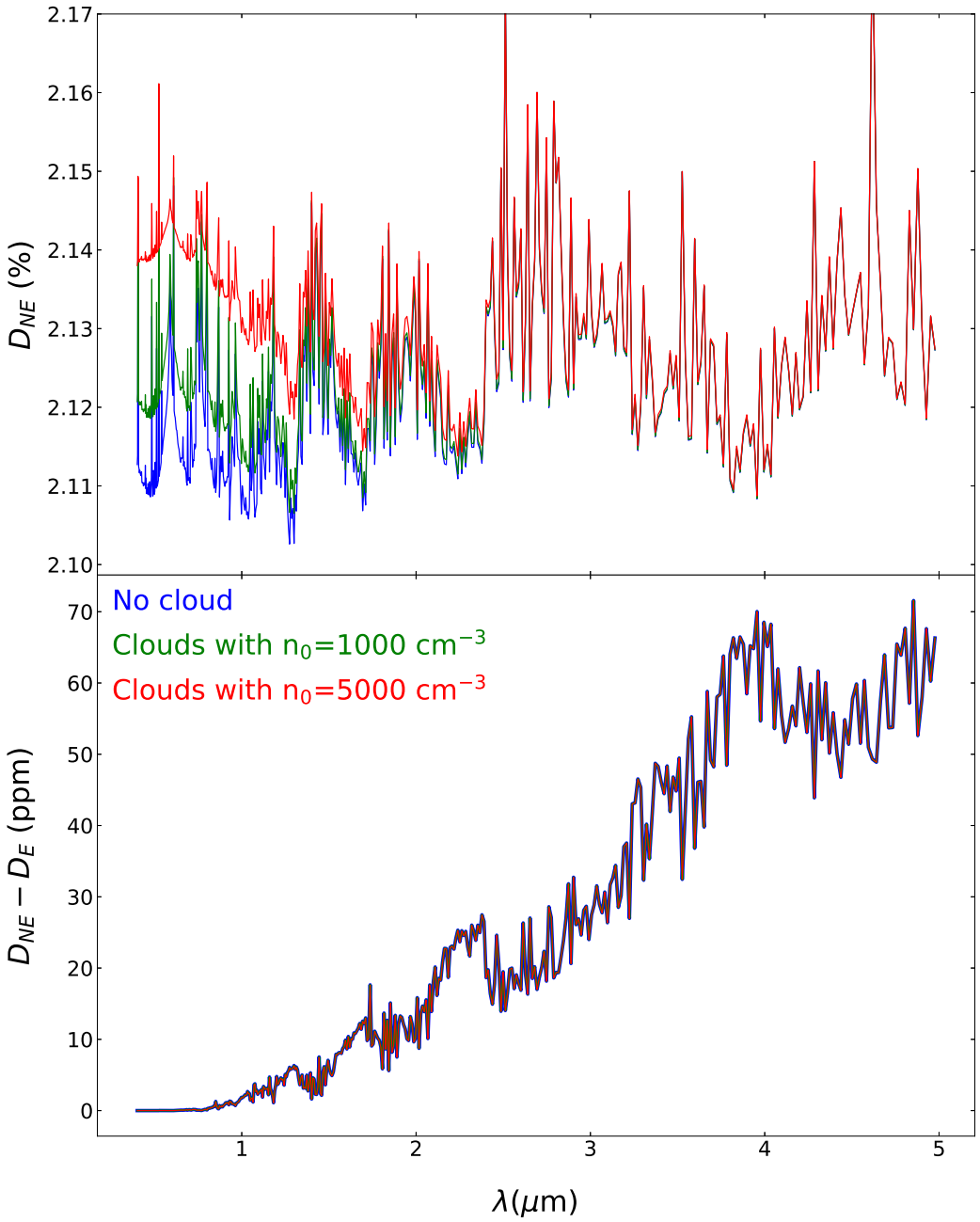

Figure 6.9: Top - Models of transit depth with thermal emission with different cloud abundance as well as without any cloud for T_n=1600K, g=30 m/s^2, R_P=1.4R_J and R_*=1$R_\odot$. Bottom - Difference between the models without and with thermal emission from the planets for the above cloud abundances as well as no cloud.

We use the Mie theory of scattering to calculate the wavelength-dependent scattering coefficients, extinction coefficients, and the phase functions at different pressure atmospheric depth (Bohren & Huffman, 1983; Fowler, 1983;

Hansen & Travis, 1974; Sengupta, Chakrabarty, & Tinetti, 2020; Sengupta & Marley, 2009; van de Hulst, 1957, etc.). Figure 6.9 shows D_{NE} (in top panel) and the difference between D_{NE} and D_E (bottom panel) for cloud models with $n_0 = 1000$ cm^{-3} and $n_0 = 5000$ cm^{-3}. We compare the results with that of a cloud-free atmosphere. Although the transit depth without thermal emission, D_{NE}, can alter depending on the cloud structure and opacity, the difference between D_{NE} and D_E does not change much as the emission flux (F_{Th}) is not affected significantly in the infra-red region by the presence of cloud. Figure 6.9 shows that the difference between D_{NE} and D_E does not change at all with clouds. Hence, the clouds do not play an important role in determining the transit depth at the infra-red wavelength region of ultra-hot Jupiters.

6.6 Conclusion

We demonstrate that the effect of thermal re-emission from the night side of hot Jupiters on the transit spectra can be significant at the infrared wavelength region if the equilibrium temperature of the planet is higher than about 1200K and if the planet is large enough in size such that $R_P/R_* > 0.1$. The contribution of planetary thermal emission to the transit spectra can significantly exceed the total noise budget (photon noise plus readout noise) of the IR instruments on-board the upcoming JWST that will perform transit spectroscopy. Hence, a retrieval model that does not include planetary thermal emission would overestimate the transit depth and thus can lead to a wrong interpretation of the planetary properties of the hot Jupiters. Therefore, for a consistent and accurate interpretation of the observed transit spectra, it is essential to include the diffused reflection and transmission due to scattering in the optical and near-infrared wavelength region and the thermal re-emission at the near and mid-infrared region of hot gas giant planets. Both need the solutions of the multi-scattering radiative transfer equations.

Summary

The novel aspects of this thesis are:

- Conducting transit photometric survey and follow-up observation and development of pipelines for reduction and analysis of the images (`pyapphot`) and modeling of the transit light curves.
- Implementation of denoising or noise modeling techniques for better precision in the planetary properties estimated from the transit photometry.
- Performing transit spectroscopy of certain host stars for the first time and estimation of SNR required.
- Development of a complete pipeline for basic modeling of the atmospheres of hot Jupiters that can be used for retrieval of planetary properties from the observational data such as transmission spectra, reflection spectra, emission spectra etc.
- Incorporation of physical processes like diffused reflection and emission due to the scattering of light in the planetary atmospheres and emission from the night side of the planets for a more accurate representation of the transmission spectra observed from the hot Jupiters.

Observation of the transit events of exoplanets and determination of planetary properties from those observed data are extremely challenging as transit

observations are extremely sensitive and photon-starving and are prone to pick up noise from different sources. The development of a pipeline for handling and processing of the bulk amount of observed data is necessary. We, for the first time, developed automatic tools for the reduction, processing and modeling of the data observed from the Indian telescopes. These tools exhibit smart features like auto-selection and auto-filtering of frames, auto-extraction of all the necessary data from the images and easy execution of differential aperture photometry. Again, the tool developed for the modeling of transit light curves is based on Bayesian inversion framework and is designed for maximum precision in the deduced parameters. For better precision in the deduced parameters, we have studied the different sources of noise and segregated and treated the different noises accordingly incorporating new denoising techniques. We perform preprocessing of light curves employing wavelet denoising method to reduce the small-scale temporally uncorrelated noises. On the other hand, we model the transit light curves along with Guassian process regression to model and filter out the temporally correlated noises. Using these pipelines we have first conducted some transit survey observations searching for planets around stars with no reported planet. We didn't get any trace of planetary transits due to the limited time of availability of the telescopes to us, however, we could assess the stability of the observations and observed light curves of the stars as we chose the stars with no reported variability and no binary component. We also observed some of the stars known to host planets outside the time of predicted transit events to characterize the baseline of the light curves. We followed up the transit events of some known hot Jupiters and published the results obtained from the follow-up of five such hot Jupiter, viz., WASP-33 b, WASP-50 b, WASP-12 b, HATS-18 b and HAT-P-36 b in the Astronomical Journal. This publication has been selected as the default reference for the default parameters of these five planets on the basis of precision by the public-accessible website, NASA Exoplanet Archive. We have also been following up more hot Jupiters. The results are being procured for another publication.

Also, our survey operation in the search for new exoplanets is being continued.

We have also performed high-resolution transit spectroscopy of a few planet-hosting stars out of which we have presented here the results for 2 stars, viz., KELT-4A and HD149026. To the best of our knowledge, no transit spectroscopic results have been reported for these host stars. Our results cannot infer anything about the atmospheres of the orbiting hot Jupiters but give us some idea about the signal requirements of these observations. Both the low-resolution and the high-resolution transit spectroscopic observations of the host stars are continued.

Another important aspect of the thesis is to develop a complete pipeline that performs all the calculations for accurate modeling of the physical and chemical processes in the atmospheres of the hot Jupiters that could explain the observed transmission, reflection and emission spectra. We have developed a single platform that calculates the atmospheric density, the absorption and scattering coefficients at different altitudes in the atmosphere. It also fully solves the 1-D radiative transfer equations to calculate the transmission, reflection and emission spectra.

One major contribution from us is the incorporation of the effects of diffused reflection and transmission due to scattering in the calculation of the transmission spectra. Moreover, we incorporated the effect of clouds or haze using the Mie theory of scattering. To include the effect of scattering we solved the complete 1-D radiative transfer equations instead of using the Beer-Bouguer-Lambert law. For a cloudless planetary atmosphere, Rayleigh scattering albedo alters the transmission depth up to about 0.6μm , but the change in the transmission depth due to forward scattering by cloud or haze is significant throughout the optical and near-infrared regions up to about 1.2μm . We matched our models with the observed transmission spectra of some hot Jupiters which are available in the archive. The results demonstrate that a correct and consistent procedure is to solve the multiple-scattering radiative transfer equations as the change in transmitted flux due to diffused stellar radiation is significant.

However, in the infrared wavelength region where the effect of scattering is negligible, the Beer–Bouguer–Lambert law can very well be employed to calculate the transmission depth. We have published these studies and the results in the Astrophysical Journal.

Another major contribution from us is the study of the effect of thermal emission from the night side of the hot Jupiters on the transmission spectra observed from these planets. We studied the significance of the change in transit depth due to emission for different night-side average temperature and surface gravity of the hot Jupiters, the spectral type of the host stars and the radius ratio of the planet-star pairs. To estimate the significance we compared the change with respect to the noise levels of the different IR instruments on board the upcoming James Webb Space Telescope. The comparison demonstrates that the effect of thermal re-emission from the night sides of hot Jupiters on the transit spectra can be significant at the infrared wavelength region if the equilibrium temperature of the planet is higher than about 1200K and if the planet is large enough in size such that the radius ratio is greater than 0.1. Hence, for a more accurate representation of the transit spectra, it is essential to incorporate the planetary emission as well as solve the multi-scattering radiative transfer equations. We have published the results of this study in the Astrophysical Journal.

The upcoming missions such as JWST, ARIEL, etc., once online, will provide us with a vast amount of precise spectroscopic and photometric data of the exoplanets. In this regard, our approach to more consistent and accurate modeling of the planetary atmospheres and the observable spectra will prove to be extremely useful. Our current focus is on the development of a full-scale retrieval analysis of the planetary properties from the observed transmission spectra of the hot Jupiters based on the forward atmospheric models explained above. Moreover, we are working on the technique of probing into the atmospheres of the hot Jupiters with polarization. Results from both the studies will be procured for separate publications.

Bibliography

Ackerman, A. S., & Marley, M. S. 2001, *Astrophys. J.*, 556, 872, doi: 10.1086/321540

Alonso, R., Brown, T. M., Torres, G., et al. 2004, *Astrophys. J. Lett.*, 613, L153, doi: 10.1086/425256

An, J. H., Evans, N. W., Kerins, E., et al. 2004, *Astrophys. J.*, 601, 845, doi: 10.1086/380820

Anche, R. M., Anupama, G. C., Reddy, K., et al. 2015, in Society of Photo-Optical Instrumentation Engineers (SPIE) Conference Series, Vol. 9654, International Conference on Optics and Photonics 2015, 965408

Arcangeli, J., Désert, J.-M., Parmentier, V., et al. 2019, *Astron. Astrophys.*, 625, A136, doi: 10.1051/0004-6361/201834891

Arribas, S., Gilliland, R. L., Sparks, W. B., et al. 2006, *Pub. Astron. Soc. Pac.*, 118, 21, doi: 10.1086/497674

Asplund, M., Grevesse, N., Sauval, A. J., & Scott, P. 2009, *Annurev.aa.* , 47, 481, doi: 10.1146/annurev.astro.46.060407.145222

Atwood, J., Skidmore, W., Anupama, G. C., et al. 2014, in Society of Photo-Optical Instrumentation Engineers (SPIE) Conference Series, Vol. 9150,

Modeling, Systems Engineering, and Project Management for Astronomy VI, 915013

Bakos, G. Á., Noyes, R. W., Kovács, G., et al. 2007, *Astrophys. J.*, 656, 552, doi: 10.1086/509874

Bakos, G. Á., Torres, G., Pál, A., et al. 2010, *Astrophys. J.*, 710, 1724, doi: 10.1088/0004-637X/710/2/1724

Bakos, G. Á., Hartman, J. D., Torres, G., et al. 2012, *Astron. J.*, 144, 19, doi: 10.1088/0004-6256/144/1/19

Ballester, G. E., Sing, D. K., & Herbert, F. 2007, *Nature*, 445, 511, doi: 10.1038/nature05525

Barclay, T., Endl, M., Huber, D., et al. 2015, *Astrophys. J.*, 800, 46, doi: 10.1088/0004-637X/800/1/46

Barge, P., Baglin, A., Auvergne, M., et al. 2008, *Astron. Astrophys.*, 482, L17, doi: 10.1051/0004-6361:200809353

Barman, T. 2007, *Astrophys. J. Lett.*, 661, L191, doi: 10.1086/518736

Barsanti, R. J., & Gilmore, J. 2011, in 2011 IEEE 43rd Southeastern Symposium on System Theory, 163–167

Barstow, J. K., Aigrain, S., Irwin, P. G. J., & Sing, D. K. 2017, *Astrophys. J.*, 834, 50, doi: 10.3847/1538-4357/834/1/50

Batalha, N. E., Mandell, A., Pontoppidan, K., et al. 2017, *Pub. Astron. Soc. Pac.*, 129, 064501, doi: 10.1088/1538-3873/aa65b0

Batalha, N. M., Borucki, W. J., Bryson, S. T., et al. 2011, *Astrophys. J.*, 729, 27, doi: 10.1088/0004-637X/729/1/27

Bean, J. L., Désert, J.-M., Kabath, P., et al. 2011, *Astrophys. J.*, 743, 92, doi: 10.1088/0004-637X/743/1/92

Beaulieu, J. P., Carey, S., Ribas, I., & Tinetti, G. 2008, *Astrophys. J.*, 677, 1343, doi: 10.1086/527045

Berta, Z. K., Charbonneau, D., Désert, J.-M., et al. 2012, *Astrophys. J.*, 747, 35, doi: 10.1088/0004-637X/747/1/35

Birkby, J. L., de Kok, R. J., Brogi, M., et al. 2013, *Mon. Not. Roy. Astron. Soc.*, 436, L35, doi: 10.1093/mnrasl/slt107

Bohren, C. F., & Huffman, D. R. 1983, Absorption and scattering of light by small particles

Brogi, M., de Kok, R. J., Albrecht, S., et al. 2016, *Astrophys. J.*, 817, 106, doi: 10.3847/0004-637X/817/2/106

Brown, T. M. 2001, *Astrophys. J.*, 553, 1006, doi: 10.1086/320950

Bundy, K. A., & Marcy, G. W. 2000, *Pub. Astron. Soc. Pac.*, 112, 1421, doi: 10.1086/317706

Burgasser, A. J., McElwain, M. W., Kirkpatrick, J. D., et al. 2004, *Astron. J.*, 127, 2856, doi: 10.1086/383549

Burrows, A., Budaj, J., & Hubeny, I. 2008, *Astrophys. J.*, 678, 1436, doi: 10.1086/533518

Burrows, A., Sudarsky, D., & Hubbard, W. B. 2003, *Astrophys. J.*, 594, 545, doi: 10.1086/376897

Burrows, A., Marley, M., Hubbard, W. B., et al. 1997, *Astrophys. J.*, 491, 856, doi: 10.1086/305002

Carter, A. L., Nikolov, N., Sing, D. K., et al. 2020, *Mon. Not. Roy. Astron. Soc.*, 494, 5449, doi: 10.1093/mnras/staa1078

Catling, D. C., & Kasting, J. F. 2017, Atmospheric Evolution on Inhabited and Lifeless Worlds

Chakrabarty, A., & Sengupta, S. 2019, *Astron. J.*, 158, 39, doi: 10.3847/1538-3881/ab24dd

—. 2020, *Astrophys. J.*, 898, 89, doi: 10.3847/1538-4357/ab9a33

Chamberlain, J. W., & Hunten, D. M. 1987, Theory of planetary atmospheres. An introduction to their physics andchemistry., Vol. 36

Chandrasekhar, S. 1960, Radiative transfer

Charbonneau, D., Brown, T. M., Latham, D. W., & Mayor, M. 2000, *Astrophys. J. Lett.*, 529, L45, doi: 10.1086/312457

Charbonneau, D., Brown, T. M., Noyes, R. W., & Gilliland, R. L. 2002, *Astrophys. J.*, 568, 377, doi: 10.1086/338770

Charbonneau, D., Berta, Z. K., Irwin, J., et al. 2009, *Nature*, 462, 891, doi: 10.1038/nature08679

Chen, G., Casasayas-Barris, N., Pallé, E., et al. 2020, *Astron. Astrophys.*, 635, A171, doi: 10.1051/0004-6361/201936986

Claret, A., & Bloemen, S. 2011, *Astron. Astrophys.*, 529, A75, doi: 10.1051/0004-6361/201116451

Collier Cameron, A., Bouchy, F., Hébrard, G., et al. 2007, *Mon. Not. Roy. Astron. Soc.*, 375, 951, doi: 10.1111/j.1365-2966.2006.11350.x

Collier Cameron, A., Guenther, E., Smalley, B., et al. 2010, *Mon. Not. Roy. Astron. Soc.*, 407, 507, doi: 10.1111/j.1365-2966.2010.16922.x

Collins, K. A., Kielkopf, J. F., & Stassun, K. G. 2017, *Astron. J.*, 153, 78, doi: 10.3847/1538-3881/153/2/78

Cooper, C. S., Sudarsky, D., Milsom, J. A., Lunine, J. I., & Burrows, A. 2003, *Astrophys. J.*, 586, 1320, doi: 10.1086/367763

Cowan, N. B., & Agol, E. 2011, *Astrophys. J.*, 729, 54, doi: 10.1088/0004-637X/729/1/54

Cubillos, P., Harrington, J., Loredo, T. J., et al. 2017, *Astron. J.*, 153, 3, doi: 10.3847/1538-3881/153/1/3

Cushing, M. C., Marley, M. S., Saumon, D., et al. 2008, *Astrophys. J.*, 678, 1372, doi: 10.1086/526489

Dai, X., & Guerras, E. 2018, *Astrophys. J. Lett.*, 853, L27, doi: 10.3847/2041-8213/aaa5fb

de Kok, R. J., Brogi, M., Snellen, I. A. G., et al. 2013, *Astron. Astrophys.*, 554, A82, doi: 10.1051/0004-6361/201321381

de Kok, R. J., & Stam, D. M. 2012, *Icarus*, 221, 517, doi: 10.1016/j.icarus.2012.08.020

del Ser, D., Fors, O., & Núñez, J. 2018, *Astron. Astrophys.*, 619, A86, doi: 10.1051/0004-6361/201730671

Deming, D., Wilkins, A., McCullough, P., et al. 2013, *Astrophys. J.*, 774, 95, doi: 10.1088/0004-637X/774/2/95

Demory, B.-O., Gillon, M., de Wit, J., et al. 2016, *Nature*, 532, 207, doi: 10.1038/nature17169

Evans, T. M., Sing, D. K., Goyal, J. M., et al. 2018, *Astron. J.*, 156, 283, doi: 10.3847/1538-3881/aaebff

Filippazzo, J. C., Rice, E. L., Faherty, J., et al. 2015, *Astrophys. J.*, 810, 158, doi: 10.1088/0004-637X/810/2/158

Fortney, J. J. 2018, arXiv e-prints, arXiv:1804.08149. https://arxiv.org/abs/1804.08149

Fortney, J. J., Marley, M. S., Lodders, K., Saumon, D., & Freedman, R. 2005, *Astrophys. J. Lett.*, 627, L69, doi: 10.1086/431952

Fortney, J. J., Marley, M. S., Saumon, D., & Lodders, K. 2008, *Astrophys. J.*, 683, 1104, doi: 10.1086/589942

Fortney, J. J., Mordasini, C., Nettelmann, N., et al. 2013, *Astrophys. J.*, 775, 80, doi: 10.1088/0004-637X/775/1/80

Fortney, J. J., Shabram, M., Showman, A. P., et al. 2010, *Astrophys. J.*, 709, 1396, doi: 10.1088/0004-637X/709/2/1396

Fowler, B. W. 1983, Journal of the Optical Society of America (1917-1983), 73, 19

Frazin, R. 2019, in American Astronomical Society Meeting Abstracts, Vol. 233, American Astronomical Society Meeting Abstracts #233, 467.07

Freedman, R. S., Lustig-Yaeger, J., Fortney, J. J., et al. 2014, *Astrophys. J.S*, 214, 25, doi: 10.1088/0067-0049/214/2/25

Freedman, R. S., Marley, M. S., & Lodders, K. 2008, *Astrophys. J.S*, 174, 504, doi: 10.1086/521793

Gaudi, B. S., Stassun, K. G., Collins, K. A., et al. 2017, *Nature*, 546, 514, doi: 10.1038/nature22392

Gibson, N. P., Aigrain, S., Pont, F., et al. 2012, *Mon. Not. Roy. Astron. Soc.*, 422, 753, doi: 10.1111/j.1365-2966.2012.20655.x

Gillon, M., Doyle, A. P., Lendl, M., et al. 2011, *Astron. Astrophys.*, 533, A88, doi: 10.1051/0004-6361/201117198

Gillon, M., Jehin, E., Lederer, S. M., et al. 2016, *Nature*, 533, 221, doi: 10.1038/nature17448

Gillon, M., Triaud, A. H. M. J., Demory, B.-O., et al. 2017, *Nature*, 542, 456, doi: 10.1038/nature21360

Goody, R., West, R., Chen, L., & Crisp, D. 1989, *J QUANT SPECTROSC RA*, 42, 539, doi: 10.1016/0022-4073(89)90044-7

Gordon, I. E., Rothman, L. S., Hill, C., et al. 2017, *J QUANT SPECTROSC RA*, 203, 3, doi: 10.1016/j.jqsrt.2017.06.038

Goyal, J. M., Wakeford, H. R., Mayne, N. J., et al. 2019, *Mon. Not. Roy. Astron. Soc.*, 482, 4503, doi: 10.1093/mnras/sty3001

Goyal, J. M., Mayne, N., Sing, D. K., et al. 2018, *Mon. Not. Roy. Astron. Soc.*, 474, 5158, doi: 10.1093/mnras/stx3015

Grenier, S., Baylac, M.-O., Rolland, L., et al. 1999, *Astron. Astrophys. Suppl.*, 137, 451, doi: 10.1051/aas:1999489

Griffith, C. A., Yelle, R. V., & Marley, M. S. 1998, Science, 282, 2063, doi: 10.1126/science.282.5396.2063

Grillmair, C. J., Charbonneau, D., Burrows, A., et al. 2007, *Astrophys. J. Lett.*, 658, L115, doi: 10.1086/513741

Guillot, T. 2010, *Astron. Astrophys.*, 520, A27, doi: 10.1051/0004-6361/200913396

Hansen, B. M. S. 2008, *Astrophys. J.S*, 179, 484, doi: 10.1086/591964

Hansen, J. E., & Travis, L. D. 1974, *Space Sci. Rev.*, 16, 527, doi: 10.1007/BF00168069

Heng, K., & Kitzmann, D. 2017, *Astrophys. J.S*, 232, 20, doi: 10.3847/1538-4365/aa8907

Heng, K., Malik, M., & Kitzmann, D. 2018, *Astrophys. J.S*, 237, 29, doi: 10.3847/1538-4365/aad199

Henry, G. W., Marcy, G. W., Butler, R. P., & Vogt, S. S. 2000, *Astrophys. J. Lett.*, 529, L41, doi: 10.1086/312458

Herrero, E., Morales, J. C., Ribas, I., & Naves, R. 2011, *Astron. Astrophys.*, 526, L10, doi: 10.1051/0004-6361/201015875

Hoeijmakers, H. J., Ehrenreich, D., Heng, K., et al. 2018, *Nature*, 560, 453, doi: 10.1038/s41586-018-0401-y

Huitson, C. M., Désert, J. M., Bean, J. L., et al. 2017, *Astron. J.*, 154, 95, doi: 10.3847/1538-3881/aa7f72

Johnson, M. C., Cochran, W. D., Collier Cameron, A., & Bayliss, D. 2015, *Astrophys. J. Lett.*, 810, L23, doi: 10.1088/2041-8205/810/2/L23

Kataria, T., Showman, A. P., Fortney, J. J., et al. 2015, *Astrophys. J.*, 801, 86, doi: 10.1088/0004-637X/801/2/86

Kataria, T., Sing, D. K., Lewis, N. K., et al. 2016, *Astrophys. J.*, 821, 9, doi: 10.3847/0004-637X/821/1/9

Keating, D., & Cowan, N. B. 2017, *Astrophys. J. Lett.*, 849, L5, doi: 10.3847/2041-8213/aa8b6b

Keles, E., Mallonn, M., von Essen, C., et al. 2019, *Mon. Not. Roy. Astron. Soc.*, 489, L37, doi: 10.1093/mnrasl/slz123

Keller, C. U., Schmid, H. M., Venema, L. B., et al. 2010, in Ground-based and Airborne Instrumentation for Astronomy III, ed. I. S. McLean, S. K. Ramsay, & H. Takami, Vol. 7735, International Society for Optics and Photonics (SPIE), 2342 – 2354. https://doi.org/10.1117/12.857626

Kempton, E. M. R., Lupu, R., Owusu-Asare, A., Slough, P., & Cale, B. 2017, *Pub. Astron. Soc. Pac.*, 129, 044402, doi: 10.1088/1538-3873/aa61ef

Knutson, H. A., Charbonneau, D., Allen, L. E., et al. 2007, *Nature*, 447, 183, doi: 10.1038/nature05782

Konacki, M., Torres, G., Jha, S., & Sasselov, D. D. 2003, *Nature*, 421, 507, doi: 10.1038/nature01379

Kovács, G., Zucker, S., & Mazeh, T. 2002, *Astron. Astrophys.*, 391, 369, doi: 10.1051/0004-6361:20020802

Lagha, M., Tikhemirine, M., Bergheul, S., Rezoug, T., & Bettayeb, M. 2013, Digital Signal Processing, 23, 322, doi: 10.1016/j.dsp.2012.08.001

Lee, G. R., Gommers, R., Wohlfahrt, K., et al. 2018, PyWavelets/pywt: PyWavelets v1.0.0, doi: 10.5281/zenodo.1407172. https://doi.org/10.5281/zenodo.1407172

Lehmann, H., Guenther, E., Sebastian, D., et al. 2015, *Astron. Astrophys.*, 578, L4, doi: 10.1051/0004-6361/201526176

Liebert, J., Williams, K. A., Holberg, J. B., & Sing, D. K. 2006, *Pub. Astron. Soc. Pac.*, 118, 1528, doi: 10.1086/509664

Lodders, K. 2003, *Astrophys. J.*, 591, 1220, doi: 10.1086/375492

Lodders, K., & Fegley, B. 2002, *Icarus*, 155, 393, doi: 10.1006/icar.2001.6740

Lomb, N. R. 1976, *Astrophys. Space Sci.*, 39, 447, doi: 10.1007/BF00648343

Lupu, R. E., Zahnle, K., Marley, M. S., et al. 2014, *Astrophys. J.*, 784, 27, doi: 10.1088/0004-637X/784/1/27

Maciejewski, G., Dimitrov, D., Fernández, M., et al. 2016, *Astron. Astrophys.*, 588, L6, doi: 10.1051/0004-6361/201628312

Maciejewski, G., Fernández, M., Aceituno, F., et al. 2018, *ACTA ASTRONOM*, 68, 371, doi: 10.32023/0001-5237/68.4.4

Madhusudhan, N., Mousis, O., Johnson, T. V., & Lunine, J. I. 2011a, *Astrophys. J.*, 743, 191, doi: 10.1088/0004-637X/743/2/191

Madhusudhan, N., & Seager, S. 2009, *Astrophys. J.*, 707, 24, doi: 10.1088/0004-637X/707/1/24

—. 2011, *Astrophys. J.*, 729, 41, doi: 10.1088/0004-637X/729/1/41

Madhusudhan, N., Harrington, J., Stevenson, K. B., et al. 2011b, *Nature*, 469, 64, doi: 10.1038/nature09602

Mallat, S. G. 1989, IEEE Transactions on Pattern Analysis and Machine Intelligence, 11, 674

Mancini, L., Esposito, M., Covino, E., et al. 2015, *Astron. Astrophys.*, 579, A136, doi: 10.1051/0004-6361/201526030

Mandel, K., & Agol, E. 2002, *Astrophys. J. Lett.*, 580, L171, doi: 10.1086/345520

Marley, M. S., Gelino, C., Stephens, D., Lunine, J. I., & Freedman, R. 1999, *Astrophys. J.*, 513, 879, doi: 10.1086/306881

Marley, M. S., & McKay, C. P. 1999, *Icarus*, 138, 268, doi: 10.1006/icar.1998.6071

Marley, M. S., Saumon, D., Guillot, T., et al. 1996, Science, 272, 1919, doi: 10.1126/science.272.5270.1919

Marley, M. S., & Sengupta, S. 2011, *Mon. Not. Roy. Astron. Soc.*, 417, 2874, doi: 10.1111/j.1365-2966.2011.19448.x

Martins, J. H. C., Figueira, P., Santos, N. C., et al. 2018, *Mon. Not. Roy. Astron. Soc.*, 478, 5240, doi: 10.1093/mnras/sty1355

Mayor, M., & Queloz, D. 1995, *Nature*, 378, 355, doi: 10.1038/378355a0

McKay, C. P., Pollack, J. B., & Courtin, R. 1989, *Icarus*, 80, 23, doi: 10.1016/0019-1035(89)90160-7

Mollière, P., van Boekel, R., Dullemond, C., Henning, T., & Mordasini, C. 2015, *Astrophys. J.*, 813, 47, doi: 10.1088/0004-637X/813/1/47

Morley, C. V., Fortney, J. J., Marley, M. S., et al. 2012, *Astrophys. J.*, 756, 172, doi: 10.1088/0004-637X/756/2/172

—. 2015, *Astrophys. J.*, 815, 110, doi: 10.1088/0004-637X/815/2/110

Moutou, C., Coustenis, A., Schneider, J., et al. 2001, *Astron. Astrophys.*, 371, 260, doi: 10.1051/0004-6361:20010406

Narita, N., Suto, Y., Winn, J. N., et al. 2005, *Pub. Astron. Soc. Japan*, 57, 705, doi: 10.1093/pasj/57.4.705

Nikolov, N., Sing, D. K., Gibson, N. P., et al. 2016, *Astrophys. J.*, 832, 191, doi: 10.3847/0004-637X/832/2/191

Nugroho, S. K., Kawahara, H., Masuda, K., et al. 2017, *Astron. J.*, 154, 221, doi: 10.3847/1538-3881/aa9433

Pallé, E., Chen, G., Alonso, R., et al. 2016, *Astron. Astrophys.*, 589, A62, doi: 10.1051/0004-6361/201527881

Parmentier, V., & Crossfield, I. J. M. 2018, Exoplanet Phase Curves: Observations and Theory, 116

Parmentier, V., & Guillot, T. 2014, *Astron. Astrophys.*, 562, A133, doi: 10.1051/0004-6361/201322342

Parmentier, V., Guillot, T., Fortney, J. J., & Marley, M. S. 2015, *Astron. Astrophys.*, 574, A35, doi: 10.1051/0004-6361/201323127

Patra, K. C., Winn, J. N., Holman, M. J., et al. 2017, *Astron. J.*, 154, 4, doi: 10.3847/1538-3881/aa6d75

Penev, K., Hartman, J. D., Bakos, G. Á., et al. 2016, *Astron. J.*, 152, 127, doi: 10.3847/0004-6256/152/5/127

Peraiah, A., & Grant, I. P. 1973, J. Int. Math. Appl, 12, 75

Pierrehumbert, R. T. 2010, Principles of Planetary Climate

Poddaný, S., Brát, L., & Pejcha, O. 2010, New Astronomy, 15, 297 , doi: https://doi.org/10.1016/j.newast.2009.09.001

Pont, F., Gilliland, R. L., Knutson, H., Holman, M., & Charbonneau, D. 2009, *Mon. Not. Roy. Astron. Soc.*, 393, L6, doi: 10.1111/j.1745-3933.2008.00582.x

Queloz, D., Bouchy, F., Moutou, C., et al. 2009, *Astron. Astrophys.*, 506, 303, doi: 10.1051/0004-6361/200913096

Rasmussen, C. E., & Williams, C. K. I. 2006, Gaussian Processes for Machine Learning

Redfield, S., Endl, M., Cochran, W. D., & Koesterke, L. 2008, *Astrophys. J. Lett.*, 673, L87, doi: 10.1086/527475

Robinson, T. D., & Catling, D. C. 2012, *Astrophys. J.*, 757, 104, doi: 10.1088/0004-637X/757/1/104

Rosenblatt, F. 1971, *Icarus*, 14, 71, doi: 10.1016/0019-1035(71)90103-5

Sánchez-López, A., Alonso-Floriano, F. J., López-Puertas, M., et al. 2019, *Astron. Astrophys.*, 630, A53, doi: 10.1051/0004-6361/201936084

Saumon, D., Geballe, T. R., Leggett, S. K., et al. 2000, *Astrophys. J.*, 541, 374, doi: 10.1086/309410

Saumon, D., & Marley, M. S. 2008, *Astrophys. J.*, 689, 1327, doi: 10.1086/592734

Scargle, J. D. 1982, *Astrophys. J.*, 263, 835, doi: 10.1086/160554

Seager, S. 2010, Exoplanet Atmospheres: Physical Processes

Seager, S., & Sasselov, D. D. 2000, *Astrophys. J.*, 537, 916, doi: 10.1086/309088

Sengupta, S. 2008, *Astrophys. J. Lett.*, 683, L195, doi: 10.1086/591733

—. 2013, Journal of Astrophysics and Astronomy, 34, 151, doi: 10.1007/s12036-013-9170-z

—. 2018, *Astrophys. J.*, 861, 41, doi: 10.3847/1538-4357/aac6da

Sengupta, S., Chakrabarty, A., & Tinetti, G. 2020, *Astrophys. J.*, 889, 181, doi: 10.3847/1538-4357/ab6592

Sengupta, S., & Marley, M. S. 2009, *Astrophys. J.*, 707, 716, doi: 10.1088/0004-637X/707/1/716

—. 2010, *Astrophys. J. Lett.*, 722, L142, doi: 10.1088/2041-8205/722/2/L142

—. 2016, *Astrophys. J.*, 824, 76, doi: 10.3847/0004-637X/824/2/76

Sing, D. K., Fortney, J. J., Nikolov, N., et al. 2016, *Nature*, 529, 59, doi: 10.1038/nature16068

Skemer, A. 2019, in AAS/Division for Extreme Solar Systems Abstracts, Vol. 51, AAS/Division for Extreme Solar Systems Abstracts, 503.02

Snellen, I. A. G., Albrecht, S., de Mooij, E. J. W., & Le Poole, R. S. 2008, *Astron. Astrophys.*, 487, 357, doi: 10.1051/0004-6361:200809762

Snellen, I. A. G., de Kok, R. J., de Mooij, E. J. W., & Albrecht, S. 2010, *Nature*, 465, 1049, doi: 10.1038/nature09111

Southworth, J., Wheatley, P. J., & Sams, G. 2007, *Mon. Not. Roy. Astron. Soc.*, 379, L11, doi: 10.1111/j.1745-3933.2007.00324.x

Stam, D. M., de Rooij, W. A., Cornet, G., & Hovenier, J. W. 2006, *Astron. Astrophys.*, 452, 669, doi: 10.1051/0004-6361:20054364

Stephens, D. C., Leggett, S. K., Cushing, M. C., et al. 2009, *Astrophys. J.*, 702, 154, doi: 10.1088/0004-637X/702/1/154

Stevenson, K. B., Bean, J. L., Seifahrt, A., et al. 2014, *Astron. J.*, 147, 161, doi: 10.1088/0004-6256/147/6/161

—. 2016, *Astrophys. J.*, 817, 141, doi: 10.3847/0004-637X/817/2/141

Sudarsky, D., Burrows, A., & Hubeny, I. 2003, *Astrophys. J.*, 588, 1121, doi: 10.1086/374331

Tanner, A., & Crossfield, I. 2014, in Thirty Meter Telescope Science Forum, 50

Tennyson, J., & Yurchenko, S. N. 2012, *Mon. Not. Roy. Astron. Soc.*, 425, 21, doi: 10.1111/j.1365-2966.2012.21440.x

Tennyson, J., Yurchenko, S. N., Al-Refaie, A. F., et al. 2016, Journal of Molecular Spectroscopy, 327, 73, doi: 10.1016/j.jms.2016.05.002

Tinetti, G., Encrenaz, T., & Coustenis, A. 2013, *Astron. Astrophys. Rev.*, 21, 63, doi: 10.1007/s00159-013-0063-6

Tinetti, G., Liang, M.-C., Vidal-Madjar, A., et al. 2007a, *Astrophys. J. Lett.*, 654, L99, doi: 10.1086/510716

Tinetti, G., Vidal-Madjar, A., Liang, M.-C., et al. 2007b, *Nature*, 448, 169, doi: 10.1038/nature06002

Toon, O. B., McKay, C. P., Ackerman, T. P., & Santhanam, K. 1989, *J. Geophys. Res.*, 94, 16287, doi: 10.1029/JD094iD13p16287

Tsiaras, A., Waldmann, I. P., Zingales, T., et al. 2018, *Astron. J.*, 155, 156, doi: 10.3847/1538-3881/aaaf75

Turner, J. D., Pearson, K. A., Biddle, L. I., et al. 2016, *Mon. Not. Roy. Astron. Soc.*, 459, 789, doi: 10.1093/mnras/stw574

Turner, J. D., de Mooij, E. J. W., Jayawardhana, R., et al. 2020, *Astrophys. J. Lett.*, 888, L13, doi: 10.3847/2041-8213/ab60a9

Valencia, D., Guillot, T., Parmentier, V., & Freedman, R. S. 2013, *Astrophys. J.*, 775, 10, doi: 10.1088/0004-637X/775/1/10

van de Hulst, H. C. 1957, Light Scattering by Small Particles

Vidal-Madjar, A., Lecavelier des Etangs, A., Désert, J. M., et al. 2003, *Nature*, 422, 143, doi: 10.1038/nature01448

Vidal-Madjar, A., Désert, J. M., Lecavelier des Etangs, A., et al. 2004, *Astrophys. J. Lett.*, 604, L69, doi: 10.1086/383347

von Essen, C., Czesla, S., Wolter, U., et al. 2014, *Astron. Astrophys.*, 561, A48, doi: 10.1051/0004-6361/201322453

Waldmann, I. P. 2014, *Astrophys. J.*, 780, 23, doi: 10.1088/0004-637X/780/1/23

Waldmann, I. P., Rocchetto, M., Tinetti, G., et al. 2015a, *Astrophys. J.*, 813, 13, doi: 10.1088/0004-637X/813/1/13

Waldmann, I. P., Tinetti, G., Rocchetto, M., et al. 2015b, *Astrophys. J.*, 802, 107, doi: 10.1088/0004-637X/802/2/107

Wilson, D. M., Enoch, B., Christian, D. J., et al. 2006, *Pub. Astron. Soc. Pac.*, 118, 1245, doi: 10.1086/507957

Wolszczan, A., & Frail, D. A. 1992, *Nature*, 355, 145, doi: 10.1038/355145a0

Wood, P. L., Maxted, P. F. L., Smalley, B., & Iro, N. 2011, *Mon. Not. Roy. Astron. Soc.*, 412, 2376, doi: 10.1111/j.1365-2966.2010.18061.x

Yip, K. H., Nikolaou, N., Coronica, P., et al. 2019, in AAS/Division for Extreme Solar Systems Abstracts, Vol. 51, AAS/Division for Extreme Solar Systems Abstracts, 305.04